RICE UNIVERSITY

Quantum criticality of strongly correlated systems

By

Chia-Chuan Liu

A THESIS SUBMITTED
IN PARTIAL FULFILLMENT OF THE
REQUIREMENTS FOR THE DEGREE

Doctor of Philosophy

APPROVED, THESIS COMMITTEE

Qimiao Si
Qimiao Si (Apr 21, 2020)

Qimiao Si

Harry C. and Olga K. Weiss Professor of Physics and Astronomy

Matthew S. Foster
Matthew S. Foster (Apr 21, 2020)

Matthew Foster

Associate Professor of Physics and Astronomy

Junichiro Kono
Junichiro Kono (Apr 21, 2020)

Junichiro Kono

Professor of Electrical and Computer Engineering, Professor of Materials Science and Nanoengineering, Professor of Physics and Astron

HOUSTON, TEXAS

April 2020

RICE UNIVERSITY

Quantum criticality of strongly correlated systems

by

Chia-Chuan Liu

A Thesis Submitted
in Partial Fulfillment of the
Requirements for the Degree

Doctor of Philosophy

Approved, Thesis Committee:

Qimiao Si, Chair
Harry C. and Olga K. Weiss Professor of
Physics and Astronomy

Matthew Foster
Associate Professor of Physics and
Astronomy

Junichiro Kono
Professor of Electrical and Computer
Engineering
Professor of Materials Science and
Nanoengineering
Professor of Physics and Astronomy

Houston, Texas

April, 2020

ABSTRACT

Quantum criticality of strongly correlated systems

by

Chia-Chuan Liu

Quantum criticality has been an active research topic in condensed matter physics, with major efforts being devoted to the heavy fermion material in which local moments are coupled with itinerant electrons through an antiferromagnetic Kondo coupling. The competition between the Kondo coupling and antiferromagnetic Ruderman–Kittel–Kasuya–Yosida(RKKY) interaction between local moments leads to a rich global phase diagram for these systems. It is a fundamentally important but challenging problem to develop a unified theoretical approach to understand this global phase diagram.

We approach this issue from the magnetically ordered side by using a quantum non-linear sigma model (QNLσM) to represent the local moments. We firstly study the consequence of skyrmion defects of antiferromagnetism on a honeycomb lattice. We solve the low energy effective Dirac Hamiltonian in the skyrmion background, and then identify the singlet orders through an enhanced correlations in the corresponding channels. In addition, we perform a renormalization group (RG) analysis of the QNLσM with a Kondo coupling by treating both bosonic and fermionic degrees of freedom on an equal footing. These results shed new insight into the global phase diagram of the heavy fermion systems.

Recent evidence of two consecutive Kondo destruction quantum critical points(QCPs)

in $Ce_3Pd_{20}Si_6$ also provides an interesting extension of the global phase diagram. Motivated by this development, we study a spin-orbital coupled Bose-Fermi Kondo model. By performing a Coulomb-gas based RG calculation of this model with Ising anisotropy, we show that a generic trajectory in the parameter space contains two QCPs associated with the destruction of the orbital and spin Kondo effects, respectively.

Not only the heavy fermion systems, iron pnictides also provide a platform to study quantum criticality. The new ingredient here is that the quantum critical singularities in the nematic and magnetic channels are concurrent, and their relationship has yet to be clarified. Here we study this problem within an effective Ginzburg-Landau theory for both channels in the presence of a small external uniaxial potential that breaks the lattice C_4 symmetry. We establish an identity that connects the spin excitation anisotropy, which is the difference of the dynamical spin susceptibilities at two ordering wave vectors $\vec{Q}_1 = (\pi, 0)$ and $\vec{Q}_2 = (0, \pi)$, with the dynamical magnetic susceptibility and static nematic susceptibility. Using this identity, we introduce a scaling procedure to determine the dynamical nematic susceptibility in the quantum critical regime, and illustrate the procedure in the case of the optimally Ni-doped $BaFe_2As_2$.

Preface

This thesis is based on the research conducted in Prof. Qimiao Si's group. Part of the work had been performed in collaboration with Prof. Pallab Goswami of Northwestern University and Prof. Elihu Abrahams who was at University of California, Los Angeles. The main results of this thesis can be found in the following publications:

- C.-C. Liu, P. Goswami, and Q. Si, "Skyrmion defects and competing singlet orders in a half-filled antiferromagnetic Kondo-Heisenberg model on the honeycomb lattice ", Phys. Rev. B 96, 125101 , (2017)

- C.-C. Liu, and Q. Si, "Quantum criticality of a quantum nonlinear sigma model with Kondo coupling: A renormalization group study", in preparation.

- V. Martelli, A. Cai, E. M. Nica, M. Taupin, A. Prokofiev, C. -C. Liu, H. -H. Lai, R. Yu, K. Ingersent, R. Küchler, A. M. Strydom, D. Geiger, J. Haenel, J. Larrea, Q. Si, S. Paschen, "Sequential localization of a complex electron fluid", PNAS 116 (36), 17701-17706 (2019)

- C.-C. Liu, and Q. Si, "Sequential quantum phase transitions of a spin-orbital-coupled Bose-Fermi Kondo model", in preparation.

- C.-C. Liu, E. Abrahams and Q. Si, "Quantum critical nematic fluctuations and spin excitation anisotropy in iron pnictides", arXiv:1910.14597

Acknowledgments

First of all, I would like to express my gratitude to my advisor Qimiao Si, for all of his support and guidance during my PhD research. Qimiao is not only a great physicist with outstanding insight in science, but also a good mentor. He always knows how to come up with projects that match the student's potential best. It is truly a pleasure to wok with him.

I would also like to thank Matthew Foster and Junichiro Kono for serving on my thesis committee. I benefited a lot from Matt's courses. I also appreciate him for his help on my job-finding. I thank Kaden Hazzard for being on my advisory committee and his generosity. He is always willing to provide me with help and sincere suggestions.

I would like to thank all my collaborators, Pallab Goswami and late Elihu Abrahams for all of the inspiring discussions and interactions on the relevant projects. Without their help, these works can not be done. Especially, I appreciate Pallab's help and suggestions on my job-finding. Even though I had no chance to meet Elihu in person, it is still a great honor for me to collaborate with a great physicist like him.

I would like to thank all the people I have interacted with in the condensed matter physics group: Ang Cai, Lei Chen, Yang-Zhi Chou, Wenxin Ding, Sara Grefe, Haoyu Hu, Wenjun Hu, Hsin-Hua Lai, Emilian Nica, Weiyi Wang, Zhentao Wang, Hongyi Xie, Li Yang. I am especially grateful to Ang for his guidance on using the high-performance cluster computing.

I would like to thank all the Rice Physics Department staff for their assistance. Their passion and smile always make me feel warm and comfortable, and make the department as a pleasant place for work and study.

Last but not the least, I would like to thank my family for their dedication to my education and their endless love and support.

Contents

Tables

Illustrations

Chapter 1

Overview

Critical phenomenon occurs when a physical system undergoes a continuous phase transition. Such phenomenon is ubiquitous in natural world, which is one of the reasons why the physics of critical phenomena is an important area at the crossroads of many different fields. The quest to understand it in a general and organized way has motived physicists to develop lots of universal concepts and techniques[15].

There are many reasons that make the physics of critical phenomena as an important and interesting subject. One of them is its elegance. At a critical point, the correlation length is divergent; there is then no characteristic length scale. Therefore, the system is scale invariant, and in turn physical quantities exhibit power law behavior. Moreover, the critical exponents of these power law functions near a critical point depend only on overall properties, such as the dimensionality and the symmetry, but not the microscopic details of the system, which means that many systems that look very different in detail actually share the same critical exponents. Such concept is called the universality[16, 17].

Another reason for the importance of the critical phenomena as a subject is that it is relevant to the understanding of other kinds of physical phenomena. Near a critical point, the system undergoes severe fluctuation. These critical fluctuations can interplay with other ingredients of the system, and cause some dramatic consequences in the end.

Depending on the nature of the fluctuations that drive the phase transition, one

can classify the critical phenomena into two classes: the classical and quantum criticality, driven by thermal and quantum fluctuations, respectively. Quantum phase transition arises between two different quantum phases at zero temperature[18, 19]. As we will see in chapter 2, near a quantum critical point(QCP), there is a region with non-zero temperature where both the quantum and thermal fluctuations are important. Within this region, the conventional quasiparticle description of low energy excitations of system fails, while many physical properties still exhibit some kinds of universal behavior that are hard to be explained within the conventional quasiparticle picture[20].

In recent years, quantum criticality in strongly correlated system has become an active research topic[21, 22, 23]. In such systems, the electron-electron interactions are large compared to the width of the relevant electronic band(s), the interaction could change the ground state, as well as the nature of the low-energy excitations. Finding unifying principles for how the electrons are organized in these systems, is a challenging but promising research topic. Empirically, quantum criticality appears to be important to many of such strongly correlated systems. Theoretically, there are a variety of correlated electron and quantum spin models in which quantum criticality can be examined. Therefore, studying quantum criticality in strongly correlated systems promises to lead us to some central unifying or guiding principles of strongly correlated systems and beyond.

The first successful unifying paradigm of interacting fermions is Landau Fermi liquid theory[24], where the interaction is regarded as "weak", in the sense that there is a one-to-one correspondence between the elementary excitations of the interacting system and a non-interacting one. The momentum distribution $n_{k\sigma}$ at low temperature still shows a sudden jump at the Fermi momentum k_F, and the spectral function still

retains a sharp peak. All of these suggest that the concepts of Fermi surface and the quasiparticle are still well-defined. What interaction does is only renormalizing the parameters that characterrize the quasiparticles, such as the effective mass. Following the Fermi liquid theory, one can easily derive the leading temperature dependences of the electrical resistivity $\rho \sim T^2$ and specific heat $C \sim T$.

However, as the interaction grows stronger, at some point the ground state would suddenly change to a completely different one. In other words, a the quantum phase transition happens, and thus the one-to-one correspondence between the spectrum of interacting and non-interacting system could fail. One famous example is the Mott transition[25], where the strong on-site Colomb repulsion can change the system from a metal into a insulator. Other examples are unconventional superconductors, where the term "unconventional" means that their superconductivity can not be explained by the conventional BCS theory.

In cuprate materials, the parent state is an antiferromagnetic Mott insulator. Upon doping with hole or electron, the antiferromagnetism is suppressed, while the superconductivity with high critical temperature emerges. Besides antiferromagnetism, other exotic phase, such as a pseudogap phase where the Fermi surface possesses a partial energy gap, also arises in the phase diagram of the cuprates. Since the quantum critical points of antiferromagnetic and pseudogap phases seem to lie close to or within the superconducting dome[26], it is reasonable to ask if the quantum critical fluctuations associated with these QCPs help develop the unconventional superconductivity. Moreover, above the optimal doping in the phase diagram there is a quantum critical region, in which the resistivity exhibits non-Fermi liquid(NFL) but universal temperature dependence $\rho = \rho_0 + AT$[27]. Remarkably, other kinds of unconventional superconductors, like heavy fermions[28] or iron-based materials[29],

also possess pretty similar overall phase diagrams. The schematic phase diagram of various strongly correlated systems are summarized in Fig. 1.1. These features suggest that quantum criticality is a candidate unifying concept in the understanding of the strongly correlated systems. This thesis is dedicated to deepening our understanding of this topic. In chapter 2, we will introduce the basic preliminary knowledge for the research presented in this thesis.

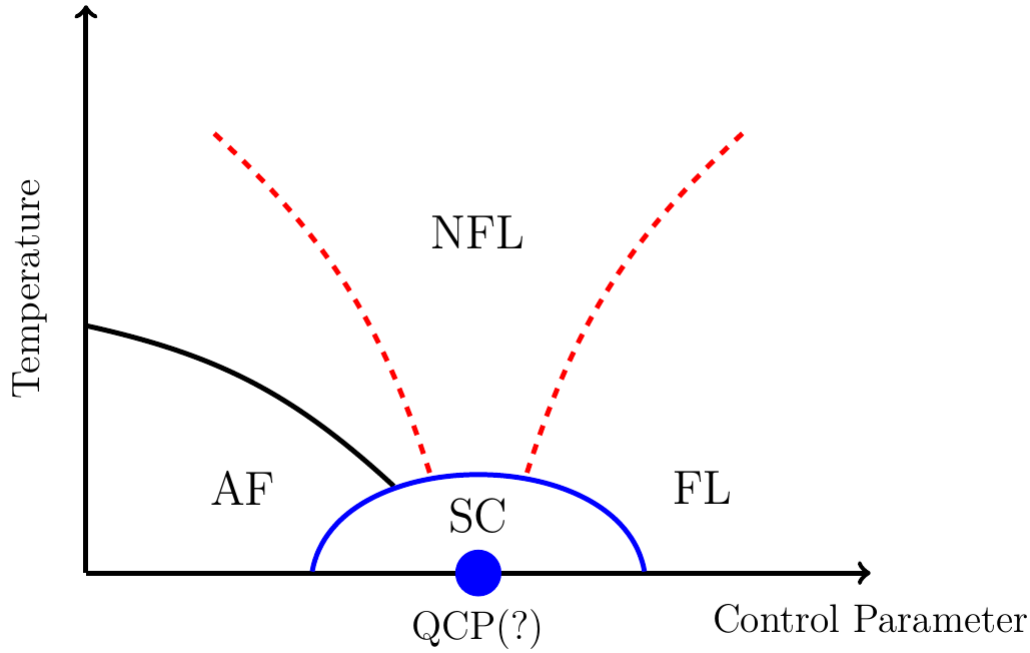

Figure 1.1 : Schematic phase diagram of various strongly correlated systems. Black and blue solid lines denote the antiferromagnetic(AF) and superconducting(SC) transitions, respectively. The blue dot is the presumable quantum critical point inside the SC dome, and above it there is a quantum critical regime in which the resistivity exhibits universal non-Fermi liquid(NFL) behavior.

Due to their high-tunability, heavy fermion compounds have been prototypical systems to study the quantum criticality. In these systems, the local moments are coupled with itinerant electrons through a Kondo coupling, which competes with

an antiferromagnetic Ruderman–Kittel–Kasuya–Yosida (RKKY) interaction between the local moments. When Kondo coupling is small, the local moments are decoupled from conduction electrons, and the RKKY interaction drives the system into antiferromagnetism. On the other hand, in the strong Kondo coupling regime, the ground state is a paramagnetic Kondo-screened phase where the Kondo singlets between the conduction electrons and f-electrons of local moments are formed, and the Fermi surface is enlarged due to the contribution from the f-electrons. In addition, strong frustration in the interactions between the local moments can also lead to another kind of paramagnetic state where the Kondo entanglement is absent and the Fermi surface remains small[1, 2, 30]. The competition between antiferromagnetism and a variety of proximate paramagnetic spin-singlet states is a common feature for many heavy fermion compounds, and has been discussed in the proposed global phase diagram as shown in Fig. 1.2.

From a theoretical perspective, the intricate interplay between different kinds of degrees of freedom makes it challenging to develop a unified framework for the quantum criticality of heavy fermion systems, even though it is fundamentally important. Most of previous studies only focused on single phase transition path by taking some specific theoretical approaches. In chapter 3, we approach this problem from the magnetically ordered side by using a quantum non-linear sigma model(QNLσM) to represent the local moments. We consider the consequence of skyrmion defects of antiferromagnetism. These topological defects are known to induce singlet orders based on a perturbative gradient expansion[31, 32]. By starting from antiferromagnetic Kondo honeycomb lattice model, we are able to solve the low energy effective Dirac Hamiltonian in the skyrmion background, and then identify the singlet orders non-perturbatively through an enhanced correlations in the corresponding channels[33].

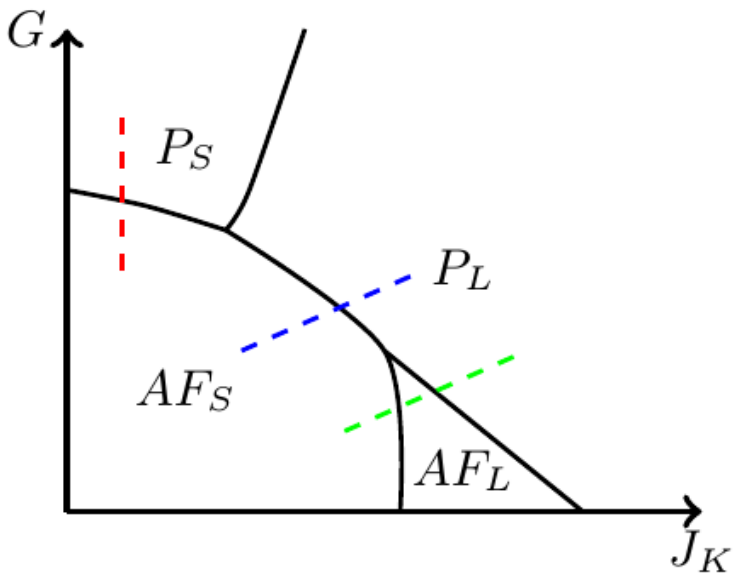

Figure 1.2 : Proposed global phase diagram for heavy fermion materials, where G is the degree of magnetic frustration and J_K is the Kondo coupling. Here, P and AF denote paramagnetic and antiferromagnetic phases, respectively. In the Kondo-screened phases where Kondo singlets are formed, the f-electron will also contribute to the Fermi surface so that the Fermi volume will be enlarged. The sub-indices S and L, which means small and large Fermi surfaces, respectively, mark the Kondo-destroyed and Kondo-screened phases, respectively. There are three types of transition between P and AF. The green line is a Hertz's type spin density wave transition, in which the Kondo destruction is inside the ordered part of the phase diagram. The blue line corresponds to the transition caused by Kondo destruction, while the red line denotes the transition caused by magnetic fluctuations alone. Adapted from Refs.[1, 2]

In the Kondo lattice model, we find two leading singlet channels, one in the spin Peierls and the other in the Kondo singlet. The relative stability of the Kondo singlet and spin Peierls channels is tuned by varying the Kondo coupling.

Motivated by the recent experimental result in geometrically frustrated heavy fermion metal CePdAl[34], in chapter 4, we study the RG calculation of QNLσM with a Kondo coupling. By treating both bosonic and fermionic degree in a equal footing, we perform a RG analysis of this model. Our RG analysis shows that Kondo coupling is irrelevant around the QCP of QNLSM. As a result, the phase transition between antiferromagnetism and paramagnetism should be stable against weak Kondo coupling. According to our calculation of the electronic self-energy induced by Kondo coupling around the QCP, we conclude that the Fermi surface also remains small against Kondo coupling. Together with chapter 3, our results shed new light on the global phase diagram of the heavy fermion systems.

Recent experimental results in $Ce_3Pd_{20}Si_6$ also provides an exciting extension of the global phase diagram to the heavy fermion materials with local multipolar levels[13]. In this coupound, the ground state of the local levels has a four-fold degeneracy, containing not only dipolar magnetic moments but also multipolar moments such as quadruple. Such four-fold dgeneracy can be expressed in therm of spin and orbital degree of freedom. This compound shows evidence of two consecutive Fermi surface collapsing QCPs as it is tuned from a paramagnetic to an antiferroquadrupolar and then to an antiferromagnetic state [13]. A theory was advanced[13] for a sequential destruction of Kondo entanglement in an spin-orbital-coupled Bose-Fermi Kondo(BFK) model, an effective model for a multipolar Kondo lattice. In chapter 5 we report an analytical renormalization group calculation of this spin-orbital BFK model with Ising anisotropy on bosonic bath, using a Coulomb-gas representation. We

show that a generic trajectory in the parameter space contains two QCPs associated with the destruction of the orbital and spin Kondo effects, respectively. Our work establishes a firm theoretical ground for the notion of sequential Kondo destruction.

Not only the heavy fermion systems, iron pnictides also provide a platform to study quantum criticality. The new ingredient here is that the quantum critical singularities in the nematic and magnetic channels are concurrent, and their relationship has yet to be clarified. In chapter 6, we study this problem within an effective Ginzburg-Landau theory for both channels in the presence of a small external uniaxial potential that breaks the lattice C_4 symmetry. We establish an identity that connects the spin excitation anisotropy, which is the difference of the dynamical spin susceptibilities at two ordering wave vectors $\vec{Q}_1 = (\pi, 0)$ and $\vec{Q}_2 = (0, \pi)$, with the dynamical magnetic susceptibility and static nematic susceptibility[35]. Using this identity, we introduce a scaling procedure to determine the dynamical nematic susceptibility in the quantum critical regime, and illustrate the procedure in the case of the optimally Ni-doped $BaFe_2As_2$[14]. Our analysis suggests that the singular energy dependences of spin excitation anisotropy and dynamical magnetic susceptibility observed in the optimally Ni-doped $BaFe_2As_2$ leads to the existence of non-trivial dynamical term $|\omega|/q^2$ in nematic susceptibility.

Chapter 2

Introduction

2.1 Landau-Ginzburg theory of classical phase transition

In the conventional Landau theory of phase transition, a phase of matter is related to a global symmetry and its spontaneous breaking. For instance, ferromagnetism breaks rotational symmetry, while paramagnetism preserves it, which is why the two represent distinct phases of matter. In the ordered phase the order parameter is non-vanishing and the symmetry is broken, while in the disordered phase, the order parameter vanishes and the symmetry is preserved. Phase transition happens when the system transforms between the ordered and disordered phases.

The basic idea of Landau-Ginzburg theory is that the free energy of the system can be expressed in terms of the order parameter and its fluctuations. We use a magnetic transition as an example, where the free energy functional F can be expressed in terms of the magnetic order parameter field $\phi(x)$:

$$\begin{aligned} F &= \int d^D x \left[\frac{t}{2}\phi^2(x) + K\left(\nabla\phi(x)\right)^2 + \frac{u}{4!}\phi^4(x) - h\phi(x) \right] \\ &= \int d^D p \phi(p) \left(\frac{t}{2} + Kp^2 \right) \phi(-p) \\ &+ \frac{u}{4!} \int d^D p_1 d^D p_2 d^D p_3 d^D p_4 \phi(p_1)\phi(p_2)\phi(p_3)\phi(p_4)\delta(p_1+p_2+p_3+p_4) \\ &+ h\phi(p=0) \end{aligned} \tag{2.1}$$

which is also called ϕ^4 theory, where $u > 0$ to ensure stability. The partition function

is:

$$Z = \int D\phi e^{-F} \tag{2.2}$$

where $D\phi \equiv \lim_{N\to\infty} \prod_{i=1}^{N} d\phi\left(x_i\right)$ is the measure of the path integral functional.

Without considering the spatial fluctuation and the external magnetic field, that is, $K = 0$ and $h = 0$, we can derive the mean-field solution of order parameter ϕ from the requirement that the solution minimizes the free energy functional F:

$$\frac{\partial F}{\partial \phi} = 0 \Rightarrow \phi\left(t + \frac{u}{6}\phi^2\right) = 0 \tag{2.3}$$

One can check that when $t < 0$, the solution is $\phi = \pm\sqrt{-\frac{6t}{u}}$, that is, the ordered phase. On the other hand, when $t > 0$ one get solution $\phi = 0$ corresponding to the disordered phase. At $t = 0$, the phase transition happens continuously.

Therefore, the parameter t measures the distance from the critical point. Without loss of generality, one can absorb the prefactor so that $t = \frac{T-Tc}{T_c}$, where T_c is critical temperature. Near a critical point, many physical quantities exhibit power-law behavior. The associated critical exponents are defined as:

$$\begin{aligned} C\left(t\right) &\propto t\partial_t^2 f|_{h=0} \sim |t|^{-\alpha} \\ \phi\left(t\right) &\propto \partial_h f|_{h=0} \sim |t|^{\beta} \\ \chi\left(t\right) &\propto \partial_h^2 f|_{h=0} \sim |t|^{-\gamma} \\ \phi\left(h\right) &\propto \partial_h f|_{t=0} \sim (h)^{\frac{1}{\delta}} \end{aligned} \tag{2.4}$$

where $f = -\frac{1}{\beta}\ln Z$ is the free energy density, C is the specific heat, and χ is the susceptibility. One can verify that the saddle point mean-field solution of Landau-Ginzberg model gives $\alpha = 0$, $\beta = 1/2$, $\gamma = 1$, and $\delta = 3$.

Fisher	$\nu(2-\eta)=\gamma$
Rushbrooke	$\alpha+2\beta+\gamma=2$
Widom	$\beta(\delta-1)=\gamma$
Josephson	$2-\alpha=\nu D$

Table 2.1 : Scaling relations for critical exponents

On the other hand, if the fluctuation effect is incorporated, then there are two other critical exponents associated with the correlation function:

$$G(x)\equiv\langle\phi(x)\,\phi(0)\rangle\sim\begin{cases}x^{-D+2-\eta}, & x\ll\xi\\ \exp\left(-\frac{x}{\xi}\right), & x\gg\xi\end{cases}\tag{2.5}$$

where η is called anomalous dimension, and ξ is the correlation length, which diverges in a power law manner near a critical point:

$$\xi\sim|t|^{-\nu}\tag{2.6}$$

One of the most incredible thing about critical phenomena is that these critical exponents actually are universal, in the sense that they are actually independent to the microscopic details of the model, but only dependent on the macroscopic properties, such as dimensionality and symmetry of the model, which means that many models that are different microscopically can in fact belong to the same universality class with the same critical exponents. Moreover, critical exponents are actually not independent of each other. They are satisfied the so-called scaling relations, as summarized in the table (2.1).

Since there are six critical exponents, while we have four constraints, the number

of real independent parameters should only be two. These scaling relations can be understood by scaling hypothesis[36]. The spirit is that near a critical point, the correlation length ξ is the only length scale and is divergent at a critical point, and hence the system should exhibit some sort of self-similarity and scale invariance. Under the rescale of length scale $\xi \to b\xi$, parameters t and h rescale as $t \to b^{y_t} t$, and $h \to b^{y_h} h$, and the free energy density f satisfies the scaling form:

$$f(t,h) = b^{-D} f\left(tb^{y_t}, hb^{y_h}\right) \tag{2.7}$$

for every b. Once we choose $tb^{y_t} = 1$, then

$$f(t,h) = t^{\frac{D}{y_t}} \tilde{f}\left(\frac{h}{t^{y_h/y_t}}\right) \tag{2.8}$$

Following this form and the definition of critical exponents in Eq. (2.4), (2.5) and (2.6), one can check that:

$$\begin{aligned} &\alpha = 2 - \frac{D}{y_t}, \quad \beta = \frac{D - y_h}{y_t}, \quad \gamma = \frac{2y_h - D}{y_t} \\ &\delta = \frac{y_h}{D - y_h}, \quad \nu = \frac{1}{y_t}, \quad \eta = 2 + D - 2y_h \end{aligned} \tag{2.9}$$

We see that the two independent parameters y_t and y_h define the six critical exponents, and more remarkably, the Eq. (2.9) indeed satisfy the scaling relations in Table. (2.1). As a result, by deriving scaling factors y_t and y_h we can derive other critical exponents.

The success of applying scaling theory to understand the critical phenomena help to the development of renormalization group(RG). By performing RG calculation, one can not only identify different phases or critical points hidden in a model but also derive the critical exponents from the first principle. The procedure of RG consists of the following steps[37]:

1.*Coarse-Grain*: The first step of the RG is to decrease the resolution of the length scale. For the ϕ^4 theory (2.1) as an example, this is usually achieved by divided the fields $\phi(q)$ into fast and slow modes:

$$\phi(\vec{q}) = \begin{cases} \phi_<(q), & 0 < |\vec{q}| < \frac{\Lambda}{b} \\ \phi_>(q), & \frac{\Lambda}{b} < |\vec{q}| < \Lambda \end{cases} \tag{2.10}$$

where $b > 1$ and Λ is the momentum cut-off of the model, and then integrate out the fast-mode $\phi_>$.

2. *Rescale* After integrate out the fast modes, we need to restore the length scale to the original one, which is achieved by rescaling the position:

$$x \to \frac{x}{b} \tag{2.11}$$

or equivalently, in the momentum space:

$$p \to bp \tag{2.12}$$

and the fields also need to be rescaled so that the leading term that governs the behavior of free theory(in this case, the $K(\nabla\phi)^2$) should be invariant:

$$\phi(q) \to b^{d_\phi}\phi \tag{2.13}$$

3. *Renromalize*:

In the end, the action retains its original form, but with a different set of parameters:

$$F = \int d^D x \left[\frac{t'}{2}\phi^2(x) + K(\nabla\phi(x))^2 + \frac{u'}{4!}\phi^4(x) - h'\phi(x)\right] \tag{2.14}$$

Let $G = \{g_\alpha\}$ denotes the set of parameters of the model g_α. In this case, $G = (t, u, h)$. After a RG procedure R, it transform to $G' = \{g'_\alpha\}$:

$$G' = \tilde{R}(G) \tag{2.15}$$

where the operation $\tilde{R}(G)$ describes the effects of the RG procedure of the system. Iterate the RG procedure can generate the flow of parameters along with each RG procedure, which is also called RG flow. By setting the parameter $l = \ln b$ and taking it as infinitesimal value, one can derive the RG flow:

$$\frac{dG}{dl} = \beta(G) \tag{2.16}$$

where $\beta(G) = \lim_{l\to 0} l^{-1}\left(\tilde{R}(G) - G\right)$ is called β functions.

For the ϕ^4 theory, up to the second order, the β functions are:

$$\begin{aligned}
\frac{dt}{dl} &= 2t + \frac{u^2}{16\pi^2} - \frac{tu}{16\pi^2} \\
\frac{du}{dl} &= \epsilon u - \frac{3u^2}{16\pi^2} \\
\frac{dh}{dl} &= \frac{6-\epsilon}{2} h
\end{aligned} \tag{2.17}$$

where $\epsilon = 4 - D$.

As we discussed, a characteristic of a critical point is the self-similarity. Any self-similar configurations must correspond to a fixed point G^* satisfying $G^* = \tilde{R}(G^*)$, that is:

$$\left.\frac{dG}{dl}\right|_{G=G^*} = \beta(G^*) = 0 \tag{2.18}$$

The RG flow near the vicinity of a fixed point can be further explored by linearizing the β functions:

$$\frac{dG}{dl} = \beta\left(G\right) \cong W\left(G - G^*\right) \tag{2.19}$$

where $W_{ab} = \frac{\partial \beta_a}{\partial g_b}\Big|_{G=G^*}$. One can diagonalize matrix W and identify its left eigenvectors ϕ_α with associated eigenvalues λ_α:

$$\phi_\alpha^T W = \lambda_\alpha \phi_\alpha^T \tag{2.20}$$

and then the RG flow near the vicinity of fixed point G^* can be expressed in a more suitable basis set $\{v_\alpha\}$:

$$v_\alpha = \phi_\alpha^T \left(G - G^*\right) \tag{2.21}$$

It is easy to check that:

$$\frac{dv_\alpha}{dl} = \lambda_\alpha v_\alpha \rightarrow v_\alpha\left(l\right) = \exp\left(l\lambda_\alpha\right) \tag{2.22}$$

Therefore, for $\lambda_\alpha > 0$, the trajectory of RG procedure flows away from the critical point G^*, while for $\lambda_\alpha < 0$ it flows toward G^*. The associated scaling field for the former case is said to be *relevant*, in the sense that it forcefully drives the system away from the critical point, and for the latter case *irrelevant*. For the case $\lambda_\alpha = 0$, we call the associated fields *marginal*.

A *Stable fixed point* is a point where all associated scaling fields are all irrelevant or exactly marginal. In RG language, these points correspond to a "phases of matter", since when one start initial parameters somewhere in the parameter space surrounding any of these attractors, the RG trajectory will flow towards one of these points and eventually arrive it, i.e. it is not only self-similar but also stable against any small perturbation, and thus genuinely represents what we call a state of matter.

On the other hand, a critical point is a fixed point where there are both relevant and irrelevant scaling fields. These points correspond to a continuous phase transitions, since tuning a relevant parameter around it can change the final destination of the RG flow trajectory, and thus change the state of matter.

For the ϕ^4 theory (2.1), one can identify the critical points from its β functions (2.17):

$$(t_1^*, u_1^*, h^*) = (0, 0, 0)\,, \quad (t_2^*, u_2^*, h^*) = \left(-\frac{1}{6}\epsilon, \frac{16\pi^2}{3}\epsilon, 0\right) \tag{2.23}$$

where the first one is called the Gaussian fixed point, and the second one is called the Wilson-Fisher fixed point.

The Wilson-Fisher fixed point only exists at $\epsilon > 0$, that is, $D < 4$, since u must be positive. However, since it has less relevant operator than the Gaussian fixed point, at $D < 4$ it should be the fixed point that control the critical behaviors. On the other hand, at $D > 4$ the critical phenomenon of ϕ^4 theory is described by the Gaussian fixed point. To understand the full RG flow diagram at $D < 4$, one can linearize the β functions (2.17) around the Gaussian and the Wilson-Fisher fixed point. Denoting the linearized mappings by W_1 and W_2 for the Gaussian and the Wilson-Fisher fixed point, respectively, we have:

$$W_1 = \begin{pmatrix} 2 & \frac{1}{16\pi^2} & 0 \\ 0 & \epsilon & 0 \\ 0 & 0 & \frac{6-\epsilon}{2} \end{pmatrix}, \quad W_2 = \begin{pmatrix} 2 - \frac{1}{3}\epsilon & \frac{1}{16\pi^2} & 0 \\ 0 & -\epsilon & 0 \\ 0 & 0 & \frac{6-\epsilon}{2} \end{pmatrix} \tag{2.24}$$

by which the associated critical exponents can be derived:

1. For the Gaussian fixed point, $y_t = 2$ and $y_h = \frac{6-\epsilon}{2} = 1 + \frac{D}{2}$. Compare these with Eq. (2.9), we have:

$$\alpha = 2 - \frac{D}{2},\ \beta = -\frac{1}{2} + \frac{D}{4},\ \gamma = 1,\ \delta = \frac{D+2}{D-2},\ \nu = 1,\ \eta = 0 \tag{2.25}$$

2. For the Wilson-Fisher fixed point, $y_t = 2 - \frac{1}{3}\epsilon$ and $y_h = \frac{6-\epsilon}{2} = 1 + \frac{D}{2}$, and hence the critical exponents are:

$$\alpha = \frac{\epsilon}{6},\ \beta = \frac{1}{2} - \frac{\epsilon}{6},\ \gamma = 1 + \frac{\epsilon}{6},\ \delta = 3 + \epsilon,\ \nu = \frac{1}{2} + \frac{\epsilon}{12},\ \eta = 0 \tag{2.26}$$

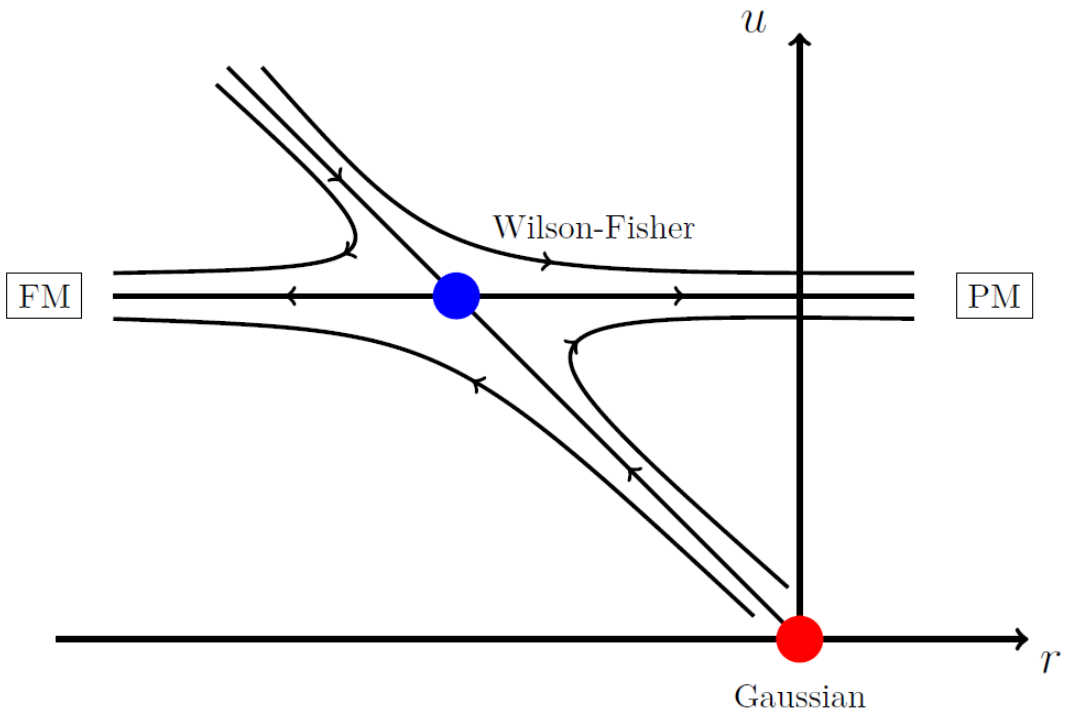

Figure 2.1 : The RG flow of ϕ^4 theory (2.1) at $D < 4$ obtained from the ϵ-expansion, where the FM and PM denote paramagnetic and ferromagnetic phase, respectively.

2.2 Quantum phase transition

The quantum phase transition is driven by quantum fluctuations. In the classical phase transition driven by thermal fluctuations, the spatial and temporal fluctuations are essentially decoupled. On the other hand, for quantum phase transitions, they

are generically intertwined[18, 19]. Therefore, the correlation time ξ_τ is related to the correlation length ξ:

$$\xi_\tau \sim \xi^z \tag{2.27}$$

where z is called dynamical exponent.

The energy scale of quantum fluctuation can be estimated through $\hbar\omega_c$, where $\omega_c \sim \frac{1}{\xi_\tau}$ is the characteristic frequency of the system. Since near a thermal-driven transition with critical temperature T_c, the correlation length scales as $\xi \sim |t|^{-\nu}$, where $t = \frac{T-T_c}{T_c}$, the energy scale of quantum fluctuation hence is:

$$\hbar\omega_c \propto |t|^{\nu z} \tag{2.28}$$

On the other hand, the energy scale of thermal fluctuations is $k_B T$, where k_B is the Boltzmann constant. The quantum fluctuations will be important as long as their energy scale is larger than the thermal one, that is, $\hbar\omega_c > k_B T$. However, from Eq. (2.28), we see that if $T \neq 0$, then at a temperature close enough to the critical temperature T_c, one must have $\hbar\omega_c < k_B T$. In other words, it is always the thermal fluctuations that dominate the critical behaviors of phase transition in the end. Following this simple estimation, one can conclude that the quantum phase transition can only happen at zero temperature.

Therefore, a quantum critical point(QCP) must be approached by a non-thermal tuning variable r. Near a QCP, the interplay of quantum and thermal fluctuations leads to a very rich phase diagram. Depending on the strength of quantum and thermal fluctuations, the phase diagram can be divided into different regions. To elucidate it, again we rely on the comparison between the energy scale of quantum and thermal fluctuations. Suppose a quantum phase transition takes place at $r = r_c$,

then similar as thermal-driven phase transition Eq.(2.28), we have $\xi \sim |r - r_c|^{-\nu}$ and:

$$\hbar\omega_c \propto |r - r_c|^{\nu z} = \Delta \tag{2.29}$$

where we define $\Delta \equiv |r - r_c|^{\nu z}$. As shown in Fig. 2.2, the regions where $k_B T < \Delta$ corresponds to quantum ordered or disordered phases, and the conventional quasiparticle paradigm is applicable. On the other hand, within $k_B T > \Delta$, the thermal and quantum fluctuations interplay with each other, and drastically influence the thermal excitation of the system. The quasiparticle paradigm thus becomes invalid.

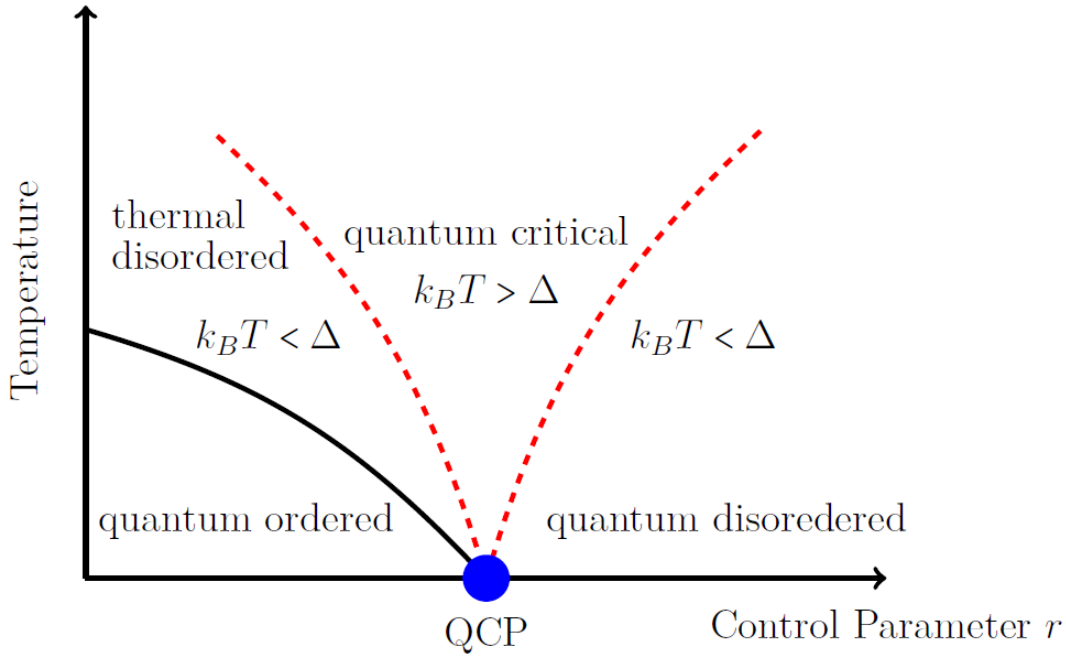

Figure 2.2 : A schematic overall phase diagram of quantum phase transition.

Similar to the classical critical point, near a QCP, lots of physical quantities also obey scaling behavior. The quantum scaling hypothesis assumes that under the

rescale of parameters, the free energy density satisfies the scaling form:

$$f\left(r-r_c,T,h\right)=b^{-(D+z)}f\left(b^{y_r}\left(r-r_c\right),b^zT,b^{y_h}h\right) \tag{2.30}$$

Compare it with the scaling hypothesis of classical phase transition (2.7), we can see that it implies that the effective dimension of a quantum phase transition $D_{\text{eff}}=D+z$.

There are many interesting models exhibiting quantum phase transition. In the following, we would like to introduce two essential toy models describing different kinds of magnetic phase transitions.

2.2.1 Hertz-Millis theory

Hertz-Millis theory aims to study the itinerant magnetic phase transition, where the magnetism is mainly induced by the Fermi surface instability of itinerant electron[38, 39]. The starting microscopic Hamiltonian is the Hubbard model[40]:

$$H=-\sum_{\langle ij\rangle\sigma}t_{ij}c_{i\sigma}^{\dagger}c_{j\sigma}+U\sum_i n_{i\uparrow}n_{i\downarrow} \tag{2.31}$$

where $c_{i\sigma}^{\dagger}$ and $c_{i\sigma}$ creates and destroys a electron on site i with spin σ, respectively, and $n_{i\sigma}=c_{i\sigma}^{\dagger}c_{i\sigma}$ is the number of electron on site i with spin σ.

The on-site Coulomb interaction can be expressed as $n_{i\uparrow}n_{i\downarrow}=1/4\left[\left(n_{i\uparrow}+n_{i\downarrow}\right)^2+\left(n_{i\uparrow}-n_{i\downarrow}\right)^2\right]$. Since we aim to study the magnetic phase transition, we ignore the charge density fluctuation $\left(n_{i\uparrow}+n_{i\downarrow}\right)^2$. By using the Hubbard-Stratonovich transformation with the field ϕ conjugating with spin density fluctuation $n_{i\uparrow}-n_{i\downarrow}$, the Hubbard interaction can be decoupled. After integrating out the fermionic degree of freedom, and express the effective action in terms of the power series of ϕ field, the resulting Hertz-Millis model is:

$$S = \sum_{i\omega_n, \vec{q}} \left(r + q^2 + \gamma \frac{|\omega_n|}{q^a} \right) |\phi\left(i\omega, \vec{q}\right)|^2 + \frac{u}{4} \int d\tau d^D x |\phi\left(\tau, \vec{x}\right)|^4 \tag{2.32}$$

The Hertz-Millis theory (2.32) can be regarded as a quantum generalization of the classical ϕ^4 theory (2.1). The difference is that, in the Hertz-Millis theory, the temporal fluctuations also interplay with spacial fluctuations, and influence the critical behaviors. Note that in the quadratic term of the action (2.32), there is a non-trivial dynamical term $\gamma|\omega_n|/q^a$ called Landau damping, which results from the particle-hole polarization of electron near Fermi surface, and $a = 1 (a = 0)$ for spin density wave(ferromagnetic) transition. Therefore, to assure that the action (2.32) is invariant under rescaling $q \to bq$, $\omega \to b^z \omega$, we must have:

$$z = 2 + a \tag{2.33}$$

and hence the effective dimension of Hetz-Millis theory is $D_{\text{eff}} = D + z = D + 2 + a$.

After performing RG procedure up to one-loop level, the β functions of the Hertz-Millis theory (2.32) are:

$$\begin{aligned} \frac{dT}{dl} &= zT \\ \frac{dr}{dl} &= 2r + u^2 f_2\left(T, r\right) \\ \frac{du}{dl} &= \left(4 - D - z\right) u - u^2 f_4\left(T, r\right) \end{aligned} \tag{2.34}$$

As we said, the Herz-Millis model is like a generalization of ϕ^4 theory but only with effective dimension $D_{\text{eff}} = D + z$ modified due to the temporal fluctuation. Therefore, at $D_{\text{eff}} = D + z > 4$, coupling constant u should be irrelevant, and hence the QCP should correspond to a Gaussian fixed point. After solving these β functions, one can even derive the RG flow and the scaling behaviors. In the end, according to the

scaling behaviors, the whole phase diagram can be divided into different regions, as summarized in Fig. 2.3.

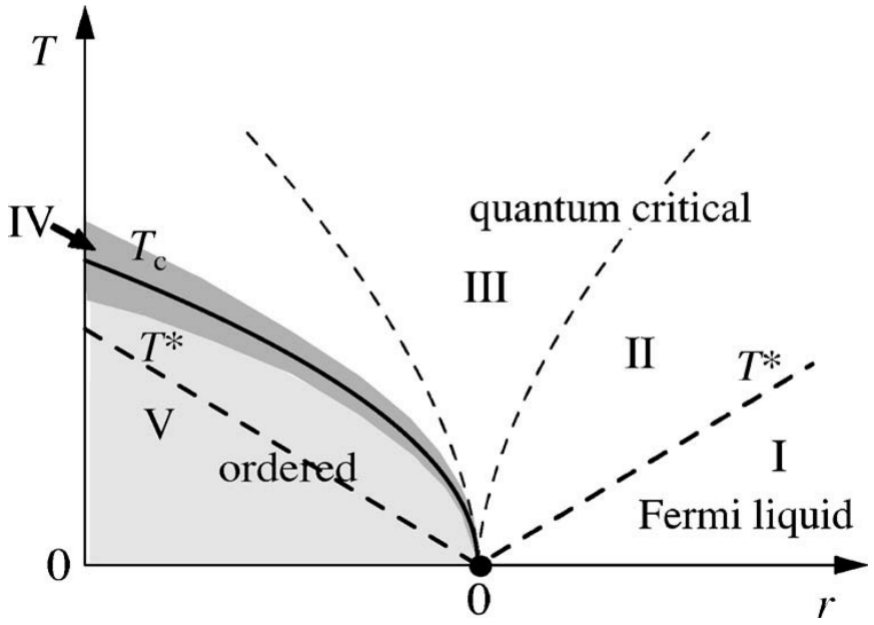

Figure 2.3 : The schematic phase diagram of the Hertz-Millis theory. Regime I is a magnetic disorederd Fermi liquid. II and III are quatum critical regime, with different scaling behavior of correlation length. IV is a Non-Gausssian classical crtical regime. V is a magnetic ordered phase. Figure adapted from reference [3].

Note that in the derivation of action (2.32) from the Hubbard model, we actually assume that except the quadratic term from fermionic particle-hole polarization, other higher-order terms resulting from integrating out fermionic modes is constant and independent of the external momentum and frequency. This assumption, however, can actually fail, and it turns out dramatically changing the nature of itinerant magnetic phase transition[41, 42, 43]. Nonetheless, due to its simplicity and ability to demonstrate lots of general features of the quantum criticality, the Hertz-Millis model is still regarded as one of the most important prototype to study quantum phase transitions.

2.2.2 Quantum Non-Linear Sigma model

The Hertz-Millis theory addresses the quantum criticality of itinerant magnetism. Its microscopic origin is the Hubbard model (2.31). At the strong on-site Coulomb interaction limit $U \to \infty$, since any double occupancy of electrons at each site cost much more energy, the electrons would like to avoid this circumstance and tend to stay at each site. Therefore, the electrons are localized, and the picture of the itinerant electrons is no longer a good starting point. The transition from itinerant metal to localized insulator due to strong Coulomb interaction is called the Mott transition[25]. This kind of insulator is also called the Mott insulator and is different from the conventional band insulator which can be understood within the non-interacting band theory.

For the single band Hubbard model at half-filling case, each site is occupied by a localized single electron. Because of the hopping term t, these localized electrons can still interact with each other through the super-exchange mechanism[44], and the final effective Hamiltonian is:

$$H = J_H \sum_{ij} \vec{S}_i \cdot \vec{S}_j \tag{2.35}$$

where $J_H \sim t^2/U$, and $\vec{S}_i$ is the local moment spin operator of a localized electron on site i.

The model (2.35) is also called the Heisenberg model, which is a quantum generalization of the classical Ising model. Even though it is hard to derive the exact solution of the Heisenberg model, some of progress can still be made. By starting from an antiferromagnetic(AF) ordered phase, D. Haldane developed a way to semi-classically approximate the Heisenberg model (2.35) into a continuum field theory[45, 46], in which the local moment operator $\vec{S}_i$ is represented by the non-linear sigma field $\vec{n}\,(\vec{x}, \tau)$ char-

actering the classical Neel order of AF ordered phase, and the canting field $\vec{L}(\vec{x},\tau)$ describing the fluctuation around the non-linear sigma field $\vec{n}(\vec{x},\tau)$:

$$2\vec{S}_i \to e^{i\vec{Q}\cdot\vec{x}}\vec{n}(\vec{x},\tau)\sqrt{1-\left(2a^D\vec{L}(\vec{x},\tau)\right)^2}+2a^D\vec{L}(\vec{x},\tau) \tag{2.36}$$

where $\vec{Q}$ is the ordering wave vector, $\vec{x}$ labels the position, a is the lattice constant, $\vec{n}(\vec{x},\tau)\cdot\vec{L}(\vec{x},\tau)=0$, and $|\vec{n}(\vec{x},\tau)|=1$. For the sake of simplicity, in the following, we take the square lattice with ordering wave vector $\vec{Q}=\left(\frac{\pi}{a},\frac{\pi}{a}\right)$ as an example. All of the results can be easily generalized in other cases.

After putting (2.36) into the Heisenberg model (2.35), and taking the continuum limit, one will end up with a continuum field theory S_H:

$$\begin{aligned} S_H &= S_n + S_B \\ S_n &= \frac{1}{2g}\int d\tau d^D x\left(\frac{1}{c^2}\left(\partial_\tau\vec{n}\right)^2+\left(\nabla\vec{n}\right)^2\right) \end{aligned} \tag{2.37}$$

where $g=\frac{a^{D-2}}{S^2}\frac{J_1}{J_1-2J_2}$, $c=2aSJ_1\sqrt{D}\sqrt{\frac{J_1-2J_2}{J_1}}$($J_1$ and J_2 is the nearest-neighbor and next-nearest-neighbor interaction, respectively). The topological term S_B results from the Berry phase effect of path integral, and is vanishing inside the AF ordered phase.

Because of the non-linear constraint $|\vec{n}(\vec{x},\tau)|=1$, the QNL$\sigma$M (2.37) actually contains infinite number of local interaction. However, due to the $O(N)$ symmetry, the QNLσM (2.37) is still renormalizable[47, 48, 49]. The RG flow of the temperature T and the coupling constant g can be explored through the following β functions[50]:

$$\begin{aligned} \frac{d\tilde{t}}{dl} &= -(D-2)\tilde{t}+(N-2)\frac{K_D}{2}\tilde{g}\tilde{t}\coth\left(\frac{\tilde{g}}{2\tilde{t}}\right) \\ \frac{d\tilde{g}}{dl} &= -\epsilon\tilde{g}+(N-2)\frac{K_D}{2}\tilde{g}^2\coth\left(\frac{\tilde{g}}{2\tilde{t}}\right) \end{aligned} \tag{2.38}$$

where $\epsilon=D+z-2=D-1$, $\tilde{g}=c\Lambda^{D-1}g$, and $\tilde{t}=\Lambda^{D-2}gT$.

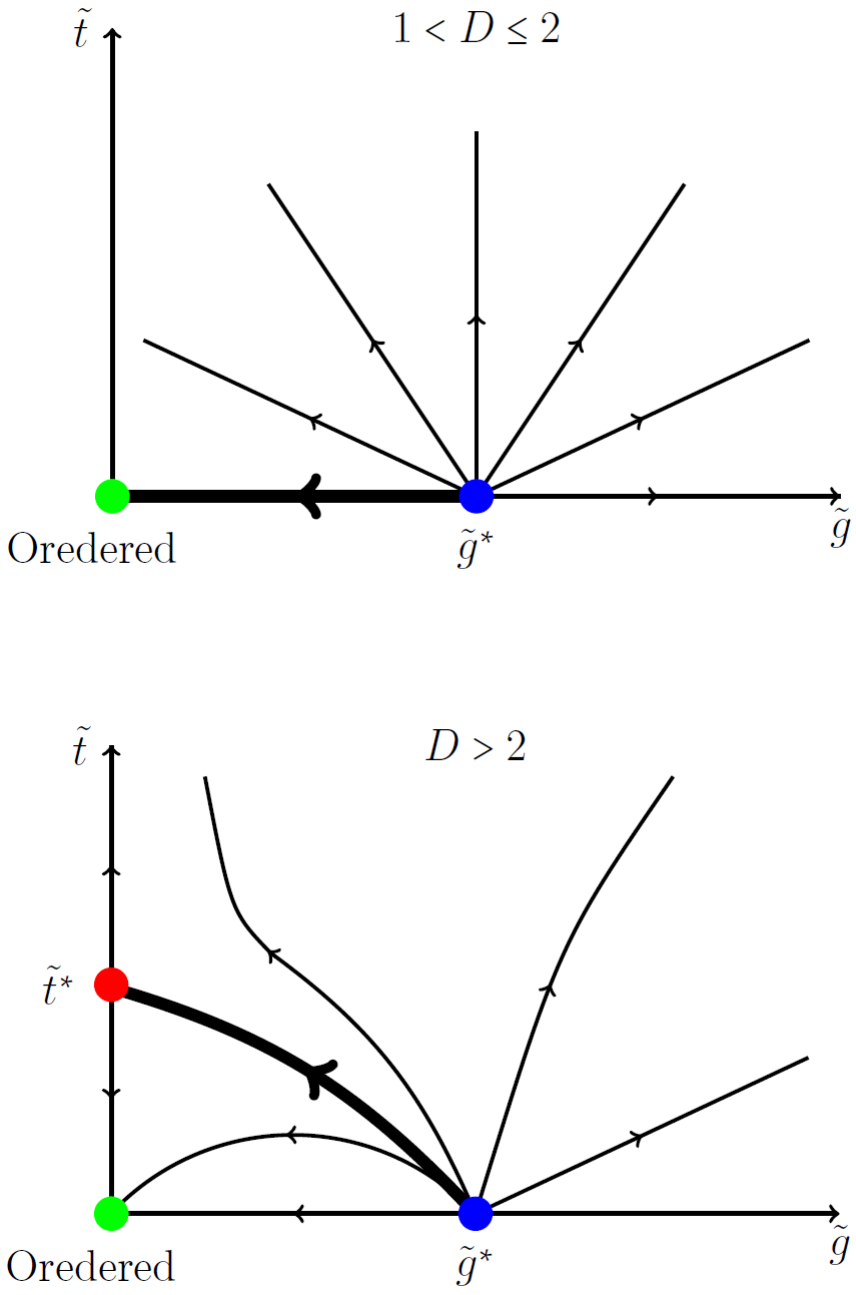

Figure 2.4 : RG flow diagram of the quantum non-linear sigma model for $1 < D \leq 2$(Up) and $D > 2$(Down). At $D > 1$, there is a QCP $\tilde{g} = \tilde{g}^*$ separating the quantum ordered and disordered phase. Thick lines are the phase boundary. At $1 < D \leq 2$, such ordered phase only exists at zero temperature.

From these β functions (2.38), one can see that at $D = 1$, the coupling constant g is relevant, which indicates that the ground state should be AF disordered. Large-N mean-field solution also predicts that there is a massive gap dynamically generated due to quantum fluctuation[51]. The whole RG flow at $D > 1$ are plotted in Fig. 2.4. At $T = 0$, there is a QCP separating the AF ordered and disordered phase.

Until now, we have not yet considered the influence of the topological term S_B. It is vanishing inside the AF ordered phase. However, at $D = 1$, the coupling constant is relevant and flows to the AF disordered fixed point. The influence of the topological term S_B should also be incorporated[45]. Such topological term has a local expression:

$$S_B(\vec{n}) = \frac{iS}{2} \int d\tau dx \vec{n} \cdot (\partial_x \vec{n} \times \partial_\tau \vec{n}) = 2i\pi SQ \tag{2.39}$$

where Q is an integer since the non-linear sigma field $\vec{n}$ is a mapping from S^2 to S^2 if we assign $\vec{n}\left(\sqrt{x^2+\tau^2} \to \infty\right) = 1$, and the homotopy group $\Pi_2(S^2) = Z$. The configurations of $\vec{n}$ that give non-vanishing Q is called skyrmion. Fig. (2.5) shows the profile of a skyrmion with $Q = -1$.

From the relation (2.39), we see that if S is an integer, then the influence of the topological term should be irrelevant since $e^{S_B} = 1$. However, if S is a half-integer, then this term $e^{S_B} = (-1)^Q$ depends on the integer Q. Following all of these analyses, Haldane conjectured that $D = 1$ spin chain should be an gapped AF disordered phase and gapless ordered phase if S is an integer and half-integer, respectively[45].

At $D = 2$, as we have seen, there is a QCP separating AF ordered and disordered phase, and the topological term is vanishing inside the ordered phase. However, it is still useful to consider the consequence of topological defects, since by which one can infer the physics on the disordered side. At $D = 2$, it turns out that the skyrmion defects do not contribute to the partition function[52]. However, aother kind of defect called hedgehog, which can be regarded as a skyrmion number changing event in the

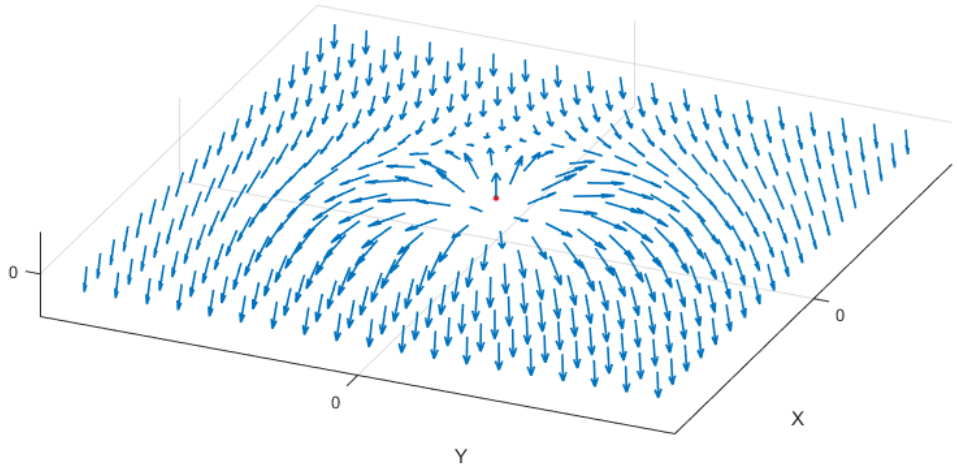

Figure 2.5 : Profile of a skyrmion with $Q = -1$.

space-time(see Fig. 2.6), can still dramatically changes the nature of the QCP and the ground state of the AF disordered phase. As a result, once they proliferate, these defects can cause some exotic phase transitions that are forbidden in the Landa-Ginzburg paradigm [53, 54, 55, 56].

2.3 Heavy Fermions

We have introduced two prototypical models for different kinds of magnetic quantum criticality. One is Herz-Millis model that aims to address itinerant spin density wave or ferromagnetic quantum phase transitions, and the other is quantum non-linear sigma model that comes from localized magnetism. The itinerant and localized picture seems to be quite opposite and hard to be reconciled. One way to make progress is to consider the interplay of these two seeming opposite pictures. Heavy fermion materials is an ideal system for such study.

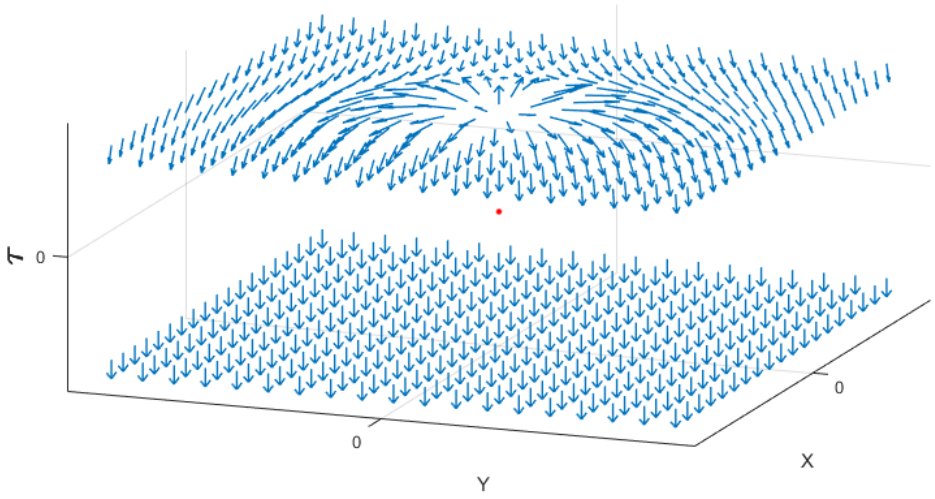

Figure 2.6 : Profile of a hedgehog defect in the space-time.

Heavy fermion systems refer to the intermetallic compounds that involve rare-earth or actinide elements, which contribute 4f or 5f electrons. The on-site Coulomb interaction is strong in the f-orbitals so that the f-electrons are highly localized and form local moments on each site. These local moments interact with itinerant conduction electrons through the antiferromagnetic Kondo coupling, and also interact with each other through the so called Ruderman–Kittel–Kasuya–Yosida(RKKY) interaction mediated by conduction electrons[57, 58, 59]. The effective Hamiltonian describing heavy fermion systems is Kondo lattice model H_K:

$$
\begin{aligned}
H_K &= H_c + H_f + H_K \\
H_c &= \sum_{\vec{k}\sigma} \epsilon_{\vec{k}} c^\dagger_{\vec{k}\sigma} c_{\vec{k}\sigma} \\
H_f &= \sum_{ij} J_{H,ij} \vec{S}_i \cdot \vec{S}_j \\
H_K &= \sum_i J_K \vec{S}_i \cdot \vec{s}_{c,i}
\end{aligned}
\tag{2.40}
$$

where $\vec{s}_{c,i} = \sum_{\alpha\beta} c^\dagger_{i\alpha} \frac{\vec{\sigma}_{\alpha\beta}}{2} c_{i\beta}$ is the spin of conduction electron on site i.

Since the RKKY interaction is generated by coupling with conduction electron, its strength depends on the Kondo coupling as $J_{H,ij} \propto \rho_0 J_K^2$. On the other hand, below the Kondo temperature scale $T_K \propto \exp\left(-1/\left(\rho_0 J_K\right)\right)$, the conduction electrons and f-electrons should form singlets called Kondo singlet. These two energy scale compete with each other. At weak Kondo coupling $J_K \to 0$, the RKKY coupling $J_{H,ij} \gg T_K$. Therefore, the conduction electrons and the local moments are essentially decoupled, and the magnetism of the is dominant by the RKKY interaction H_f, which usually prefer AF ordered phase formed by local moments.

On the other hand, at strong Kondo coupling limit $J_K \to \infty$, we have $J_{H,ij} \ll T_K$. Consequently, it should be the Kondo coupling that dominates, and thus the Kondo singlets between conduction and f-electrons are formed, which breaks the antiferromagnetic orders formed between the local moments and lead the system into paramagnetism. To explore the nature of the ground state in this case, we use the pseudofermion representation to represent the local moment operator $\vec{S}_i$[60]:

$$
\vec{S}_i = \frac{1}{2} \sum_{\alpha\beta} f^\dagger_{i\alpha} \frac{\vec{\sigma}_{\alpha\beta}}{2} f_{i\beta} \tag{2.41}
$$

with the constraint $\sum_\sigma f^\dagger_{i\sigma} f_{i\sigma} = 1$, which is usually satisfied at the mean-field level

by introducing new variable λ_i

$$\sum_{i\alpha} \lambda_i \left(f^\dagger_{i\alpha} f_{i\alpha} - 1 \right) \tag{2.42}$$

into the action.

By using this pseudo-fermion representation, one can decouple the Kondo coupling into Kondo hybridization channel through Hubbard-Stratonovich transformation:

$$\sum_i J_K \vec{S}_i \cdot \vec{s}_{c,i} \to \sum_{i\sigma} \left(V_i c^\dagger_{i\sigma} f_{i\sigma} + h.c \right) + \sum_i \frac{|V_i|^2}{J_K} \tag{2.43}$$

When Kondo coupling dominates and Kondo singlet is formed, both V_i and λ_i will acquire non-vanishing static expectation value. Therefore, we can replace these dynamical variables with their static saddle-point value $V_i \to V$ and $\lambda_i \to \lambda$, and the resulting mean-field Kondo lattice model H_{KMF} is:

$$H_{KMF} = \sum_{k\sigma} \epsilon_k c^\dagger_{k\sigma} c_{k\sigma} + \lambda \sum_{i\alpha} \left(f^\dagger_{i\alpha} f_{i\alpha} - 1 \right) + V \sum_{i\sigma} \left(c^\dagger_{i\sigma} f_{i\sigma} + h.c \right) + \sum_i \frac{|V|^2}{J_K} \tag{2.44}$$

This mean-field Kondo lattice model (2.44) can be diagonalized. Because of the Kondo hybridization V, the elementary quasi-particle consists of both conduction electron and f-electron. As a result, under the global $U(1)$ gauge transformation, not only the conduction electron but also f-electron will also transform, and hence the f-electron should also contribute to the electronic transport properties so that the Fermi surface become much larger. This feature can been seen in the band structure of quasi-particle plotted in Fig. 2.7, where there are two bands separated by a gap called hybridization gap. The lower band is drastically flatten, so that the effective mass of quasi-particle and the Fermi surface become much larger if the Fermi energy

lies around the lower band, which is why these systems are called heavy fermion.

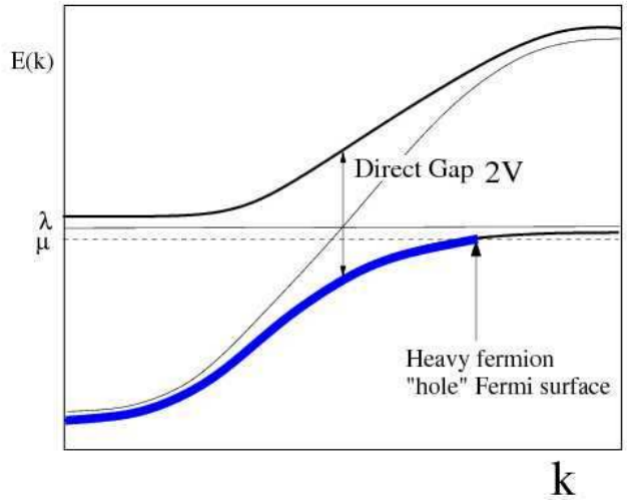

Figure 2.7 : Band structure of the mean-field Kondo lattice model (2.44). Thin solid lines denote the conduction electron band and the local f electron levels before the hybridization. Thick solid lines are the renormalized band of the heavy-quasiparticles composed of conduction electrons and f-electrons. Figure adapted from reference [4].

For these paramagnetic heavy quasi-particle systems, the conventional Fermi liquid theory is sufficient to explain lots of physical properties. In the Fermi liquid theory, the interactions only dress up the quasi-particles and change their parameters such as effective mass m^*, but do not break them. From quasi-particles picture one can derive the temperature T dependences of the specific heat $C \sim \gamma T$, the resistivity $\rho \sim \rho_0 + AT^2$, and the static spin susceptibility $\chi \sim$ Const at low temperature, where $\gamma \sim m^*$, $A \sim (m^*)^2$, and $\chi \sim m^*$. The Wilson ratio $W = \chi/\gamma$[61] and Kadowaki Woods ratio $\alpha_{KW} = A/\gamma^2$[62] in Fermi liquid theory should thus independent of effective mass m^*. Fig. 2.8 are the plots of for γ versus χ and A versus γ^2 of many heavy fermion compounds. The fact that they almost fit in with linear relations is a proof that the Fermi liquid description works pretty well for these heavy fermion systems.

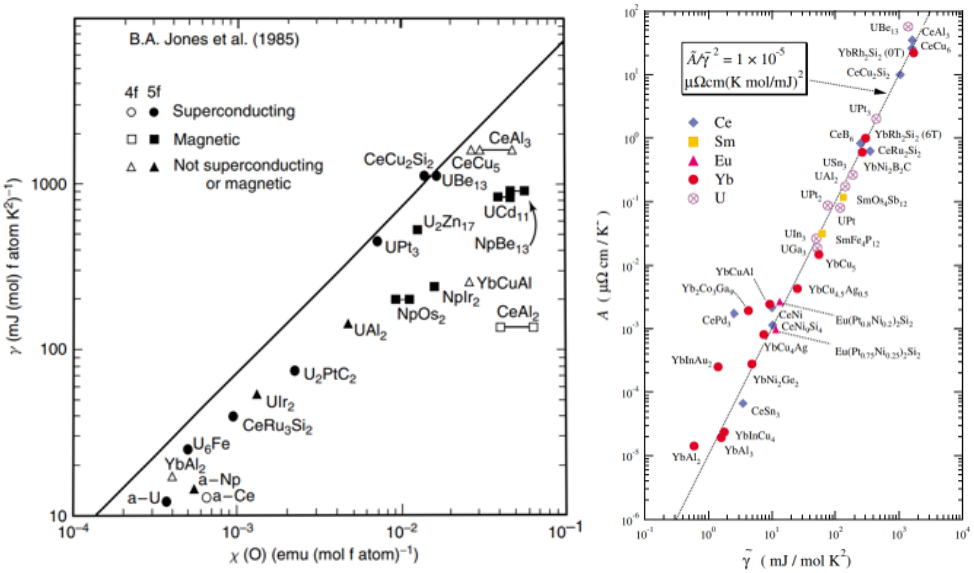

Figure 2.8 : Wilson ratio χ/γ(Left) and Kadowaki Woods ratio A/γ^2(Right) for a wide range of heavy fermion systems with different effective mass. Figures adapted from references [5](Left) and [6](Right).

Now we have explored the Kondo lattice model (2.40) in weak and strong Kondo limits $J_K \to 0$ and $J_K \to \infty$, and found that it corresponds to a antiferromagnetic Kondo-destroyed phase with small Fermi surface and paramagnetic Kondo-screened phase with large Fermi surface, respectively. As a result, there must be a phase transition between these two phases. In conventional Hert-Millis theory, the Kondo singlet destruction and the magnetic phase transition are treated as separated issues. However, experimental discoveries of ω/T scaling of spin suceptibility in $CeCu_{6-x}Au_x$ at $x = x_c \approx 0.1$[63] and $YbRh_2Si_2$[64] imply the inapplicability of Hertz-Millis theory to this transition, and it is believed that the Kondo singlet destruction and the magnetic phase transition take place simultaneously at such critical point.

A new concept called local quantum criticality has been proven successful to understand the ω/T scaling of spin suceptibility[65, 66]. In the local quantum criticality,

the breakdown of Kondo singlet is concurrent with the magnetic phase transition simultaneously. Since the breakdown of the Kondo singlet involves both the spin and charge degree of freedom, in the local quantum criticality scenerio, not only the the spin fluctuations but also the charge fluctuations should be singular around the magnetic quantum critical point[67, 68, 69, 70]. The correspondent ω/T scaling of optical conductivity has been already observed in the $YbRh_2Si_2$[71].

Because the Kondo destruction is local in space, a QCP like this violates the conventional Landau-Ginzburg paradigm. To demonstrate the local quantum criticality in Kondo lattice model (2.40), the extended dynamical mean field theory(EDMF) is used to self-consistently map the Kondo lattice model (2.40) to the Bose-Fermi Kondo model H_{BFK}[65]:

$$\begin{aligned} H_{BFK} &= H_0 + H_B + H_K \\ H_0 &= \sum_{\vec{k}\sigma} \epsilon_{\vec{k}} c^\dagger_{\vec{k}\sigma} c_{\vec{k}\sigma} + \sum_{\vec{q}} \omega_{\vec{q}} \vec{\phi}^\dagger_{\vec{q}} \cdot \vec{\phi}_{\vec{q}} \\ H_B &= g\vec{S} \cdot \sum_{\vec{q}} \left(\vec{\phi}^\dagger_{\vec{q}} + \vec{\phi}_{-\vec{q}} \right) \\ H_K &= J_K \vec{S} \cdot \vec{s}_c \end{aligned} \tag{2.45}$$

where $\vec{\phi}$ is a vector bosonic field, and the fermioninc and bosonic dispersion $\epsilon_{\vec{k}}$ and $\omega_{\vec{q}}$ are determined self-consistently. The Bose-Fermi Kondo model H_{BFK} (2.45) describe a local impurity with spin $\vec{S}$ couples with itinerant electron $c_{\vec{k}\sigma}$ and dissipative bosonic bath $\vec{\phi}$, as shown in Fig. 2.9. This impurity model is related to the original Kondo lattice model through the self-consistent condition:

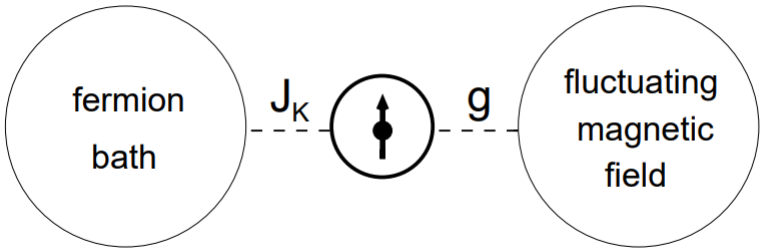

Figure 2.9 : Schematic diagram of Bose-Fermi Kondo model (2.45).

$$
\begin{aligned}
G_{\mathrm{loc},\sigma}\left(i\omega_n\right) &= \sum_{\vec{k}} G_\sigma\left(\vec{k}, i\omega_n\right) = \sum_{\vec{k}} \frac{1}{i\omega_n - \epsilon_{\vec{k}} - \Sigma\left(\omega_n\right)} \\
\chi_{\mathrm{loc},\sigma}\left(i\nu_n\right) &= \sum_{\vec{q}} \chi\left(\vec{q}, i\nu_n\right) = \sum_{\vec{q}} \frac{1}{I_{\vec{q}} + M\left(i\nu_n\right)}
\end{aligned}
\tag{2.46}
$$

where $G_\sigma\left(\vec{k}, i\omega_n\right)$ and $\chi\left(\vec{q}, i\nu_n\right)$ is fermionic Green's function and spin susceptibility on lattice, respectively.

For Bose-Fermi Kondo models H_{BFK} with various different spin symmetries, local quantum critical points have been identified by both numerical[72, 73, 74] and analytical[75, 76, 77] way. For spin $SU\left(2\right)$ symmetry case, one can perform a controllable ϵ-expansion RG calculation of the Bose-Fermi Kondo model H_{BFK} (2.45), where $\epsilon = 1 - s$ and s is the exponent of bosonic spectral function $\rho_b \propto \omega^2$ with $s < 1$[75]. The resulting β functions are:

$$
\begin{aligned}
\frac{dJ_K}{dl} &= J_K\left(J_K - g^2 - \frac{J_K^2}{2} + g^4\right) \\
\frac{dg}{dl} &= g\left(\frac{\epsilon}{2} - g^2 - \frac{J_K^2}{2} + g^4\right)
\end{aligned}
\tag{2.47}
$$

Fig. 2.10 shows the RG flow diagram of these β functions. The ω/T scaling around the local quantum critical point of spin $SU\left(N\right)$ symmetric Bose-Fermi Kondo

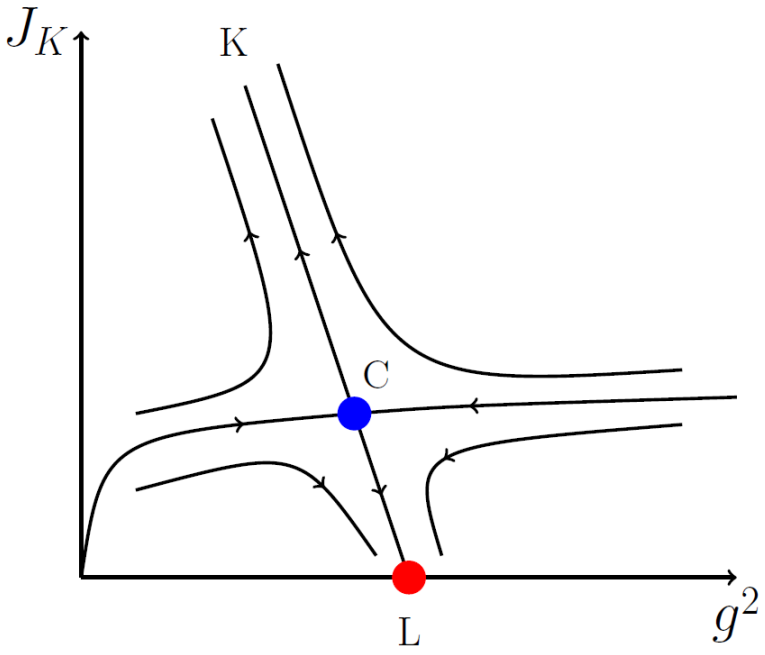

Figure 2.10 : The RG flow diagram for the Bose-Fermi Kondo model (2.45), where the blue dot C denotes the quantum critical point of the local quantum criticality, and red dot L is the local moment fixed point for a Kondo-destroyed phase. At large Kondo coupling, the RG trajectory flows toward the strong coupling Kondo-screened fixe point K.

model (2.45) has also been verified by dynamical large-N method[67], where N is the number of spin indices of conduction electron.

2.4 Iron Pnictides

The discovery of high-temperature superconductivity in iron-based materials has brought lots of surprises to physicist[78, 79]. The parent state of these materials are antiferromagnetism. For the iron pnictides, many evidences of bad-metal behavior have been found. One of them is from the Mott-Ioffe-Regel criterion, which compares the electron mean free path l with the Fermi wavelength $1/k_F$. For a good metal, their ratio $k_F l$, which is dimensionless, is much larger than unity. The fact

that, at room temperature, $k_F l \approx 1$ for the iron pnictides indicates that they are bad metals. Other evidences for the bad metal behavior, from optical conductivity measurement, are summarized in Fig. 2.12.

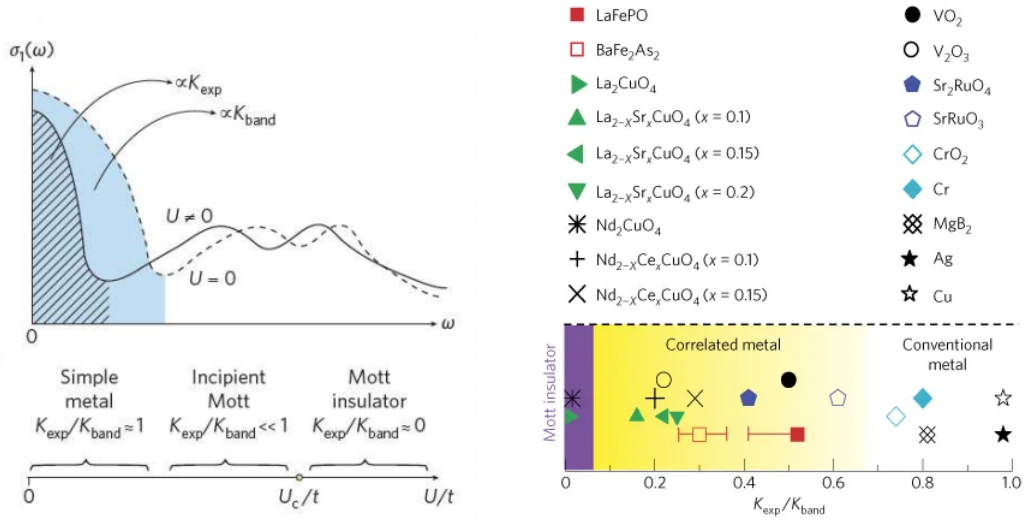

Figure 2.11 : Left: The optical conductivity $\sigma(\omega)$ versus frequency ω for the interacting($U \neq 0$) and non-interacting($U = 0$) case. K_{exp} and K_{band} is the measured Drude weight of $\sigma(\omega)$ for interacting and non-interacting case, respectively. Adapted from Ref. [7]. Right: The ratio of K_{exp} to K_{band} for various superconductors, including cuprate and iron pnictides. Adapted from Ref. [8].

Motivated by these evidences of bad metal behavior, it has been proposed that the electronic correlation in the parent state of iron pnictides is strong enough that the parent state can be regarded as "incipient Mott state"[80, 9]. In other words, they are metallic state but very close to the edge of the Mott transition. The electron spectral function versus energy is illustrated in Fig. 2.12, where the middle peak at the Fermi energy E_F is the coherent part which is responsible for the metallic behavior, and the other two peaks are the incoherent parts that are precursors of Hubbard bands in a Mott insulator. The ratio of the coherent part to the whole spectral weight is denoted as w, which is 0 for a Mott insulator since, here, there is no coherent part. For an

incipient Mott state, w should be very small. By using it as a control parameter, one can derive, at the zeroth order in w, the effective magnetic Hamiltonian so-called the J_1-J_2 model[81]:

$$H = J_1 \sum_{\langle ij \rangle} \vec{S}_i \cdot \vec{S}_j + J_2 \sum_{\langle\langle ij \rangle\rangle} \vec{S}_i \cdot \vec{S}_j \tag{2.48}$$

where J_1 and J_2 is the nearest-neighbor and next-nearest-neighbor coupling, respectively.

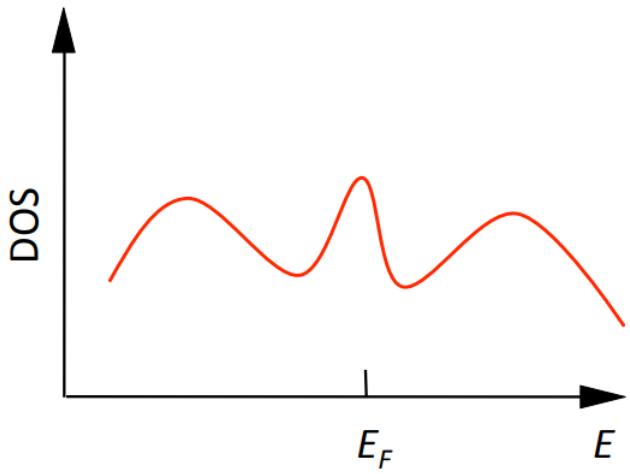

Figure 2.12 : Single-electron spectral function versus energy. Adapted from Ref.[9]

For the iron pnictides, the first-principle calculation suggests that $J_1 \sim 2J_2$[82] and both are antiferromagnetic[83]. When $J_1 < 2J_2$, the ground state of the classical limit of the J_1-J_2 model (2.48) is known to have the $O(3) \times O(3)$ symmetry consisting of two interpenetrating Neel lattices with independent Neel order parameter $\vec{m}_A$, and $\vec{m}_B$, as shown in Fig. 2.13, and the ground state energy is independent of the relative angle ϕ between $\vec{m}_A$ and $\vec{m}_B$. Such a huge degeneracy of the ground state can be broken by the quantum or thermal fluctuations, which pick the $\phi = 0$ or $\phi = \pi$ as the true ground state. As a result, the ground state possess not only the magnetic

order $\vec{m}_{A,B} \cdot \vec{m}_{A,B} \neq 0$ but also the Ising-nematic order $\vec{m}_A \cdot \vec{m}_B \neq 0$[84]. At higher temperatures, there is a window within which the magnetic order is vanishing, but the Ising-nematic order is still non-vanishing[85, 86]. Such a phase is called a nematic phase, and is related to the structural transition observed in the iron pnictides[87, 88].

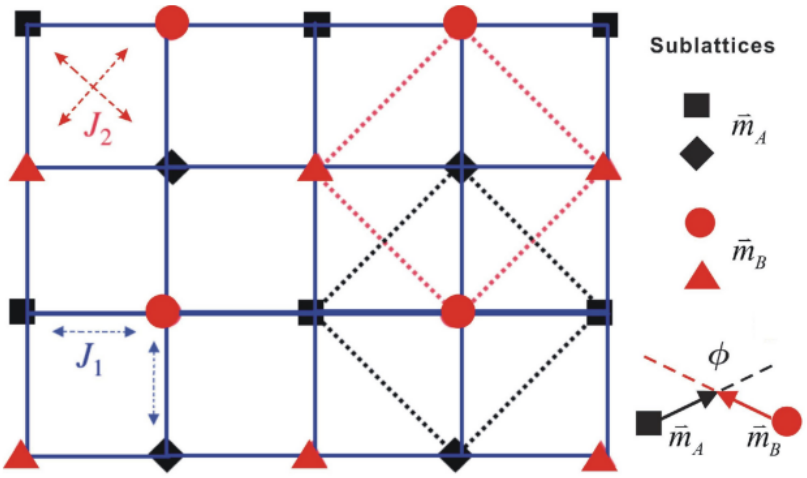

Figure 2.13 : Illustration of the J_1-J_2 model on a square lattice. The staggered magnetizations $\vec{m}_A$ and $\vec{m}_B$ are defined on two interpenetrating Neel square lattices. Adapted from Ref.[10].

In order to understand the phase diagram of the system that starts at the w^0 order with the J_1-J_2 model (2.48), one then study the Ginzburg-Landau description that incorporates the w-expansion (2.48)[80, 9] :

$$
\begin{aligned}
S_0 &= S_2 + S_4 \\
S_2 &= \sum_{q=\vec{q},i\omega_n} \left\{ G_0^{-1}(q) \left(|\vec{m}_A(q)|^2 + |\vec{m}_B(q)|^2 \right) + v \left(q_x^2 - q_y^2 \right) \vec{m}_A(q) \cdot \vec{m}_B(-q) \right\} \\
S_4 &= \int_0^\beta d\tau \int d^2x \left[u_1 \left(\vec{m}_A^2 + \vec{m}_B^2 \right)^2 - u_I \left(\vec{m}_A \cdot \vec{m}_B \right)^2 - u_2 \left(\vec{m}_A^2 - \vec{m}_B^2 \right)^2 \right]
\end{aligned}
\tag{2.49}
$$

where u_1, u_2, u_I are all positive, and:

$$G_0^{-1}\left(\vec{q}, i\omega_n\right) = r\left(w\right) + \omega_n^2 + c\vec{q}^2 + \gamma|\omega| \tag{2.50}$$

with $r\left(w\right) = r_0 + wA_{\vec{Q}}$. We choose $r_0 < 0$ so that at $w = 0$ the system is at the AF phase. Critical point can be reached by tuning w at critical value w_c such that $r = r_0 + w_c A_{\vec{Q}} = 0$.

Because of the Landau damping term $\gamma|\omega|$, which comes from the particle-hole polarization of the high energy itinerant electrons, the dynamical exponent $z = 2$. Consequently, the system (2.49) is at the critical dimension $D_{\text{eff}} = D + z = 4$, and the Ising-nematic coupling $-u_I < 0$ is a marginally relevant operator. Therefore, there are two relevant operators, one is the magnetic mass term r and the other is the Ising-nematic coupling $-u_I$. From the RG perspective, it suggests that the magnetic and the Ising-nematic phase transitions should be either concurrent in a first-order manner, or split into two continuous transitions. Either effect is expected weak because of the marginal nature of the coupling $-u_I$, so that there must be a large parameter range in which the critical phenomenon can be observed. According to this RG argument, we have the schematic phase diagram in Fig. 2.14, which has been supported theoretically by the large-N calculation[10] and experimentally by the P for As doped $BaFe_2As_2$[89, 90, 91]. The quantum critical regime with strange metal behavior has also been observed in the P for As doped $BaFe_2As_2$[92], as shown in Fig. 2.15.

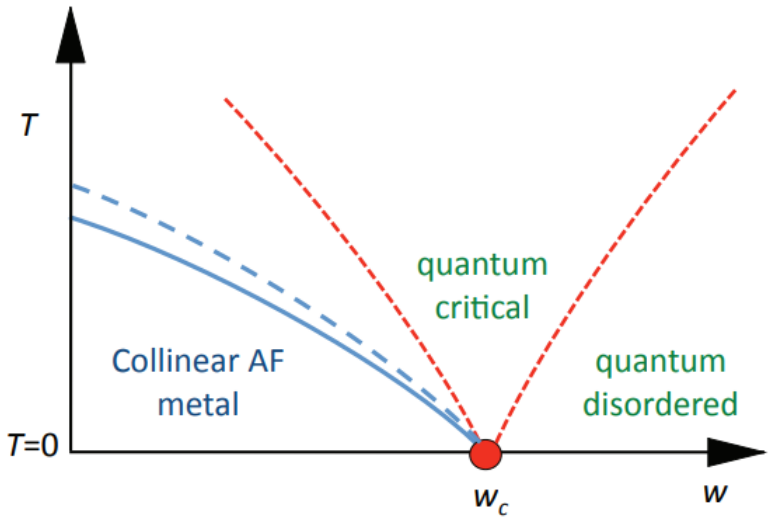

Figure 2.14 : Schematic phase diagram of iron-pnictides, where solid and dashed blure line denote antiferromagnetic and Ising-nematic phase transition, respectively. Adapted from Ref.[9].

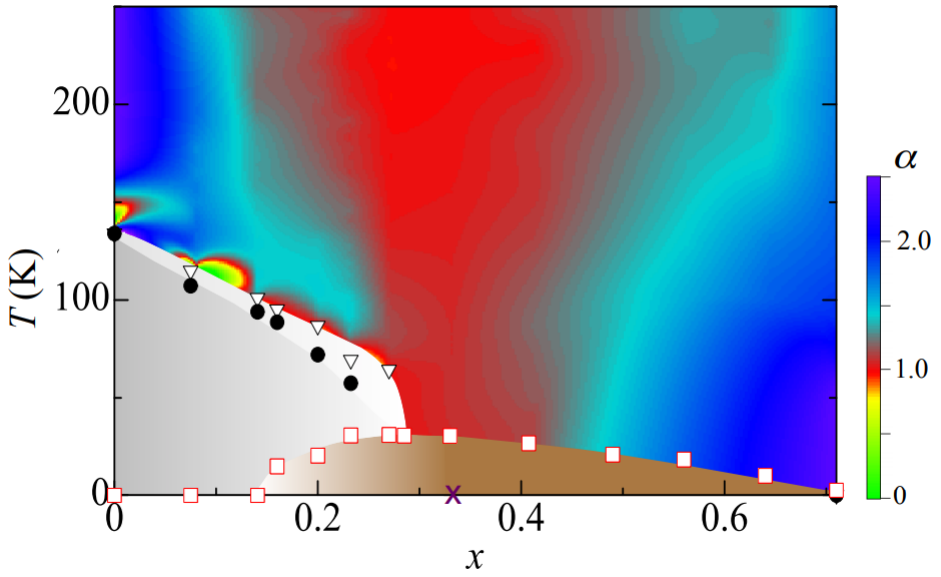

Figure 2.15 : Phase diagram for $BaFe_2(As_{1-x}P_x)_2$. The color shading represents the value of the resistivity exponent in the relation $\rho = \rho_0 + AT^{\alpha}$. The inverted triangles, black dots and squares denote the structural, magnetic (gray region) and superconducting (brown region) transitions, respectively. Adapted from Ref. [9].

Chapter 3

Skyrmion defects of antiferromagnet and competing singlet orders of a Kondo-Heisenberg model on honeycomb lattice

3.1 Introduction

Competing orders and quantum criticality are two generic features of the rich phase diagrams displayed by several strongly correlated materials, including heavy fermion systems [66, 77, 93, 3, 2]. Of particular significance are the antiferromagnetic phase and competing spin-singlet phases such as charge and bond density waves and unconventional pairings. Therefore, for a comprehensive understanding of the global phase diagrams of many strongly correlated materials, it is essential to gain insights into the relationship among different competing orders, which spontaneously break distinct global symmetries. Within the conventional theme of Landau theory of local order parameters, describing smooth fluctuations or collective modes, order parameters breaking distinct symmetries do not seem to bear any specific relationship. However, the nonperturbative topological defects of order parameters such as domain walls, vortices, skyrmions and hedgehogs can support competing orders as fluctuating objects and thereby contain information about apparently distinct ordered states[55, 56, 94, 31, 32, 95, 96, 97, 98, 99]. In addition, the interaction between fermions and topological defects can be important in strongly correlated electronic systems such as heavy fermion compounds, generically described by effective Kondo-

Heisenberg models. The strong competition among antiferromagnetism and Kondo singlet formation in addition to spin-singlet superconductivity are essential features of many heavy fermion compounds, and a global phase diagram has been theoretically proposed [2] which features the transitions between an antiferromagnetic order and a variety of spin-singlet paramagnetic phases. This global phase diagram has been studied in the Kondo-Heisenberg models using various microscopic methods [100], and has motivated experimental investigations in a number of heavy fermion materials[34, 101, 102, 103, 104]. However, it remains a theoretical challenge to concretely access the spin-singlet orders (e.g., the heavy fermi liquid phase due to static Kondo singlets) of the paramagnetic phases starting from the antiferromagnetically ordered side. In this work, we are interested in addressing the fluctuating spin-singlet orders supported by gapped skyrmion excitations inside an antiferromagnetically ordered phase of a Kondo-Heisenberg model. We are also interested in identifying the most dominant singlet orders which can be nucleated when the antiferromagnet order is destroyed by quantum fluctuations, causing the collapse of skyrmion excitation gap inside the paramagnetic phase.

The general problem of interaction between fermions and topological defects is often intractable. But valuable insights can be gained by studying specific toy models where fermionic degrees of freedom are modeled by Dirac fermions. In this regard, a Kondo-Heisenberg model defined on the honeycomb lattice plays a very instructive role, as the coupling between Dirac fermions and antiferromagnetic order parameter can be addressed employing diverse analytical and numerical methods. Some previous works have addressed the interaction between Dirac fermions and topologically nontrivial skyrmion configuration of antiferromagnetic order parameter, by employing perturbative gradient expansion scheme[31, 32]. Within such scheme the calculations

of triangle diagram for Goldstone-Wilczek current are controlled by the inverse of Dirac mass (caused by uniform amplitude of antiferromagnetic order) and rely upon adiabatic principle.

3.1.1 Competition between spin Peierls and antiferromagnetic orders

The simplest situation involves a doublet (two inequivalent valleys or nodes) of spinful Dirac fermions coupled to antiferromagnetic order that simultaneously breaks time reversal and spatial inversion symmetries. The corresponding low energy theory can be described by the effective action

$$S_1 = \int d^2x d\tau \bar{\psi}[\gamma_\mu \partial_\mu + g_\psi \mathbb{1} \otimes \boldsymbol{\eta} \cdot \mathbf{n}]\psi, \tag{3.1}$$

where ψ is a eight-component spinor (incorporating two sublattice, two nodal and two spin degrees of freedom), γ_μ are three mutually anticommuting 4×4 Hermitian matrices operating on sublattice and valley indices, $\mathbb{1}$ is 4×4 identity matrix that operates on sublattice and valley indices, and Pauli matrices $\boldsymbol{\eta}$ act on spin components. The coupling between fermion and the O(3) vector order parameter $\mathbf{n}$ is denoted by g_ψ. Inside the antiferromagnetically ordered phase Dirac fermions possess excitation or mass gap $2g_\psi\langle\bar{\psi}\mathbb{1} \otimes \boldsymbol{\eta} \cdot \mathbf{n}\psi\rangle$. The gradient expansion analysis (controlled by the mass gap) shows that a skyrmion acquires an induced chiral charge $Q_5 = \langle\bar{\psi}\gamma_0\gamma_5\psi\rangle = 2Q_{top}$, where Q_{top} is the topological invariant or Pontryagin index for skyrmion configuratio[105, 106, 107, 108, 109]. Within the continuum description, the chiral charge acts as the generator of translational symmetry (an emergent U(1) symmetry when higher gradient kinetic terms are ignored). Inside the antiferromagnetically ordered phase, the skyrmion number and consequently the chiral charge Q_5 act as conserved quantities, thus freely mixing two bilinears $\bar{\psi}\hat{M}\psi$ and $\bar{\psi}\hat{M}\gamma_5\psi$,

where $[\hat{M}, \gamma_5] = 0$, which cause hybridization between two inequivalent nodes. Consequently, skyrmion core supports translational symmetry breaking orders $\bar{\psi}\hat{M}\psi$ and $\bar{\psi}\hat{M}\gamma_5\psi$ as fluctuating quantities. The specific choice $\hat{M} = \mathbb{1}$ corresponds to spin Peierls order, while other choices for $\hat{M}$ represent charge and current density wave orders. All of these singlet orders mix two valleys, and naturally break chiral or translational symmetry [31, 32].

3.1.2 Competition between Kondo singlets, spin Peierls and antiferromagnetic orders

For the Kondo-Heisenberg model defined on the honeycomb lattice, we have to account for two species of eight-component fermions corresponding to conduction and f-electrons. Inside the antiferromagnetically ordered phase the low energy theory can be qualitatively understood in terms of the effective action

$$S_2 = \int d^2x d\tau \bar{\psi}[\gamma_\mu \partial_\mu + g_\psi \mathbb{1} \otimes \boldsymbol{\eta} \cdot \mathbf{n}]\psi + \int d^2x d\tau \bar{\chi}[\gamma_\mu \partial_\mu + g_\chi \mathbb{1} \otimes \boldsymbol{\eta} \cdot \mathbf{n}]\chi,$$

where ψ and χ capture two distinct eight-component Dirac fermions [32, 99]. Crucially, the antiferrormagnetic sign of Kondo coupling is described by the condition $g_\psi g_\chi < 0$ (same sign would represent Hund's coupling and describe spin-1 system). For simplicity all additional couplings between two species of fermions (residual quartic interactions) are being ignored. Both species of fermions give rise to induced chiral charges, while their sum vanishes. Interestingly, the difference between two types of induced chiral charge equals $4Q_{top}$, i.e., $Q_{5,+} = \langle \bar{\psi}\gamma_0\gamma_5\psi \rangle + \langle \bar{\chi}\gamma_0\gamma_5\chi \rangle = 0$ and $Q_{5,-} = \langle \bar{\psi}\gamma_0\gamma_5\psi \rangle - \langle \bar{\chi}\gamma_0\gamma_5\chi \rangle = 4Q_{top}$. It has been shown that the relative chiral charge $Q_{5,-}$ (hence the skyrmion number) causes free rotation among several translational symmetry preserving Kondo singlet operators (mixing ψ and χ at same valley)

in addition to conventional translational symmetry breaking density wave operators. Therefore gradient expansion scheme provided important insight that the skyrmion texture supports several competing Kondo singlet operators, spin Peierls (bond density) as well as charge and current density wave orders inside the antiferromagnetic insulating phase [32].

3.1.3 One dimensional Kondo-Heisenberg model

A similar issue of interaction between Dirac fermions and topological defects of antiferromagnetic order has also been emphasized in one spatial dimension [110, 111]. In one dimension the relevant topological defects are instantons or tunneling events for O(3) quantum nonlinear sigma model. However these instantons in two-dimensional Euclidean space, and static skyrmions of (2+1)-dimensional model have identical forms. By employing different field theoretic methods (direct gradient expansion and chiral anomaly), it has been found that the instanton number is directly related to the expectation value of bilinear $\bar{\psi}\gamma_5\psi$ (which represents translational symmetry breaking, Ising spin-Peierls order). In the presence of Kondo coupling, one finds the competition between Kondo singlet formation and spin-Peierls order[111]. This picture is also qualitatively supported by bosonization analysis.

3.1.4 Accomplishments of the present work

However, the gradient expansion scheme only employs scattered states of Dirac fermions, while completely ignoring the effects of low energy bound states. How do these non-perturbative eigenstates affect the predictions of gradient expansion? Which are the most dominant singlet orders which can be nucleated after the antiferromagnetic order is destroyed by quantum fluctuations, causing a collapse of skyrmion excitation

gap? In the present work we answer these important physical and technical questions. We first solve for the exact fermion eigenfunctions in the presence of topologically nontrivial skyrmion background to establish the induced chiral charge of skyrmion texture. Subsequently by employing these nonperturbative eigenstates, we evaluate the susceptibilities of different competing orders. Based on the susceptibilities, we demonstrate spin Peierls to be the most dominant translational symmetry breaking singlet order, which strongly competes against the static Kondo singlet formation. We also substantiate our results obtained in the continuum limit by calculations performed with lattice regularizations. Intriguingly, we find remarkable agreement between the analysis of this work and the predictions of perturbative field theory[32] and more recent nonperturbative analysis of hedgehog-fermion interactions inside the paramagnetic phase[99].

Since the two dimensional skyrmion texture describes the instanton or tunneling event of nonlinear sigma model in one spatial dimension, our methodology can be directly applied to the one dimensional problem (1+1-dimensional space-time) for computing the fermion determinant in the presence of topologically nontrivial dynamic background (it is equivalent to solving a fictitious two dimensional Hamiltonian defined in Euclidean space). Therefore, we can also extract the dynamic information regarding destruction of algebraic spin liquid in favor of competing Kondo singlet and spin Peierls phases for one dimensional Kondo-Heisenberg chain. Similarly, our methodology can be applied for many two and also three dimensional systems, supporting competition between spin-triplet and spin-singlet orders.

3.2 Kondo lattice model on honeycomb lattice

The Hamiltonian for Kondo-Heisenberg model on a honeycomb lattice is given by

$$H = \sum_{\boldsymbol{r}_i \in A} \sum_{j=1}^{3} \Big[-t_c \, c^{\dagger}_{A,\alpha}(\boldsymbol{r}_i) \, c_{B,\alpha}(\boldsymbol{r}_i + \boldsymbol{\delta}_j) + h.c + J_H \, \boldsymbol{S}_A(\boldsymbol{r}_i) \cdot \boldsymbol{S}_B(\boldsymbol{r}_i + \boldsymbol{\delta}_j) + J_K \, c^{\dagger}_{A,\alpha}(\boldsymbol{r}_i) \frac{\boldsymbol{\eta}_{\alpha\beta}}{2} c_{A,\beta}(\boldsymbol{r}_i) \cdot \boldsymbol{S}_A(\boldsymbol{r}_i) + \frac{J_K}{3} \, c^{\dagger}_{B,\alpha}(\boldsymbol{r}_i + \boldsymbol{\delta}_j) \frac{\boldsymbol{\eta}_{\alpha\beta}}{2} c_{B,\beta}(\boldsymbol{r}_i + \boldsymbol{\delta}_j) \cdot \boldsymbol{S}_B(\boldsymbol{r}_i + \boldsymbol{\delta}_j) \Big], \tag{3.2}$$

where $c^{\dagger}_{A/B,\alpha/\beta}$ is the conduction electron creation operator, and A, B denote two interpenetrating triangular sublattices, and Pauli matrices $\boldsymbol{\eta}$ operate on spin indices α and β, and $\boldsymbol{\delta}_j$ are three coordination vectors connecting two sublattices, as shown in Fig. 3.1. The explicit form of these vectors are $\boldsymbol{\delta}_1 = \left(-\frac{a}{2}, \frac{\sqrt{3}a}{2}\right)$, $\boldsymbol{\delta}_2 = (a, 0)$ and $\boldsymbol{\delta}_3 = \left(-\frac{a}{2}, -\frac{\sqrt{3}a}{2}\right)$, where a is the lattice spacing. The local moments on sublattice A and B are represented by $\boldsymbol{S}_A(\boldsymbol{r}_i)$ and $\boldsymbol{S}_B(\boldsymbol{r}_i + \boldsymbol{\delta}_j)$, respectively. The RKKY coupling between local moment is modeled by nearest neighbor Heisenberg interaction with strength J_H, and J_K is the Kondo coupling between conduction electron and local moment. We will consider both J_H and J_K to be antiferromagnetic, i.e., $J_H > 0$ and $J_K > 0$.

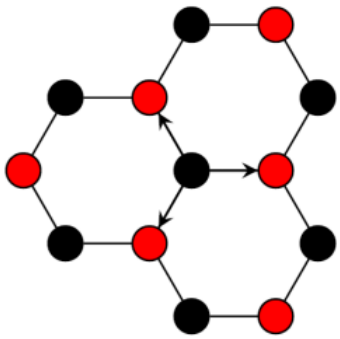

Figure 3.1 : The structure of honeycomb lattice, where the red and the black circles, respectively, denote two interpenetrating triangular sublattices A and B. Coordinate vectors $\boldsymbol{\delta}_i$ are shown as solid line with arrows.

After linearizing the dispersion relation for fermions around two inequivalent nodal points of the hexagonal Brillouin zone (located at $\mathbf{K}_{\pm}$) and analytically continuing real time to imaginary time by setting $\tau = it$, the low energy effective physics of free conduction electron can be described by the imaginary time action:

$$S_0 = \int dx^2 d\tau \overline{\psi}_\alpha \left(\gamma_0 \otimes \eta_0 \partial_t + v_\psi \gamma_j \otimes \eta_0 \partial_j\right) \psi_\alpha, \tag{3.3}$$

where $v_\psi = \frac{\sqrt{3} t_c a}{3}$ is the Fermi velocity, spinor $\psi_\alpha^T = (c_{+,A,\alpha}, c_{+,B,\alpha}, c_{-,B,\alpha}, c_{-,A,\alpha})$, $\overline{\psi}_\alpha = \psi_\alpha \gamma_0$, $\pm$ is index for two valleys $K_\pm$, and α is spin index. The gamma matrices are defined as:

$$\begin{aligned} \gamma_0 = \tau_1 \otimes \sigma_0 = \begin{pmatrix} 0 & \sigma_0 \\ \sigma_0 & 0 \end{pmatrix}, \gamma_j = i\tau_2 \otimes \sigma_j = \begin{pmatrix} 0 & \sigma_j \\ -\sigma_j & 0 \end{pmatrix}, \\ \gamma_5 = \tau_3 \otimes \sigma_0 = \begin{pmatrix} \sigma_0 & 0 \\ 0 & -\sigma_0 \end{pmatrix} \end{aligned} \tag{3.4}$$

where the Pauli matrices $\boldsymbol{\sigma}$, $\boldsymbol{\tau}$ respectively operate on the sublattice and valley indices.

Inside the antiferromagnetically ordered phase, the low energy physics of local moments can be described by QNLσM [45, 46]:

$$S_n = \frac{1}{2cg} \int d^2 x d\tau \left[c^2 \left(\partial_x \boldsymbol{n}\right)^2 + \left(\partial_\tau \boldsymbol{n}\right)^2\right] + i S_B \left[\boldsymbol{n}\right] \tag{3.5}$$

The coupling constant g has the dimension of length, and the antiferromagnetically ordered phase exists for g smaller than a critical strength g_c[50]. The last term $S_B\left[\boldsymbol{n}\right]$ corresponds to Berry phase, which vanishes inside the ordered phase. The Berry phase can be finite inside the paramagnetic phase, but it does not possess a simple continuum limit in (2+1) dimensions[52, 54].

Now we incorporate the Kondo coupling, which captures the scattering between conduction electron spinor ψ and the QNLσM field $\boldsymbol{n}$ representing the local moment:

$$S_K = g_K \int d^2 x d\tau \overline{\psi}_\alpha \gamma_3 \boldsymbol{n} \cdot \boldsymbol{\eta}_{\alpha\beta} \psi_\beta \tag{3.6}$$

Therefore, the low energy theory of antiferromagnetic phase for the Kondo-Heisenberg model can be described by:

$$S = S_0 + S_n + S_K \tag{3.7}$$

The lack of continuum representation for Berry's phase in (2+1)-dimensions makes it hard to analyze its consequence inside the paramagnetic phase based on the coarse grained representation. However, this can be circumvented by introducing auxiliary f-fermions for describing the local moments [32]. We assume that the auxiliary f-fermions only hop to the nearest neighbor sites like the conduction fermions, with a hopping strength t_f. At low energies, these f-fermions can also be described by the Dirac equation with a new spinor $\chi_\alpha^T = (f_{+,A,\alpha}, f_{+,B,\alpha}, f_{-,B,\alpha}, f_{-,A,\alpha})$. Thus, the resulting low energy effective action for f-fermion inside AF phase is:

$$S_f = \int dx^2 d\tau \overline{\chi}_\alpha \left[\gamma_0 \otimes \eta_0 \partial_t + v_\chi \gamma_j \otimes \eta_0 \partial_j + g_\chi \gamma_3 \boldsymbol{n} \cdot \boldsymbol{\eta}\right]_{\alpha\beta} \chi_\beta \tag{3.8}$$

where $v_\chi = \frac{\sqrt{3} t_f a}{2}$. In fact, after integrating out the f-fermion degrees of freedom, this action will return to the same form of QNLσM of Eq. (3.5) [112, 113, 106]. We again remind the reader that the Berry phase vanishes inside the antiferromagnetically ordered phase and only becomes important for addressing the nature of paramagnetic phase. The Hamiltonian operator from Eq. (3.6) involving only f-electrons would be:

$$H_f = \tau_3 \left[-i v_\chi \left(\sigma_1 \partial_1 + \sigma_2 \partial_2\right) + g_\chi \boldsymbol{n} \cdot \boldsymbol{\eta} \sigma_3\right]. \tag{3.9}$$

Usually the introduction of auxiliary fermion description requires the introduction of Lagrange multiplier or constraint gauge fields. Since in this work we would be dealing with confined phases of matter such as antiferromagnet, spin Peierls or Kondo singlets, the constraint gauge field does not affect any of our conclusions regarding the competing order. For this reason we follow Ref.[114] and use an alternative method

that avoids introduction of any constraint gauge fields. Within this method one considers actual f electrons in the presence of sufficiently strong Hubbard interaction, which gives rise to an antiferromagnetic phase. The relevant steps are described in the Appendix A.1.

Therefore, the Hamiltonian operator for the combined problem described by $S = S_0 + S_f + S_K$ is given by

$$H_\Psi = \tau_3 \left[-iv_+ \left(\sigma_1 \partial_1 + \sigma_2 \partial_2 \right) - iv_- \left(\sigma_1 \partial_1 + \sigma_2 \partial_2 \right) \rho_3 + g_+ \boldsymbol{n} \cdot \boldsymbol{\eta} \sigma_3 + g_- \boldsymbol{n} \cdot \boldsymbol{\eta} \sigma_3 \rho_3 \right], \tag{3.10}$$

which operates on the spinor $\Psi = (\psi, \chi) = (c_{A\alpha+}, c_{B\alpha+}, c_{B\alpha-}, c_{A\alpha-}, f_{A\alpha+}, f_{B\alpha+}, f_{B\alpha-}, f_{A\alpha-})$ where $v_\pm = \frac{v_c \pm v_f}{2}$ and $g_\pm = \frac{g_K \pm g_\chi}{2}$, and new Pauli matrices ρ_i act on the flavor index representing conduction and f-electrons, (ψ, χ). Inside AF phase, we expect that the staggered magnetic moments of conduction electron ψ and f-electron χ anti-align to each other. Therefore, we have $g_K g_\chi < 0$ [32] .

3.3 Skyrmion, induced chiral charge and competing orders: perturbative argument

The static nonsingular topological defect of QNLσM in $2+1$ dimensions is called skyrmion, which satisfies the boundary condition $\boldsymbol{n}\left(r \to \infty\right) = \boldsymbol{n}^0$, where $r = \sqrt{x^2 + y^2}$ and $\boldsymbol{n}^0$ is a constant unit vector. Therefore, the two-dimensional space is compactified onto a two sphere S^2 and the skyrmion configurations are defined by an integer topological charge also known as skyrmion number, since the homotopy group $\Pi_2\left(S^2\right) = Z$. The skyrmion with topological charge $Q_{top} \in Z$ can have arbitrary profile function, provided it satisfies the boundary condition and the requirement that $\frac{1}{4\pi} \int d^2x \boldsymbol{n} \cdot \partial_1 \boldsymbol{n} \times \partial_2 \boldsymbol{n} = Q_{top}$. Fig. 3.2 illustrates a real space profile

for single skyrmion with $Q_{top} = 1$.

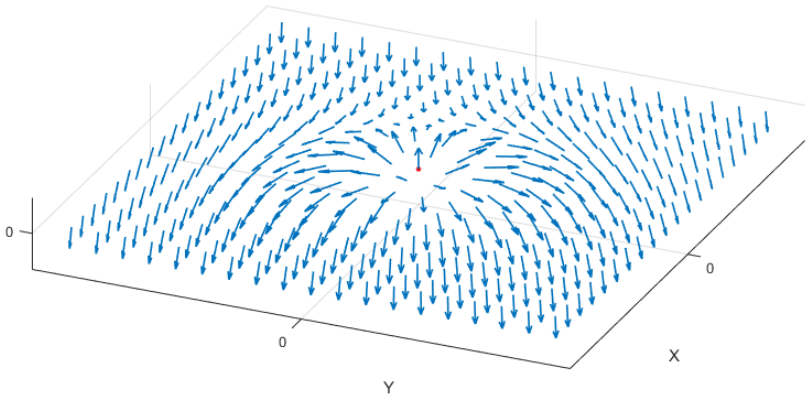

Figure 3.2 : Illustration of single skyrmion. The red dot denotes the origin of skyrmion core, and blue arrow is the direction of staggered magnetization or antiferromagnetic order parameter $\boldsymbol{n}$.

It is well known, when Dirac fermions are coupled to QNLσM, the skyrmion textures will acquire induced fermion number [108, 109, 115, 116, 106]. For Hamiltonian of Eq. (3.9), due to the overall matrix τ_3 (appearing odd number of times) operating on two inequivalent valleys, the total induced fermionic charge vanishes. But the chiral charge, defined as the difference of fermion densities at two valleys, will be proportional to the topological charge of skyrmion:

$$\begin{aligned} Q_{\pm} &\equiv \int d^2x \langle :f_{\pm}^{\dagger} f_{\pm}: \rangle = \pm \,\mathrm{sign}\,(g_{\chi})\, Q_{top}, \\ Q_5 &\equiv \int d^2x \langle :\chi^{\dagger}\tau_3\chi: \rangle = \int d^2x \left(\langle :f_{+}^{\dagger} f_{+}: \rangle - \langle :f_{-}^{\dagger} f_{-}: \rangle \right), \\ &= 2\,\mathrm{sign}\,(g_{\chi})\, Q_{top}, \end{aligned} \tag{3.11}$$

$Q_{\pm}$ are the charges for $\pm$ valleys, and :: denotes normal ordering operation. These relations can be proven by gradient expansion method [106], and the detailed derivation is provided in Appendix A.2. We can also verify this result numerically by solving

for the spectral flow during adiabatic formation of skyrmion, as shown in Fig. 3.3. We can simulate the formation of single (anti)skyrmion without loss of generality by assuming

$$\boldsymbol{n}\left(\vec{r},t\right)=\left(\sin tf\left(r\right)\cos\theta,\sin tf\left(r\right)\sin\theta,\cos tf\left(r\right)\right), \tag{3.12}$$

where $f\left(r\right)=\pi e^{-\frac{r}{2}}$. One can easily verify that $Q_{top}=0$ at $t=0$ and $Q_{top}=-1$ at $t=1$, and the definition of (anti)skyrmion does not depend on the precise form of profile function. For + valley, as shown in Fig. 3.3, we find there is precisely one state that crosses zero energy (flowing out of negative energy states or filled Dirac sea) during the formation of skyrmion. Therefore, the induced charge is -1, just as Eq. (3.11) suggests*. The relation among the induced fermionic chiral charge of the system, the spectrum flow, and the topological charge of skyrmion, is a consequence of index theorem [117, 118].

Since $g_K g_\chi<0$, the induced chiral charges for conduction and f-electrons have opposite signs [electron $Q_{5,\psi}=2\,\mathrm{sign}\left(g_K\right)Q_{top}$ and f-electron $Q_{5,\chi}=2\,\mathrm{sign}\left(g_\chi\right)Q_{top}$]. This means if one state for conduction fermion sinks into the Dirac sea, there will be a state for f-electrons which will emerge out of the Dirac sea. Therefore, the net chiral charge of two species vanishes. Nonetheless, the difference between two chiral charges is quantized:

$$Q_{-,\Psi}\equiv\int d^2x\langle:\Psi^\dagger\rho_3\tau_3\Psi:\rangle=Q_{5,\psi}-Q_{5,\chi}=4\,\mathrm{sign}\left(g_K\right)Q_{top} \tag{3.13}$$

*Note that in the intermediate stage of the skyrmion formation (3.12) $0<t<1$, there is a discontinuity of the skyrmion profile at the origin. The derivate near the orign is huge and thus the gradient expansion and Eq. (3.11) might no longer be valid. Nonetheless, at $t=0,1$, the discontinuity is absent and, correspondingly, the gradient expansion and the Eq. (3.11) are well-defined.

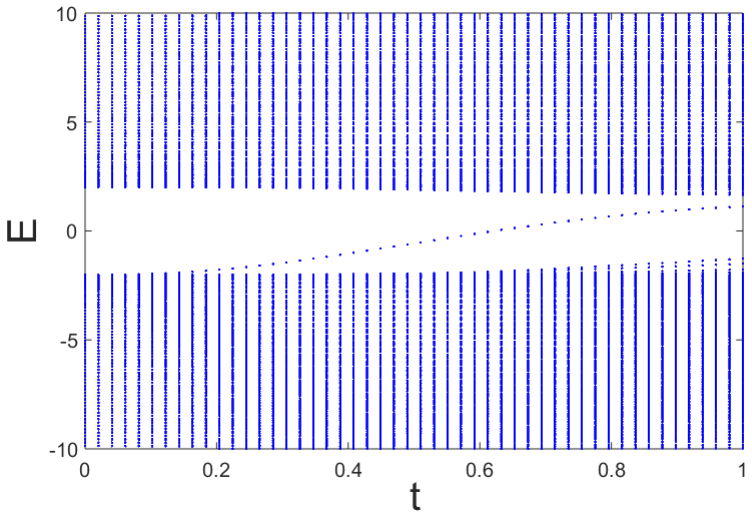

Figure 3.3 : The spectral flow for + valley during the adiabatic formation of skyrmion. Here we choose coupling constant $g_\chi = 2$

Inside the AF ordered phase, the tunneling events described by singular hedgehog and antihedgehog configurations (space-time singularities) are linearly confined, leading to the conservation of skyrmion number. When the AF order is gradually suppressed by quantum fluctuations, the spin stiffness of the sigma model and the skyrmion energy cost decrease. On the paramagnetic side, the skyrmions excitation energy vanishes, and all topologically distinct skyrmion configurations become energetically degenerate. Hence, the tunneling events between different skyrmion configurations become important for determining how ground state degeneracy is lifted. Since Q_5 and $Q_{-,\Psi}$ are proportional to the topological charge Q_{top} [as in Eq. (3.11) and Eq. (3.13)], Q_5 and $Q_{-,\Psi}$ would also be changed via tunneling events. Thus Q_5 and $Q_{-,\Psi}$ would act as fast variables inside paramagnetic phase, and their conjugate operators will serve as the appropriate slow variables or competing order parameters [31, 32].

Competing order	Matrix form $\hat{M}$	anticommute with H_Ψ?
Valence bond solid	τ_1, τ_2	Yes
Charge density wave	$\tau_1\sigma_1, \tau_1\sigma_2$	No
Current density wave	$\tau_1\sigma_3$	No

Table 3.1 : Competing orders for one species of fermion coupled to antiferromagnetic order parameter.

Based on this argument, for one species of Dirac fermions [e.g., for Hamiltonian H_f of Eq. (3.9)], the corresponding spin-singlet competing orders in the particle-hole channel are found to be

$$Q_M = \chi^\dagger \hat{M} e^{i\phi\tau_3}\chi. \tag{3.14}$$

Here $\hat{M}$ is a 4×4 matrix operating on sublattice and valley indices, and there are five distinct order parameters O_M, which are conjugate to chiral charge operator $\hat{Q}_5 = \chi^\dagger\tau_3\chi$, i.e., $\left[\hat{Q}_5, O_M\right] \propto \chi^\dagger \hat{M} e^{i\left(\frac{\pi}{2}+\phi\right)\tau_3}\chi$, as indicated in TABLE 3.1. The first two correspond to components of the valence bond solid(VBS), which is also called Kekule bond density wave order or spin Peierls order breaking the translation symmetry unlike the usual AKLT state resulting from spin-1 model, and the final three correspond to different kinds of charge or current density wave orders [31, 32]. However, only the components of VBS order anticommute with the whole Hamiltonian operator H_f of Eq. (3.9), thus maximizing the energy gap inside the skyrmion core. Therefore, from a weak coupling perspective, the VBS order should be the most dominant competing order of antiferromagnetism.

For the Kondo-Heisenberg model with two species of eight component Dirac fermions [see Eq. (3.10)], $Q_{-,\Psi}$ is proportional to the skyrmion number. Therefore, the conjugate operators of $Q_{-,\Psi}$ would serve as competing orders in the presence of

Competing order	Matrix form $\hat{M}$	anticommute with H_Ψ?
Valence bond solid	τ_1, τ_2	Yes
Charge density wave	$\tau_1\sigma_1, \tau_1\sigma_2$	No
Current density wave	$\tau_1\sigma_3$	No
Kondo singlet	$\rho_1, \rho_2, \tau_3\rho_1, \tau_3\rho_2$	Yes iff $v_+ = 0$ and $g_+ = 0$
Kondo singlet	$\sigma_3\rho_1, \sigma_3\rho_2, \tau_3\sigma_3\rho_1, \tau_3\sigma_3\rho_2$	Yes iff $v_- = 0$ and $g_+ = 0$

Table 3.2 : Competing spin-singlet orders in the presence of Kondo coupling

antiferromagnetic Kondo coupling, and they are listed in TABLE 3.2. Besides VBS, charge and current density orders already found in TABLE 3.1, the presence of ρ_3 in $\hat{Q}_{-,\Psi}$ gives rise to additional competing orders involving ρ_1 or ρ_2, corresponding to hybridization of two species or Kondo singlet formation [32]. While the VBS orders (with τ_1, τ_2) always anticommute with the combined Hamiltonian, the Kondo singlet operators do not generically anticommute with the combined Hamiltonian. Hence from the weak coupling perspective, they may not be dominant competing orders inside the skyrmion core. Only for some special choice of parameters, some Kondo singlet operators can anticommute with the effective Hamiltonian. Therefore, the gradient-expansion based results may not always predict the correct competing orders. In the following section, we circumvent this shortcoming of gradient-expansion scheme, by evaluating the exact eigenstates of Dirac Hamiltonian and subsequently computing the susceptibilities of different competing orders.

3.4 Beyond pertubative argument

The eigenstates of Dirac fermions in the presence of skyrmion configurations of O(3) nonlinear sigma model have been previously discussed in Ref. [116]. The main goal was to establish the induced fermion number due to spectral flow. But, the physical role of fermion doublers (present for any lattice model) and competing orders has not been addressed. By contrast, we would deal with fermion doublers arising from the underlying lattice model, and focus on identifying dominant competing orders residing in the skyrmion core. Therefore, we would compute susceptibilities of competing spin singlet order parameters, by using the exact eigenstates of Dirac fermions. This is a new development for the problem of interaction between Dirac fermions and O(3) skyrmion configurations.

3.4.1 Without Kondo coupling

To calculate the local susceptibility of predicted competing orders in TABLE 3.1, we solve

$$\left(H_f + \Delta\hat{M}\right)\chi = E\chi \tag{3.15}$$

on a finite disk of radius R by performing exact diagonalization. We denote the Hamiltonian Eq. (3.9) with or without single skyrmion as $H_{f,S}$ and $H_{f,0}$, respectively. For single skyrmion, we choose the profile function of skyrmion $\boldsymbol{n}$ as

$$\boldsymbol{n} = (\sin f(r)\cos\theta, \sin f(r)\sin\theta, \cos f(r)) \tag{3.16}$$

where $f(r) = \pi e^{-\frac{r}{\lambda}}$ and λ is the length scale for skyrmion. One can easily verify that in this case we have $\frac{1}{4\pi}\int d^2x \boldsymbol{n}\cdot\partial_1\boldsymbol{n}\times\partial_2\boldsymbol{n} = -1$.

The eigenstates of $H_{f,0}$ constitute a suitable basis for performing exact diagonal-

ization. We choose the background field $\boldsymbol{n} = (0, 0, 1)$, such that:

$$H_{f,0} = \tau_3 \left[v_\chi \left(\sigma_1 k_1 + \sigma_2 k_2 \right) + g_\chi \eta_3 \sigma_3 \right]. \tag{3.17}$$

Since Hamiltonian $H_{f,0}$ commutes with grand spin operator $\hat{M}_3 = -i\partial_\theta + \frac{\sigma_3}{2} + \frac{\eta_3}{2}$, $H_{f,0}$ and $\hat{M}_3$ can be simultaneoulsy diagonalized. The solutions for $H_{f,0}\chi = E\chi$ with fixed grand spin m consist of the following linearly independent states:

$$\begin{aligned}
\chi_{+,m,j,n,\eta=1}(r,\theta) &= e^{im\theta} \begin{bmatrix} C_{\eta=1} \frac{v_\chi k_{m,j}}{nE_{m,j} - g_\chi} J_{m-1}\left(k_{m,j} r\right) e^{-i\theta} \\ i C_{\eta=1} J_m\left(k_{m,j} r\right) \\ 0_{6\times 1} \end{bmatrix} \\
\chi_{+,m,j,n,\eta=-1}(r,\theta) &= e^{im\theta} \begin{bmatrix} 0_{2\times 1} \\ C_{\eta=-1} \frac{v_\chi k_{m,j}}{nE_{m,j} + g_\chi} J_m\left(k_{m,j} r\right) \\ i C_{\eta=-1} J_{m+1}\left(k_{m,j} r\right) e^{+i\theta} \\ 0_{4\times 1} \end{bmatrix} \\
\chi_{-,m,j,n,\eta=1}(r,\theta) &= e^{im\theta} \begin{bmatrix} 0_{4\times 1} \\ C_{\eta=1} \frac{v_\chi k_{m,j}}{nE_{m,j} - g_\chi} J_{m-1}\left(k_{m,j} r\right) e^{-i\theta} \\ i C_{\eta=1} J_m\left(k_{m,j} r\right) \\ 0_{2\times 1} \end{bmatrix} \\
\chi_{-,m,j,n,\eta=-1}(r,\theta) &= e^{im\theta} \begin{bmatrix} 0_{6\times 1} \\ C_{\eta=-1} \frac{v_\chi k_{m,j}}{nE_{m,j} + g_\chi} J_m\left(k_{m,j} r\right) \\ i C_{\eta=-1} J_{m+1}\left(k_{m,j} r\right) e^{+i\theta} \end{bmatrix}
\end{aligned} \tag{3.18}$$

where the fist index $\pm$ means the $\pm$ valley, index $n = \pm 1$ denotes the solution with energy $\pm E_{m,j}$, and η is the spin index. We have chosen the boundary condition $J_m\left(k_{m,j} R\right) = 0$, with index j denoting the j-th zero of Bessel function $J_m\left(r\right)$, so that the momentum $k_{m,j}$ and energy $E_{m,j} = \sqrt{v_\chi^2 k_{m,j}^2 + g_\chi^2}$ are quantized. The coefficient

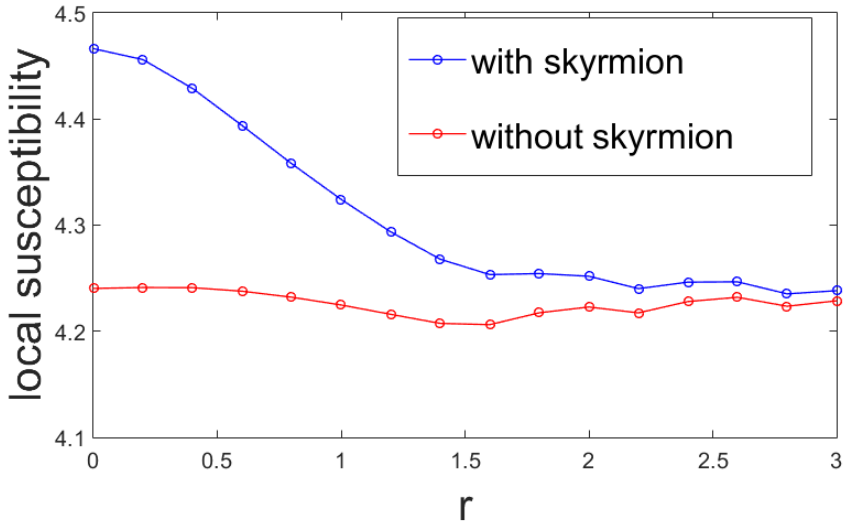

Figure 3.4 : The local susceptibility of VBS order $\hat{M} = \tau_1, \tau_2$ versus radial distance. The blue line and red line corresponds to the presence and the absence of skyrmion on origin, respectively. Once the skyrmion is present, the susceptibility of VBS order will gain obvious enhancement near the core of skyrmion defect.

C_η is determined by the normalization condition $\|\chi_{\pm,m,j,n,\eta}\|^2 \equiv \int d^2x \langle \chi_{\pm,m,j,n,\eta} | \chi_{\pm,m,j,n,\eta} \rangle = 1$.

We then solve the equation Eq. (3.15) by diagonalizing the matrix with elements $\int d^2x \langle \chi_{\pm,m,j,n,\eta} | H_f + \Delta \hat{M} | \chi_{\pm,m',j',n',\eta} \rangle$. Besides the real space cut-off (i.e, the radius of disk R), we also impose a large momentum cut-off Λ, and the large grand spin cut-off $\overline{M}$. We choose our basis set spanning from grand spin $-\overline{M}$ to $\overline{M}$. For $\hat{M} = \tau_1, \tau_2, \tau_1\sigma_3$, the Hamiltonian $H_f + \Delta\hat{M}$ commutes with the grand spin $\hat{M}_3$. Therefore, we can diagonalize the matrix in diagonal block with fixed value of grand spin m. While for $\hat{M} = \tau_1\sigma_1, \tau_1\sigma_2$ (which do not commute with $\hat{M}_3$), we have block off-diagonal elements and need to diagonalize the whole matrix at once.

After finding the solutions for Eq. (3.15), we compute the local susceptibility for

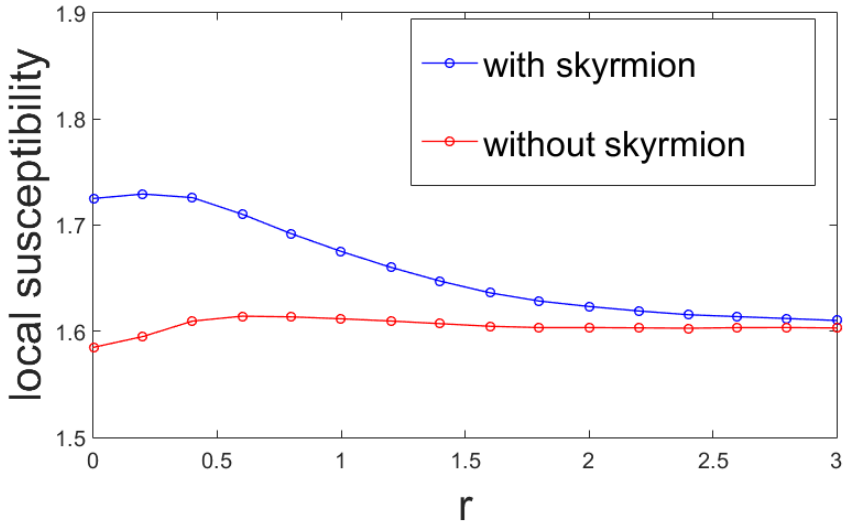

Figure 3.5 : The local susceptibility of charge density wave order $\hat{M} = \tau_1\sigma_1, \tau_1\sigma_2$ versus radial distance. Now the presence of skyrmion can still enhance the susceptibility, but the amount is smaller than VBS order.

each candidate competing order by using

$$\chi_M(r) = \lim_{\Delta \to 0} \frac{|\langle \chi^\dagger \hat{M} \chi \rangle|}{\Delta}. \tag{3.19}$$

The local susceptibility diverges with momentum cut-off Λ in two dimensions, but once we choose a finite momentum cut-off Λ, it converges with radius of disk R and the maximum of grand spin $\overline{M}$. In this paper, we choose $R = 8$, $\Lambda = 8$, $\overline{M} = 30$, the length scale of skyrmion $\lambda = 2$, and the coupling constant $g_\chi = 2$.

We have found that the local susceptibilities for VBS orders $\hat{M} = \tau_1$ or τ_2 gain expected enhancement near the core of skyrmion, as shown in Fig. 3.4 [†]. On the other hand, for other candidate competing orders like charge density wave (with $\tau_1\sigma_1$ and $\tau_1\sigma_2$), the enhancement is less prominent, as shown in Fig. 3.5. Moreover, for current density wave $\tau_1\sigma_3$, the presence of skyrmion even suppresses the susceptibility, like Fig. 3.6. The suppression of the susceptibility for current density wave $\tau_1\sigma_3$ demonstrates that the pertubative arguments of gradient-expansion scheme are not always sufficient.

[†]Actually, local susceptibility of τ_1 and τ_2 are exactly the same, since τ_1 and τ_2 can be transformed to each other by transforming the basis and the Hamiltonian Eq. (3.15) is invariant under such basis transformation. The same conclusion holds for the charge density wave orders $\tau_1\sigma_1$ and $\tau_1\sigma_2$, and different Kondo singlet orders in next section.

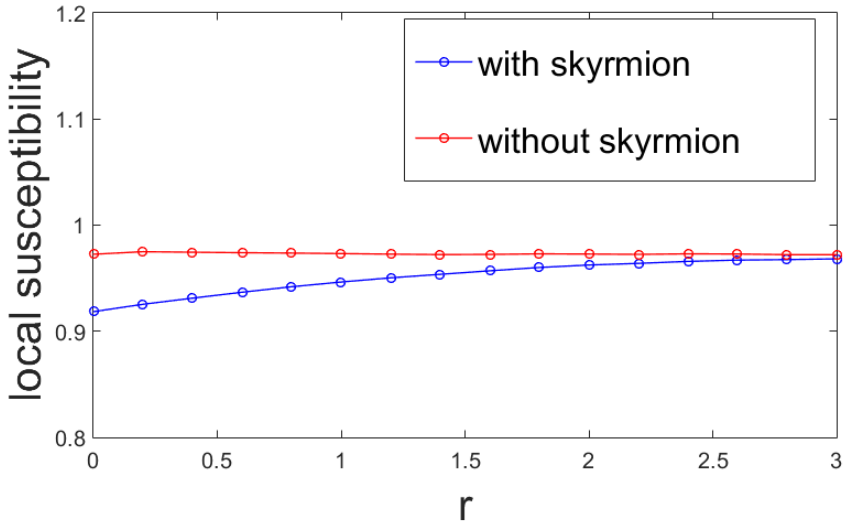

Figure 3.6 : The local susceptibility of current density wave order $\hat{M} = \tau_1\sigma_3$ versus radial distance. Instead of enhancement, the presence of skyrmion now suppresses the susceptibility of $\hat{M} = \tau_1\sigma_3$ near the core of skyrmion.

3.4.2 With Kondo coupling

In the presence of Kondo coupling, we have to account two types of fermion fields ψ and χ, and the pertubative argument predicts that the VBS and Kondo singlet orders are important competing orders of antiferromagnetism [see TABLE 3.2]. We want to establish the validity of this prediction by using exact eigenstates of Dirac Hamiltonian. This is particularly important, since Kondo singlet operators do not generically anticommute with the Hamiltonian, and within the weak coupling picture fully anticommuting VBS would seem to be the dominant competing order. Whether the Kondo singlet orders can be favored over fully anticommuting VBS over a wide range of microscopic parameter regime is not clear from the weak coupling arguments. By contrast, our physical intuition suggests that the Kondo singlets should be stabilized over a finite parameter region [2]. Here we address this issue by solving the eigenstates of

$$\left(H_{\Psi} + \Delta \hat{M}\right) \Psi = E\Psi, \tag{3.20}$$

for each $\hat{M}$ identified in TABLE 3.2, and then computing the local susceptibility by employing

$$\chi_M(r) = \lim_{\Delta \to 0} \frac{|\langle \Psi^{\dagger} \hat{M} \Psi \rangle|}{\Delta}. \tag{3.21}$$

For diagonalizing this Hamiltonian we use the basis set: $\Psi_{\pm,m,j,n,\eta} = (\psi_{\pm,m,j,n,\eta}, \chi_{\pm,m,j,n,\eta})$, where $\chi_{\pm,m,j,n,\eta}$'s have been already defined in Eq. (3.18) and $\psi_{\pm,m,j,n,\eta}$'s are defined as:

$$
\begin{aligned}
\psi_{+,m,j,n,\eta=1}(r,\theta) &= e^{im\theta}\begin{bmatrix} D_{\eta=1}\frac{v_\psi k_{m,j}}{nE'_{m,j}-g_K}J_{m-1}\left(k_{m,j}r\right)e^{-i\theta} \\ iD_{\eta=1}J_m\left(k_{m,j}r\right) \\ 0_{6\times1}\end{bmatrix} \\
\psi_{+,m,j,n,\eta=-1}(r,\theta) &= e^{im\theta}\begin{bmatrix} 0_{2\times1} \\ D_{\eta=-1}\frac{v_\psi k_{m,j}}{nE'_{m,j}+g_K}J_m\left(k_{m,j}r\right) \\ iD_{\eta=-1}J_{m+1}\left(k_{m,j}r\right)e^{+i\theta} \\ 0_{4\times1}\end{bmatrix} \\
\psi_{-,m,j,n,\eta=1}(r,\theta) &= e^{im\theta}\begin{bmatrix} 0_{4\times1} \\ D_{\eta=1}\frac{v_\psi k_{m,j}}{nE'_{m,j}-g_K}J_{m-1}\left(k_{m,j}r\right)e^{-i\theta} \\ iD_{\eta=1}J_m\left(k_{m,j}r\right) \\ 0_{2\times1}\end{bmatrix} \\
\psi_{-,m,j,n,\eta=-1}(r,\theta) &= e^{im\theta}\begin{bmatrix} 0_{6\times1} \\ D_{\eta=-1}\frac{v_\psi k_{m,j}}{nE'_{m,j}+g_K}J_m\left(k_{m,j}r\right) \\ iD_{\eta=-1}J_{m+1}\left(k_{m,j}r\right)e^{+i\theta}\end{bmatrix}.
\end{aligned}
\tag{3.22}
$$

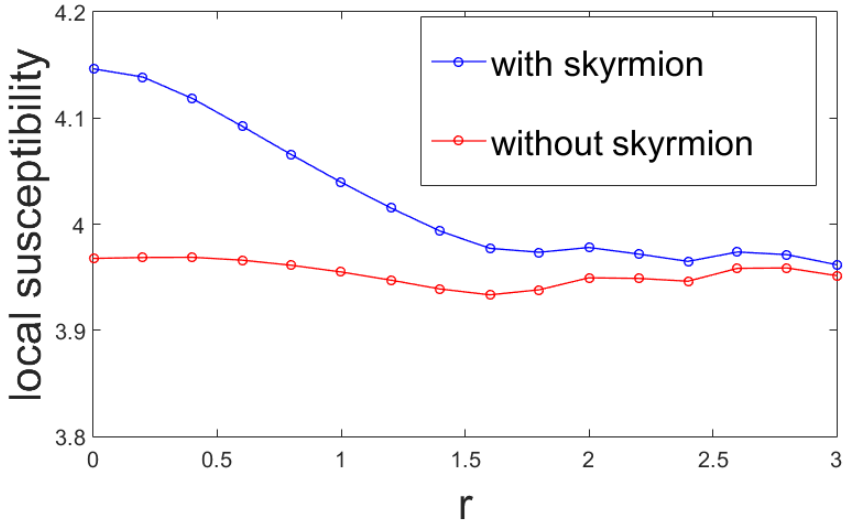

Figure 3.7 : The local susceptibility of Kondo singlet orders $\hat{M} = \rho_1, \rho_2, \tau_3\rho_1, \tau_3\rho_2$ ($\hat{M} = \sigma_3\rho_1, \sigma_3\rho_2, \sigma_3\tau_3\rho_1, \sigma_3\tau_3\rho_2$) with $v_\psi = 1$, $v_\chi = -1$, $g_\psi = 2$, and $g_\chi = -3$ ($v_\psi = 1$, $v_\chi = 1$, $g_\psi = 2$, and $g_\chi = -3$). The enhancement of susceptibility of these Kondo singlet order by skyrmion can still sustain obviously, even with parameters beyond

Here $E'_{m,j} = \sqrt{v_\psi^2 k_{m,j}^2 + g_\psi^2}$ and the coefficient D_η is obtained from the normalization condition $\|\psi_{\pm,m,j,n,\eta}\|^2 \equiv \int d^2x \langle \psi_{\pm,m,j,n,\eta} \lfloor \psi_{\pm,m,j,n,\eta} \rangle = 1$. We diagonalize the matrix with elements $\langle \Psi_{\pm,m,j,n,\eta} | H_f + \Delta \hat{M} | \Psi_{\pm,m',j',n',\eta} \rangle$.

As shown in Fig. 3.7, we have found that the enhancement of these Kondo singlet orders by skyrmion is comparable with the enhancement of VBS orders. Moreover, the enhancement of Kondo singlets is also sustained over a broad parameter space, including the regime where perturbative arguments may not be applicable. Therefore, we conclude that the Kondo singlet and VBS orders act as the dominant competing orders inside a skyrmion core. Therefore, the paramagnetic phase in the global phase diagram can support both of these competing singlet orders.

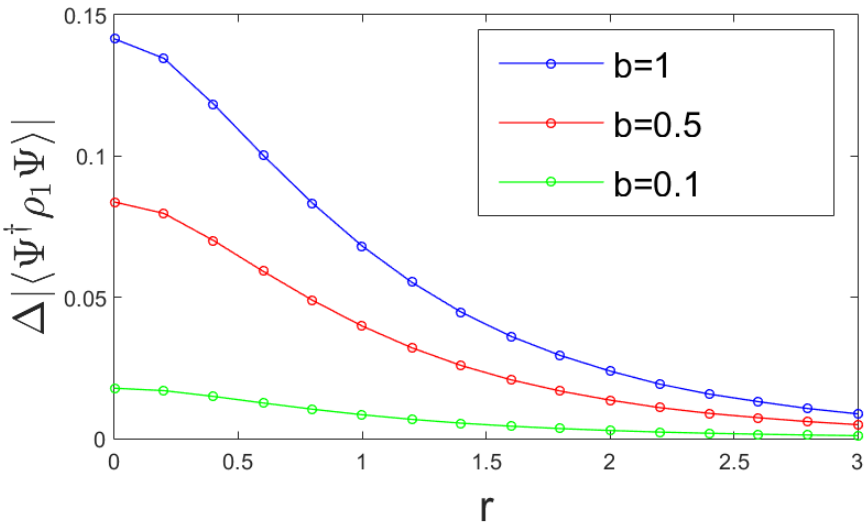

Figure 3.8 : The difference of Kondo singlet order $\langle \rho_1 \rangle$ between the presence and the absence of the skyrmion on origin for different fluctuation strength b. We choose $v_\psi = 1$, $v_{\chi=} = -1$, $g_\psi = 2$, and $g_\chi = -3$ and $Q = 0$ here. $\Delta|\langle\Psi^\dagger\rho_1\Psi\rangle|$ is defined as $\Delta|\langle\Psi^\dagger\rho_1\Psi\rangle| \equiv |\langle\Psi^\dagger\rho_1\Psi\rangle|_1 - |\langle\Psi^\dagger\rho_1\Psi\rangle|_0$, where $|\langle\Psi^\dagger\rho_1\Psi\rangle|_1$ and $|\langle\Psi^\dagger\rho_1\Psi\rangle|_0$ means $|\langle\Psi^\dagger\rho_1\Psi\rangle|$ calculated in the background with and without single skyrmion, respectively.

3.4.3 Crossover between VBS and Kondo order

The Hamiltonian of Eq. (3.10) is only useful for describing low energy physics inside the antiferromagnetic phase. In the vicinity of a magnet to paramagnet phase transition, such description is not sufficient to capture all features of the Kondo lattice model, since the fluctuations for competing channels and residual interactions in those channels can become important. The effective Hamiltonian describing the competition among VBS, Kondo singlet, and AF phases for a Kondo lattice model can be postulated to have the form

$$H = H_{\Psi} + b\rho_1 + Q\tau_1 \frac{\rho_0 - \rho_3}{2}, \tag{3.23}$$

where b and Q capture the fluctuations for Kondo and VBS channels and increase with J_K, J_H respectively [97, 100]. The presence of $\frac{\rho_0-\rho_3}{2}$ reflects that the VBS order in a Kondo lattice model can only be generated through the frustrated RKKY interactions between local moments.

From the perspective of AF Hamiltonian H_{Ψ}, the fluctuations of VBS and Kondo channels serve as external perturbation, and thus induce the corresponding order parameters approximately as:

$$\begin{aligned} \langle \chi^{\dagger} \tau_1 \chi \rangle &\cong Q \chi_{VBS}(r) \\ \langle \Psi^{\dagger} \rho_1 \Psi \rangle &\cong b \chi_{Kondo}(r) \end{aligned} \tag{3.24}$$

where $\chi_{VBS}(r)$ and $\chi_{Kondo}(r)$ are the local susceptibilities of VBS and Kondo orders, respectively.

Since we have already observed that the skyrmion defect of AF order can enhance the susceptibility of VBS and Kondo order inside AF phase, we expect that the VBS and Kondo order parameters induced by these fluctuations will also be enhanced by skyrmion. Moreover, once the $J_K(J_H)$ is enlarged, that is, the fluctuation

into Kondo(VBS) channel is larger, from Eq. (3.24), the resulting enhancement of Kondo(VBS) order parameter by skyrmion should also be enlarged.

This behavior actually is also manifested by solving the Hamiltonian of Eq. (3.23) directly and computing the resulting order parameters, as shown in Fig. 3.8. Therefore, once we increase the Kondo coupling in microscopic Kondo lattice model, the skyrmion will eventually favor Kondo order over the VBS order, causing the transition from VBS to Kondo phases. This result gives us a unifying point of view to understand the crossover between VBS and Kondo orders in a Kondo lattice model, beginning from the antiferromagnetic phase.

3.5 Justification by lattice models

So far, the model we relied on are different kinds of low energy effective Dirac-type Hamiltonian. In these models, the presence of large momentum cut-off is practically inevitable, even though all of our conclusions hold regardless of cut-offs. In order to further justify these results, we have also solved the lattices models in the presence of skyrmion defect (whose low energy effective theory is equivalent to $H_\Psi + \Delta\hat{M}$ for different candidate competing orders in TABLE 3.1 and Table 3.2) through exact diagonalization. For example, the VBS order $\hat{M} = \tau_1$ can be generated through the lattice model:

$$H = \sum_{\langle ij\rangle\alpha}\left[-t_f f^\dagger_{i,\alpha} f_{j,\alpha} - t_c c^\dagger_{i,\alpha} c_{j,\alpha} + h.c\right] + \sum_{i\alpha\beta}\Big[J_H\,(-1)^{A=0,B=1}\, f^\dagger_{i,\alpha}\frac{(\boldsymbol{n}\cdot\boldsymbol{\eta})_{\alpha\beta}}{2} f_{i,\beta} + J_K\,(-1)^{A=1,B=0}\, c^\dagger_{i,\alpha}\frac{(\boldsymbol{n}\cdot\boldsymbol{\eta})_{\alpha\beta}}{2} c_{i,\beta}\Big] \tag{3.25}$$

if we replace $t_f \to t_f + \delta t_{r,r+s_i}$ and $t_c \to t_c + \delta t_{r,r+s_i}$, where $\delta t_{r,r+s_i} = \Delta e^{i\vec{K}_+\cdot\vec{s}_i} e^{i\vec{G}\cdot\vec{r}}/3 + h.c$ and $G = K_+ - K_-$, as Fig. 3.9. The resulting low energy effective Hamiltonian

of this model is exactly the same as $H_\Psi + \Delta\tau_1$ [119]. By assigning the skyrmion configuration for local moment field $\boldsymbol{n}$, we can explore its influence on VBS order parameter in a lattice model. The presence of skyrmion in the lattice model also causes spectral flow events as in Fig. 3.10, which is consistent with the low energy continuum theory. The VBS order parameter in lattice model can be extracted through the nearest-neighbor hopping amplitude. After solving the lattice model, we can see that the presence of skyrmion enhances the VBS order parameter as shown in Fig. 3.11(a). Similar results for other competing orders are presented in Fig. 3.11. All of the results are consistent with our previous findings based on low energy Dirac theory.

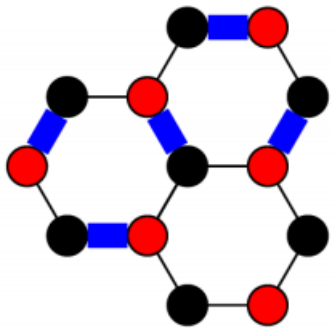

Figure 3.9 : The VBS pattern with $\delta t_{r,r+s_i} = \Delta e^{i\vec{K}_+\cdot\vec{s}_i} e^{i\vec{G}\cdot\vec{r}}/3 + h.c$. The blue thick(black thin) lines indicate hopping amplitude is increased(decreased) by $\frac{2\Delta}{3}(\frac{\Delta}{3})$.

3.6 Discussion

In the field theory literature, the nonperturbative eigenstates of Dirac fermions have been already employed for computation of induced fermion numbers [120, 121, 122, 123, 108, 124, 99]. Some famous examples are the induced chiral charge of a domain wall in one dimension, and baryon number of O(4) skyrmions in three dimensions. A similar analysis has also been performed for O(3) skyrmions in two spatial dimensions.

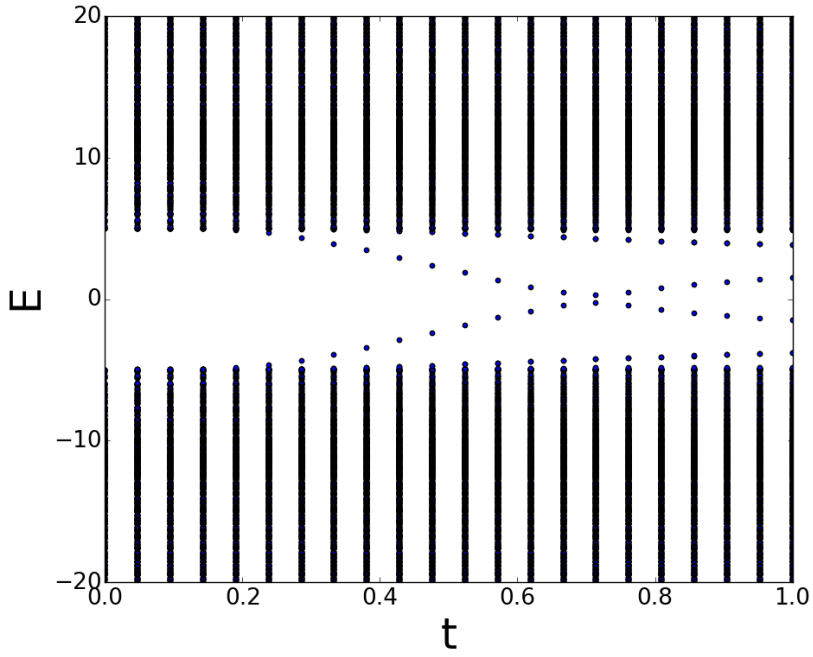

Figure 3.10 : The spectrum flow during the formation of skyrmion for lattice Hamiltonian 3.25 involving f-electron only. We choose coupling constant $J_H = 5$, $t_f = 10$ and simulate the formation of skyrmion by $\boldsymbol{n}(\vec{r}_i, t) = (\sin tf(r_i)\cos\theta, \sin tf(r_i)\sin\theta, \cos tf(r_i))$, where $f(r_i) = \pi e^{-\frac{r_i}{2}}$ and r_i is the radial position of the site i. There is one state flowing from negative state to positive state, and precisely one state flowing oppositely. This is just a reflection of relation 3.11, since the spectrum here consists of + and - valley.

However, the physical issue of competing orders and the determination of dominant fluctuating order based on nonperturbative eigenbasis are new aspects of the present work. To the best of our knowledge previous analysis along this direction has been restricted to competing orders in a vortex core (defects of Abelian theory).

Since we are explicitly solving for the eigenstates of the Dirac Hamiltonian, we can also employ these states for computing the competing orders away from half-filling. Not much is known for such a situation from perturbative field theory. Th chiral charge also acts as the generators for translational symmetry breaking paired states

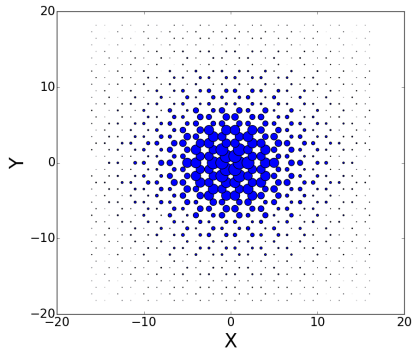

(a) VBS order $\hat{M} = \tau_1$

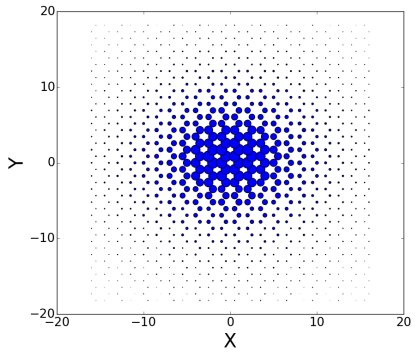

(b) charge density wave order $\hat{M} = \tau_1\sigma_1$

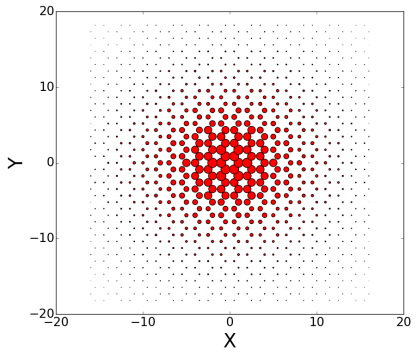

(c) current density wave order $\hat{M} = \tau_1\sigma_3$

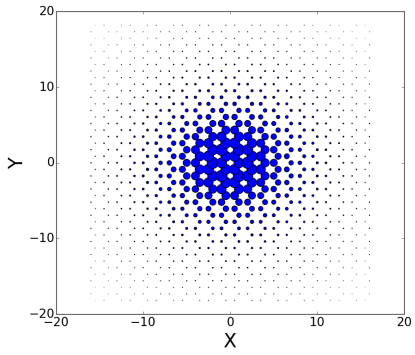

(d) Kondo singlet order $\hat{M} = \rho_1$

Figure 3.11 : The difference between distinct order parameters in the presence and absence of a skyrmion at the origin. Here we solve the lattice Hamiltonian whose low energy effective model is $H_\Psi + \Delta\hat{M}$. The blue circle means the difference is positive, and the bigger circle indicates the difference is larger. We can see obviously that VBS, charge density wave, and Kondo singlet order gain enhancement near the core of skyrmion, while the current density wave is suppressed due to the presence of skyrmion, which is consistent with the results from low energy Hamiltonian in last section. Similar conclusions hold for other order parameters listed in TABLE 3.1 and 3.2.

(FFLO states). At half-filling they do not produce fully gapped states and are less favorable compared to spin-Peierls order (causing Dirac mass gap). However, when we move away from the special case of half-filling, the paired states are more effective

in gap formation. Therefore, we expect FFLO phases to become more important in the generic situation of finite carrier density. Even current and charge density wave orders which were earlier disfavored compared to spin-Peierls order can become more important (as none of them are able to effectively gap out the Fermi surface). Such intriguing competition among particle-hole and particle-particle channel condensates are germane to understanding the generic global phase diagrams of correlated metals, and will be elucidated in a future publication.

Our methodology can be easily adapted for both higher and lower dimensional problems. Specifically, the computed energy-eigenstates for two dimensional model in the presence of skyrmion configuration can be directly taken over as the complete eigenbasis for evaluating the fermion determinant in one dimension in the presence of dynamic instanton background. Such calculations can again be performed both at and away from half-filled limit to unveil the competition among spin-Peierls, Kondo singlets and paired states, which have been suggested by different perturbative calculations as well as some density matrix renormalization group analysis.

3.7 Conclusion

We addressed the nonperturbative aspects of interaction between topological defects and fermions, and how it can give rise to competition among different order parameters. Specifically, we considered the interaction between topologically nontrivial skyrmion configurations of antiferromagnetic phase and fermionic quasiparticles in two spatial dimensions. To make progress we have modeled the fermionic excitations by Dirac fermions. Beginning with a half-filled Kondo-Heisenberg model on a honeycomb lattice, we investigated fluctuating orders that can be supported by skyrmion core inside the antiferromagnetically ordered insulating phase. Inside this

ordered state, we have considered the coupling between conduction and f-electrons to the collective mode, described in terms of an O(3) quantum nonlinear sigma model(QNLσM). By employing perturbative field theory, exact numerical and analytical solutions for eigenfunctions of Dirac fermions in the presence of a single skyrmion we have established the competition between magnetism, Kondo singlet formation and spin Peierls order. Our specific goal was to establish a framework for finding dominant order parameter, which can be adapted for many other problems involving the interaction between fermion and topological defects. The perturbative field theory calculation of Goldstone-Wilczek current for our model suggests the presence of several translational symmetry breaking orders such as charge, bond and current density waves as well as translational symmetry preserving Kondo singlet formation. However, this method does not clearly specify the dominant incipient order. Therefore, we have explicitly computed the susceptibilities for all possible local Dirac bilinears by using nonperturbatively determined eigenfunctions. Our analysis thus provides strong evidence that the global phase diagram of Kondo-Heisenberg can support a variety of competing singlet orders from skyrmion condensation (violation of skyrmion number) on the paramagnetic side. All of our results from continuum model have been consistently justified by analysis performed on suitable lattice model. This general strategy for identifying dominant competing orders mediated by topological defects can be useful in both one and three spatial dimensions.

Chapter 4

Quantum criticality of a quantum nonlinear sigma model with Kondo coupling: A renormalization group study

4.1 Introduction

Quantum criticality is ubiquitous in many strongly correlated systems, and believed to play an essential role in the electronic or magnetic properties of these systems[21, 3]. For a long time, the paradigmatic Hertz-Millis theory of magnetic quantum criticality had only focused on the fluctuations of the order parameter alone[38, 39]. In recent years, both experimental and theoretical works have challenged such paradigm[65, 81, 55, 56].

Some of the important progress comes from the heavy fermion systems. As we have introduced in Chapter 2, the Hertz-Millis paradigm fails to explain the ω/T scaling in $CeCu_{6-x}Au_x$ at $x = x_c \approx 0.1$[63] and $YbRh_2Si_2$[64].

Moreover, in heavy fermion systems, not only the Kondo coupling but also the frustration of the local moments could cause the AF phase into another kind of paramagnetism[1, 30, 2]. Since the Kondo singlet formation is absent in such transition, the Fermi surface of this paramagnetism should still remain small, and thus such paramagnetism is usually denoted as P_S. The proposed global phase was summarized in Fig. (1.2). Recent experimental result in the geometrically frustrated heavy fermion metal CePdAl has demonstrated that such frustration-driven transition is

realistically possible in heavy fermion systems[34].

Motivated by these developments, in this work, we start from an AF ordered Kondo lattice model. Because of the Kondo coupling, the AF order parameter, which should be a bosonic degree of freedom, also couples with the conduction electrons. From the theoretical point of view, the interplay between the bosonic degree of freedom and the itinerant fermion with the Fermi surface pose a difficulty for the theorist to deal with. Even though some progress has been made in the last decade[125, 126, 127, 128], how to deal with the Kondo lattice model and the local moment physics still remains a challenge.

Here, we show that by using a quantum non-linear sigma model to represent the local moments, some progress can still be made. The validity of the QNLσM representation to the AF Kondo lattice model has been established in the previous work[129]. However, previous studies of similar models either follow the spirit of conventional Hertz-Millis theory by integrating out the conduction electrons[130], or only focus on the role of the Kondo coupling inside the AF ordered phase[129].

In this work, we treat the bosonic and fermionic degree of equal footing, and perform a renormalization group calculation beyond the AF ordered phase. Without the Kondo coupling, such QNLσM is known to have a quantum phase transition from AF_S to P_S at $D > 1$[50]. We are especially interested in the influence of the Kondo coupling to this QCP, and whether the small Fermi surface nature would be destroyed by the Kondo coupling or not.

4.2 Model

The Kondo lattice model is:

$$H = \sum_{k,\sigma} \epsilon_k \psi^{\dagger}_{k,\sigma} \psi_{k,\sigma} + J_H \sum_{\langle ij \rangle} \vec{S}_i \cdot \vec{S}_j + J_K \sum_i \vec{S}_i \cdot \vec{s}_i \tag{4.1}$$

where $\vec{S}_i$ and $\vec{s}_i = \sum_{\alpha\beta} \psi^{\dagger}_{i,\alpha} \frac{\vec{\sigma}_{\alpha\beta}}{2} \psi_{i,\beta}$ is the spin operator of the local moment and conduction electron, respectively, and both the RKKY J_H the Kondo coupling J_K are positive.

Here, we start from the antiferromagnetic(AF) region, i.e. $J_K \ll J_H \ll W$, where W is the bandwidth of the electron spectrum. Inside the AF phase, the local moments and the conduction electrons are essentially decoupled, the quantum non-linear sigma model(QNLSM) representation of the local moments thus is applicable[129], where the local moment $\vec{S}_i$ can be approximated by the non-linear sigma field $\vec{n}(\vec{x}, \tau)$ charactering the Neel order of the AF phase [129, 45, 46, 131], and the canting field $\vec{L}(\vec{x}, \tau)$ describing the fluctuation around the non-linear sigma field $\vec{n}(\vec{x}, \tau)$:

$$2\vec{S}_i \rightarrow e^{i\vec{Q}\cdot\vec{x}} \vec{n}(\vec{x}, \tau) \sqrt{1 - \left(2a^D \vec{L}(\vec{x}, \tau)\right)^2} + 2a^D \vec{L}(\vec{x}, \tau) \tag{4.2}$$

where $\vec{Q}$ is the ordering wave vector, $\vec{x}$ labels the position, $\eta_{\vec{x}} = \pm 1$ on even and odd sites, a is the lattice constant, $\vec{n}(\vec{x}, \tau) \cdot \vec{L}(\vec{x}, \tau) = 0$, and $|\vec{n}(\vec{x}, \tau)| = 1$. For the sake of simplicity, in the following, in the following we take the square lattice with ordering wave vector $\vec{Q} = \left(\frac{\pi}{a}, \frac{\pi}{a}\right)$ as an example. All of the results can be easily generalized in other lattice structures.

Even though such QNLSM description of quantum magnetism was originally invented inside the AF ordered phase, its power to infer some properties of critical point or even the physics of the AF disordered side have been demonstrated in lots of different works[55, 56, 50, 132, 133]. Now we are going to incorporate the Kondo

coupling. We focus on the case in which there is no Fermi surface nesting and hence no hot-spots. The linear coupling $\vec{n}\cdot\vec{s}_c$ thus cannot connect any two points on the Fermi surface and is unimportant for the low energy physics. The Kondo coupling is thus replaced by $\vec{L}\cdot\vec{s}_c$. After integrating out the fluctuating canting field $\vec{L}\left(\vec{x},\tau\right)$, the resulting QNL$\sigma$M representation of the Kondo lattice model (4.1) is[129]:

$$\begin{aligned} S &= S_f + S_n + S_K \\ S_f &= \sum_{\sigma}\int d^D K d\Omega \psi^{\dagger}_{\vec{K}\Omega,\sigma}\left(i\Omega-\epsilon_{\vec{K}}\right)\psi_{\vec{K}\Omega,\sigma} \\ S_n &= \frac{1}{2g}\int d\tau d^D x\left(\frac{1}{c^2}\left(\partial_\tau\vec{n}\right)^2+\left(\nabla\vec{n}\right)^2\right) \\ S_K &= \lambda_K\int d\tau d^D x\left(\vec{s}_c\cdot\left(\vec{n}\times i\partial_\tau\vec{n}\right)\right) \end{aligned} \tag{4.3}$$

where $g=\frac{a^{D-2}}{S^2}\frac{I_1}{I_1-2I_2}$, $c=2aSI_1\sqrt{D}\sqrt{\frac{I_1-2I_2}{I_1}}$, $\lambda_K=\frac{J_K}{4DI_1a^D}$. We ignore the Berry phase term in action (4.1) since our analysis starts from an AF ordered phase, in which the the Berry phase term vanishes.

To impose the non-linear constraint $\left|\vec{n}\left(\vec{x},\tau\right)\right|=1$, we introduce $\vec{\pi}=\left(\pi_+,\pi_-\right)$ to represent the NLS field $\vec{n}$ as:

$$\vec{n}=\left(\vec{\pi},\sigma\right) \tag{4.4}$$

where $\vec{\pi}=\left(\pi_+,\pi_-\right)$ is a two components vector, and $\sigma=\sqrt{1-\vec{\pi}^2}\cong 1-\frac{1}{2}\left(\pi_+^2+\pi_-^2\right)+\cdots$. Therefore,

$$\begin{aligned} \partial_\tau\vec{n} &= \left(\dot{\pi}_+,\dot{\pi}_-,\frac{-\dot{\pi}_+\pi_+-\dot{\pi}_-\pi_-}{\sigma}\right) \\ \vec{n}\times\partial_\tau\vec{n} &= \begin{pmatrix} \frac{1}{\sigma}\left(-\dot{\pi}_- -\dot{\pi}_+\pi_+\pi_- +\pi_+\pi_+\dot{\pi}_-\right) \\ \frac{1}{\sigma}\left(\dot{\pi}_+ +\dot{\pi}_-\pi_-\pi_+ -\pi_-\pi_-\dot{\pi}_+\right) \\ \dot{\pi}_-\pi_+ -\pi_-\dot{\pi}_+ \end{pmatrix} \end{aligned} \tag{4.5}$$

To simplify the later RG analysis, in the following part, we rescale the fields $\vec{\pi}\to\sqrt{g}\vec{\pi}$.

Consequently, the propagator of the $\vec{\pi}$ fields is:

$$G_{\pi}\left(\vec{p}, i\omega\right) = \frac{1}{\frac{\omega^2}{c^2} + p^2} \tag{4.6}$$

Because of the non-linear constraint $|\vec{n}\left(\vec{x}, \tau\right)| = 1$, the model (4.3) actually possesses infinite numbers of local interaction. To our concern in this paper, we only need to consider some leading orders of them, and the relevant Feynman rules are shown in Fig. (4.1).

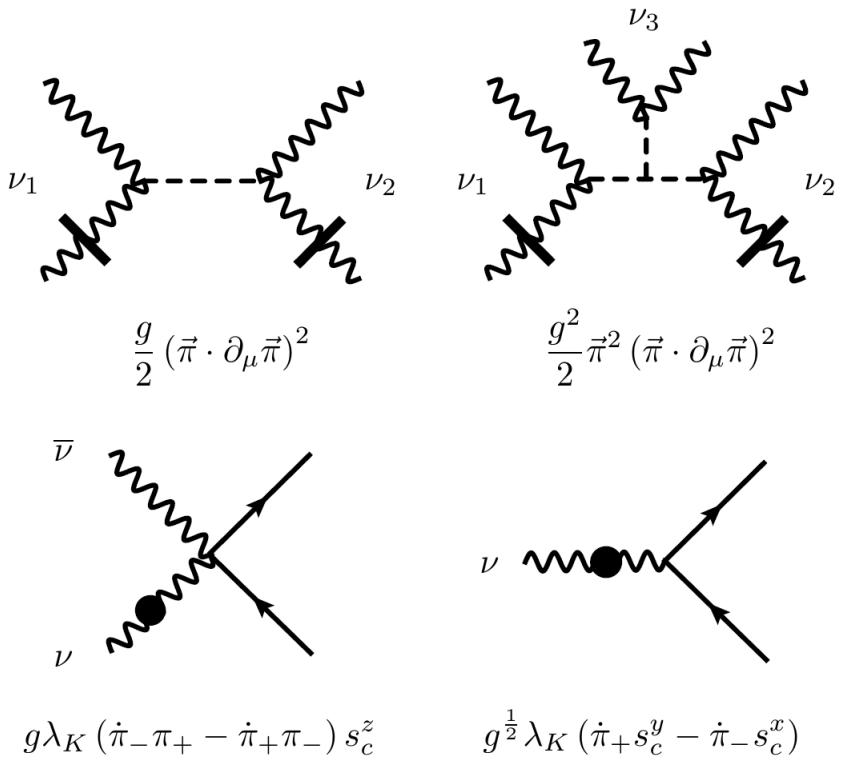

Figure 4.1 : The Feynman rules of the action (4.3) after rescaling $\vec{\pi} \to \sqrt{g}\vec{\pi}$, where $\partial_\mu = \left(\frac{1}{c}\partial_\tau, \vec{\partial}\right)$. The solid arrow line and the curve line are the propagator of the fermionic and bosonic field, respectively. The bar on the bosonic propagator denotes both the time and space derivatives, while the dot on the bosonic propagator refer to the time derivative merely.

4.3 Renormalization group with Fermi surface

Our next step is to carry out the renormalization group(RG) analysis of the action (4.3) by the ϵ expansion, where $\epsilon = D - 1$ and D is the spatial dimensions. Our analysis involves the combination of both the bosonic and fermionic degree of freedom. In this section, we firstly derive the beta functions at the tree level, which can be done by simple dimensional counting.

For the bosonic degree of freedom with the propagator (4.6), if we count the dimension by assigning $[p] = 1$, $[\omega] = 1$, then the scaling dimension of the bosonic field $\vec{\pi}$ is:

$$[\pi] = -\frac{D+3}{2} \tag{4.7}$$

which means after the rescaling $q \to bq$, $\omega \to b\omega$, the bosonic field rescales as $\pi \to b^{-\frac{D+3}{2}}\pi$ in order to keep the the propagator (4.6) invariant. By the scaling dimension (4.7), one can easily check that:

$$[g] = -\epsilon = -(D-1) \tag{4.8}$$

However, for the fermionic part, things become subtle. It has been recognized that the presence of the Fermi surface can influence the RG analysis in a dramatic manner[134]. To demonstrate that, let us firstly linearize the dispersion $\epsilon_{\vec{K}} = v_F k$, where $k = |\vec{K}| - K_F$ is the momentum relative to the Fermi momentum K_F, and v_F is the Fermi velocity. Therefore, the fermionic propagator is:

$$G_\psi\left(\vec{K}, i\Omega\right) = \frac{1}{i\Omega - v_F k} \tag{4.9}$$

Since the fermionic excitations lie within the vicinity of Fermi surface, after integrating out the fast modes whose momentum lying within $\left[\frac{\Lambda}{s}, \Lambda\right]$, where Λ is the

momentum cut-off, the integral $\int^{\Lambda} d^D K$ becomes:

$$\int^{\Lambda/s} d^D K \equiv \int d^{D-1}\Omega_{\vec{K}} \int_{K_F-\frac{\Lambda}{s}}^{K_F+\frac{\Lambda}{s}} K^{D-1} dK \tag{4.10}$$

However, one can easily see that no simple rescaling of K can restore the integral back to the original form. This difficulty results from the constraint that the momentum of the original fermionic theory is defined within the vicinity shell of the Fermi surface, so that simple rescaling of K would break this momentum constraint. To overcome this difficulty, it was pointed out that only the momentum perpendicular to Fermi surface should be rescaled[134], since

$$\begin{aligned} \int^{\Lambda/s} d^D K &\equiv \int d^{D-1}\Omega_{\vec{K}} \int_{K_F-\frac{\Lambda}{s}}^{K_F+\frac{\Lambda}{s}} K^{D-1} dK \\ &= \int d^{D-1}\Omega_{\vec{K}} \int_{-\frac{\Lambda}{s}}^{\frac{\Lambda}{s}} (k+K_F)^{D-1}\, dk \\ &\cong K_F^{D-1} \int d^{D-1}\Omega_{\vec{K}} \int_{-\frac{\Lambda}{s}}^{\frac{\Lambda}{s}} dk \end{aligned} \tag{4.11}$$

Therefore, we have $\left[d^D K\right] = [dk] = 1$, and the scaling dimension of the fermionic field ψ thus is:

$$[\psi] = -\frac{3}{2} \tag{4.12}$$

where we count $[k] = 1$, $[\Omega] = z = 1$, and the dynamical exponent $z = 1$ since there is no Fermi surface nesting, and hence no extra damping effect. Following these manners, one can easily count the dimension of the the unrescaled Kondo coupling λ_K. Use the Ising Kondo vertex $\lambda = g\lambda_K$ in Fig.(4.2) as an example, since*

*Reader might note that there are different choices to label the momentum, and the dimension of the coupling constant λ naively seems to depend on the choice. However , in order for the boson-fermion coupling term to satisfy momentum conservation, it turns out the relative angle (which does not appear in the measure) between the incoming fermion $\vec{K}$ and outgoing fermion $\vec{K}+\vec{p}+\vec{q}$ must also

$$
\begin{aligned}
&\left[d^D K d\Omega d^D p d\omega d^D q d\nu \omega \pi_- \pi_+ \psi_\sigma^\dagger \psi_\sigma\right] \\
&= 1 + 1 + D + 1 + D + 1 + 1 + 2\left(-\frac{3}{2}\right) + 2\left(-\frac{D+3}{2}\right) \\
&= D - 1
\end{aligned}
\tag{4.13}
$$

we thus have:

$$
[\lambda] = [g\lambda_K] = -\epsilon = -(D-1) \Rightarrow [\lambda_K] = 0 \tag{4.14}
$$

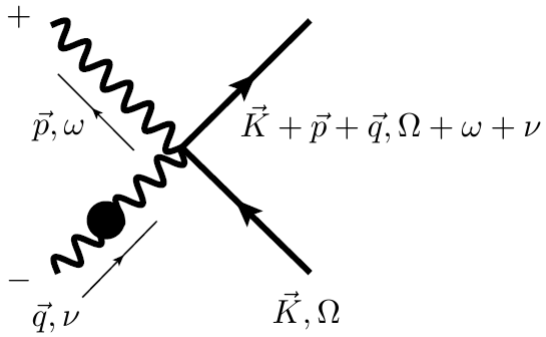

Figure 4.2 : Ising component of Kondo coupling $\lambda = g\lambda_K$.

That is, the Kondo coupling λ_K is marginal at the tree level and any dimension. As we have seen, this is closely related to the momentum constraint due to the presence of the Fermi surface discussed above. Such momentum constraint actually causes much more dramatic consequence. As discussed by S. Yamamoto and Q. Si in Ref.[129], inside the AF ordered phase, the Kondo coupling λ_K is exactly marginal because of the huge constraint on the momentum phase space. Take Fig. (4.3)

---

need to scale, otherwise the momentum of bosonic fields can not be rescaled homogeneously[129]. Consequently, our choice of labelling here in Fig. (4.2) is the most convenient one to count the dimension of coupling constants.

as an example. Because of the momentum constraint, the phase space of the loop correction is severely limited, and hence this loop correction does not contribute to the Beta function of λ_K. As a result, the Kondo coupling λ_K is exactly marginal inside AF ordered phase.

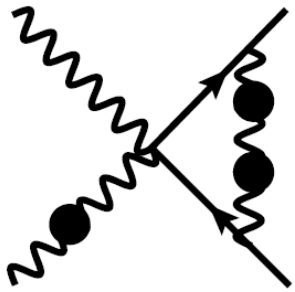

Figure 4.3 : One loop correction to $\lambda = g\lambda_K$ inside the AF phase.

4.4 Renormalization group analysis of Kondo coupling at the critical point

The previous conclusion that the Kondo coupling λ_K is exactly marginal holds only inside the AF ordered phase. In this work, we want to study the influence of the Kondo coupling outside the AF ordered phase through the renormalization group(RG) analysis, as shown in the schematic diagram in Fig. (4.4). As we will see, beyond the AF ordered phase, other loop corrections which are vanishing inside the AF ordered phase, can make contribution to the Beta function of λ_K. We are especially interested in the role of the Kondo coupling to the original quantum critical point(QCP) of the QNLSM[50]. Such QCP describes a phase transition between the AF ordered phase

and and a paramagnetic phase. It is interesting to see whether the presence of a Kondo coupling would modify such paradigm.

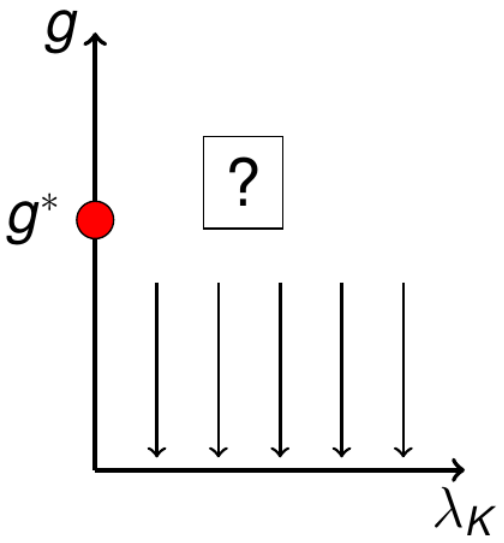

Figure 4.4 : The schematic RG flow diagram. The red dot is the QCP of QNLSM, and the RG flow in the question mark region is what we would like to explore in this work.

4.4.1 Beta functions of Kondo coupling

We perform the RG calculation in the momentum shell scheme[129, 50, 49, 135]. The first step is to decompose both the bosonic and fermionic fields into fast and slow modes as:

$$\pi_\nu\left(i\omega,\vec{q}\right)=\begin{cases}\pi_{\nu,<}\left(i\omega,\vec{q}\right), & 0<|\vec{q}|<\frac{\Lambda}{b}\\ \pi_{\nu,>}\left(i\omega,\vec{q}\right), & \frac{\Lambda}{b}<|\vec{q}|<\Lambda\end{cases} \tag{4.15}$$

and

$$\psi_\sigma\left(i\Omega,\vec{K}\right)=\begin{cases}\psi_{\sigma,<}\left(i\Omega,\vec{K}\right), & 0<||\vec{K}|-K_F|<\frac{\Lambda}{b}\\ \psi_{\sigma,>}\left(i\Omega,\vec{K}\right), & \frac{\Lambda}{b}<||\vec{K}|-K_F|<\Lambda\end{cases} \tag{4.16}$$

where $b>1$.

After integrating out the fast modes $\pi_{\nu,>}\left(\vec{q}\right)$ and $\psi_{\sigma,>}\left(\vec{K}\right)$, in order to restore the resulting action back to its original form, one also needs to do the rescaling $q\rightarrow bq$, $\omega\rightarrow b\omega$, $\pi\rightarrow\xi_\pi^{-1}\pi$, and $\psi\rightarrow\xi_\psi^{-1}\psi$. The loop correction to the bosonic propagator shown in Fig. 4.5(a) gives:

$$1=\left(1+\frac{K_D\Lambda^{D-1}}{2c}g\right)\xi_\pi^{-2}b^{(D+3)} \tag{4.17}$$

and the loop correction to the coupling g and $\lambda=g\lambda_K$ in Fig. 4.5(b) and 4.5(c) respectively give:

$$g'=g\left(1+\frac{3K_D\Lambda^{D-1}}{2c}g\right)\xi_\pi^{-4}b^{(3D+5)} \tag{4.18}$$

and

$$\lambda'=\lambda\left(1+\frac{K_D\Lambda^{D-1}}{2c}g\right)\xi_\pi^{-2}\xi_\psi^{-2}b^{(2D+5)} \tag{4.19}$$

Here we calculate the renormalization of the coupling constant g by considering the loop correction to the vertex $\frac{g}{2}\left(\vec{\pi}\cdot\partial_\mu\vec{\pi}\right)^2$, which involves numerous Feynman diagrams as listed in Fig. (4.5)(b). Actually, there is a much less tedious way to do so. Conventionally, the renormalization g of the QNLSM part S_n is derived by adding a magnetic field term $S_h=\frac{h}{g}\int d\tau d^Dx\sigma=\frac{h}{g}\int d\tau d^Dx\sqrt{1-\vec{\pi}^2}=\frac{h}{g}\int d\tau d^Dx\left(1-\frac{1}{2}\vec{\pi}^2+\cdots\right)$ to S_n, and then require that after intergrating out the fast mode, the whole form of S_h still preserve but with a renormalzied overall factor $\frac{h'}{g'}$ [47, 48]. The validity of this method relies on the fact that the QNLSM S_n preserves the $O\left(3\right)$ symmetry. Even with the presence of a non-vanishing Kondo coupling λ_K, one can still use this method to derive the coupling constant g, since under the $O\left(3\right)$ rotation, $\vec{n}\rightarrow R\vec{n}$, and thus

$\vec{n} \times i\partial_\tau \vec{n} \to R\left(\vec{n} \times i\partial_\tau \vec{n}\right)$, which can be compensated by a suitable $SU\left(2\right)$ transform U on the fermionic field $\psi \to U\psi$. As the result, the action (4.3) still preserves the $O\left(3\right)$ symmetry even with the Kondo coupling λ_K.

In Fig. 4.5(c) , we ignore the one-loop correction shown in Fig. (4.3), since as discussed in the last section, it does not contribute to the Beta function. Moreover, the one-loop diagrams in Fig. 4.5(d) are vanishing, since the two conduction electron poles are located on the same side of the real axis[134].

Finally, as we have seen in last section, since $[\psi] = -\frac{3}{2}$ the rescaling factor ξ_ψ is:

$$\xi_\psi = b^{\frac{3}{2}} \tag{4.20}$$

By Eq. (4.17)-(4.20), we can derive the Beta functions up to one-loop level:

$$\begin{aligned} \beta\left(g\right) &= -\epsilon g + g^2 \\ \beta\left(\lambda\right) &= -\epsilon\lambda \end{aligned} \tag{4.21}$$

where we have made a harmless rescaling $g \to \frac{K_D \Lambda^{D-1}}{2c} g$.

From the Beta function $\beta\left(g\right)$, one can see that there is indeed a critical point at $g = g^* = \epsilon$ when $D > 1$. Also note that even though the Beta function $\beta\left(\lambda\right)$ seems to be only at tree-level, we actually perform the calculation up to the order of $g\lambda$ as indicated in the Eq. (4.17), and find the coefficient of this order in the $\beta\left(\lambda\right)$ actually gets cancelled in the end. Since in this work, we mainly concern about the role of Kondo coupling near the QCP of the QNLSM $g = g^* = \epsilon$, other higher-order terms are unnecessary for such purpose.

Now we are at the stage to analyse the role of the Kondo coupling λ_K near the QCP $g = g^* = \epsilon$. Since the rescaled Kondo coupling $\lambda = g\lambda_K$, one has:

$$\beta\left(\lambda\right) = g\beta\left(\lambda_K\right) + \lambda_K \beta\left(g\right) \tag{4.22}$$

(a)

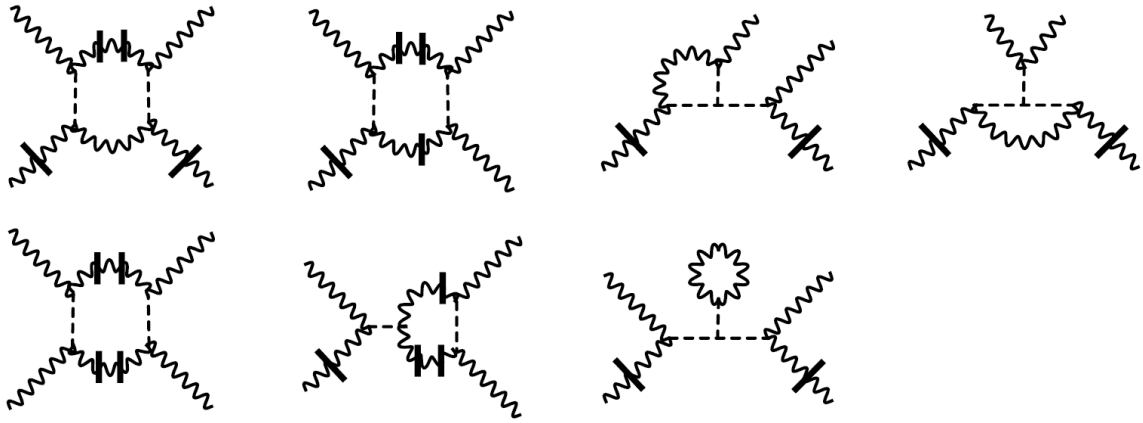

(b)

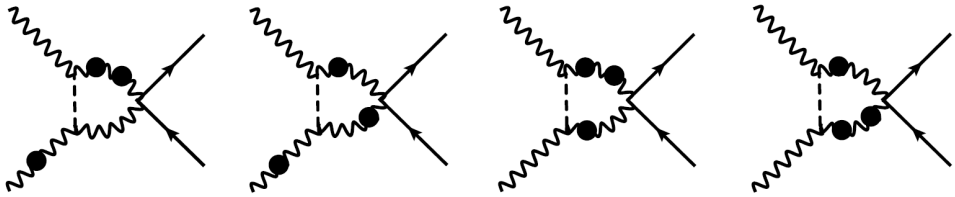

(c)

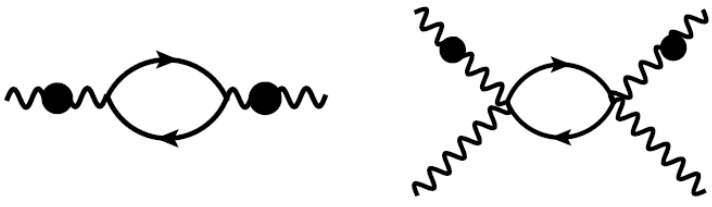

(d)

Figure 4.5 : (a) One-loop correction diagrams for the bosonic propagator (b) for the coupling constant g. (c) for the Ising Kondo coupling. (d) Diagrams involve the electronic particle-hole polarization are vanishing.

By combining this relation and the Beta functions (4.21) , one can derive the Beta function of the original unrescaled Kondo coupling λ_K:

$$\beta(\lambda_K) = -g\lambda_K \tag{4.23}$$

In the Eq. (4.23), we derive the Beta function of the Kondo coupling λ_K from the Ising Kondo vertex in Fig. (4.1). As we have proven, since the action (4.3) is invariant under $O(3)$ rotation, one should be able to derive the consistent result of the Beta function of the Kondo coupling λ_K from both the Ising and XY Kondo vertices. We demonstrate how to derive such consistent result from XY Kondo vertices in the Appendix (B.1).

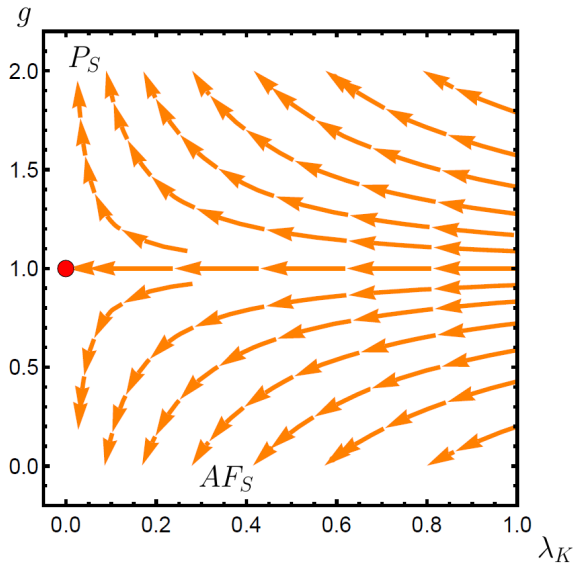

Figure 4.6 : RG flow of g and λ_K, where the red dot denotes the QCP of QNLSM $g = g^* = \epsilon$.

We see from Eq. (4.22) that at the AF fixed point $g = 0$, the Kondo coupling λ_K is indeed marginal. On the other hand, around the QCP of the QNLSM $g = g^* = \epsilon$, λ_K is irrelevant. Moreover, Eq. (4.22) also implies that at AF disordered phase

$g > g^* = \epsilon$, the Kondo coupling should be irrelevant, at least in the weak-coupling region. As a result, the AF to P_S transition should be stable against a weak Kondo coupling. The RG flow is shown in Fig. (4.6).

4.4.2 Electronic self-energy around the QCP

To verify explicitly that the Fermi surface indeed remains small even beyond the AF ordered phase, we turn to a large N generalization of the action (4.3). The $N \to \infty$ limit is taken with the spin symmetry of the conduction electrons enlarged from $SU(2)$ to $SU(N)$, and the symmetry of the bosonic field $\vec{\pi}$ from $O(2)$ to $O(N^2-2)$. The Kondo coupling is rescaled to $\lambda_K/\sqrt{N}$. As shown in Fig. (4.7), the leading order correction to the electronic self-energy is:

Figure 4.7 : Electronic self-energy induced by Kondo coupling, where double curve line is the bosonic propagator at QCP

$$\Sigma\left(\vec{K}, i\Omega\right) = \frac{g\lambda_K^2}{N}\int d^D q d\omega \omega^2 G_{\pi,*}\left(\vec{q}, i\omega\right) G_\psi\left(\vec{K}+\vec{q}, i\Omega + i\omega\right) \tag{4.24}$$

At the QCP of the QNLSM $g = g^*$, since there is an anomalous dimension of the $\vec{\pi}$ field, the bosonic propagator thus takes the form:

$$G_{\pi,*}\left(\vec{p}, i\omega\right) = \frac{1}{\left(\frac{\omega^2}{c^2} + p^2\right)^{1-\frac{\eta}{2}}} \tag{4.25}$$

where $\eta = \frac{\epsilon}{N-2}$ is the anomalous dimension of $\vec{\pi}$ field at the QCP[49, 47, 48].

To calculate the electronic self-energy $\Sigma\left(\vec{K}, i\Omega\right)$ (4.24), it is more convenient to use the spectral representation for the bosonic propagator $G_{\pi,*}\left(\vec{p}, i\omega\right)$:

$$G_{\pi,*}\left(\vec{p}, i\omega\right) = \int d\omega' \frac{A\left(\vec{p}, \omega'\right)}{\omega - i\omega'} \tag{4.26}$$

where the spectral function $A\left(\vec{p}, \omega'\right) = \operatorname{Im} G\left(\vec{p}, i\omega' \to \omega + i0^+\right)$ is

$$A\left(\vec{p}, \omega'\right) = C \frac{\Theta\left(\frac{\omega'^2}{c^2} - p^2\right)}{\left(\frac{\omega'^2}{c^2} - p^2\right)^{1-\frac{\eta}{2}}} \tag{4.27}$$

Following these, one can do the calculation and then derive[129, 136] that

$$\Sigma\left(\vec{K}_F, \omega\right) = a\omega + ib|\omega|^{D+\eta} \tag{4.28}$$

Since the imaginary part $\operatorname{Im}\Sigma\left(\vec{K}_F, \omega\right) \sim |\omega|^{D+\eta}$, at $D \geq 2$ the Fermi surface is thus still robust and small around the QCP of the QNLSM.

4.5 Discussion and Conclusion

In this section, we study the quantum non-linear sigma model with a Kondo coupling, which describes the antiferromagnetic Kodno lattice model. By treating both the bosonic and fermionic degrees on an equal footing, we perform an RG analysis of this model. Our RG analysis shows that the Kondo coupling is irrelevant around the QCP of the QNLσM. Therefore, the phase transition between the antiferromagnetism and the paramagnetism is stable against the weak Kondo coupling. By calculating the electronic self-energy induced by the Kondo coupling around the QCP, we conclude that the Fermi surface also remains small across the phase transition.

As a result, we are able to access and establish the transition between AF_S and P_S phases in the proposed global phase diagram of heavy fermion systems. The precise

nature of the small Fermi surface paramagnetic phase P_S requires further analysis. However, as we have discussed and demonstrated in chapter 3, if one also considers the influence of the topological defects and the Berry phase term, the small Fermi surface paramagnetic phase P_S for typical types of lattices should be the valence bond solid(VBS)[31, 32, 33, 53, 54, 55, 56]. The results in chapter 3 and 4 thus provide a firm theoretical basis to the understanding of the proposed global phase diagram of heavy fermion systems.

Chapter 5

Quantum Criticality from Sequential Destruction of SU(4) Spin-Orbital-coupled Kondo Effect

5.1 Introduction

In the previous chapters, we have considered the standard Kondo lattice model, in which the f-electrons form local dipolar moments and couple with the spin of a conduction electron band through the Kondo coupling. As the Kondo coupling dominates, the Kondo singlets are formed and the local moments are completely quenched. Recent experimental results in the cubic $Ce_3Pd_{20}Si_6$ provide an interesting extension of this paradigm to a multipolar Kondo lattice system, in which the f-electrons form local "levels" that possess much richer structure than the spin degree of freedom, and thus could allow for new types of phases and phase transitions.

In $Ce_3Pd_{20}Si_6$, every Ce^{3+} ion contributes one localized 4f electron. Because of the strong spin-orbit coupling, the spin and orbital degree of freedom of the 4f electron are coupled to each other, and thus are combined into a total angular momentum $J = 5/2$ state. Each local level of such $J = 5/2$ system has six-fold degeneracy, and hence supports not only dipole moment but also higher-order multipolar moments. Such six-fold degeneracy is split into a Γ_8 quartet and a Γ_7 doublet due to the crystal field effect[137]. The analysis of temperature dependent inelastic neutron scattering and entropy data also revealed that the Γ_8 quartet is the true ground state for the local levels[138]. As shown in Fig. 5.1, since the Γ_8 quartet has four-fold degeneracy,

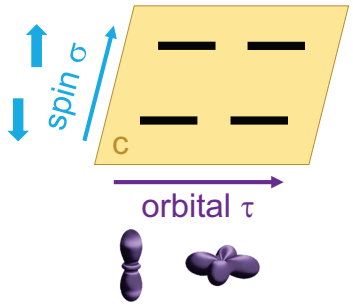

Figure 5.1 : Schematic diagrammatic representation of the 4-fold degeneracy of the Γ_8 ground state.

one can use the pseudo-spin $\vec{\sigma}$ and pseudo-orbital $\vec{\tau}$ to represent the ground state of local level as:

$$\begin{aligned}
|\tau_z = 1; \sigma_z = 1\rangle &= \sqrt{\frac{5}{6}}|J_z = \frac{5}{2}\rangle + \sqrt{\frac{1}{6}}|J_z = -\frac{3}{2}\rangle \\
|\tau_z = 1; \sigma_z = -1\rangle &= \sqrt{\frac{1}{6}}|J_z = \frac{5}{2}\rangle + \sqrt{\frac{5}{6}}|J_z = -\frac{3}{2}\rangle \\
|\tau_z = -1; \sigma_z = 1\rangle &= |J_z = \frac{1}{2}\rangle \\
|\tau_z = -1; \sigma_z = -1\rangle &= |J_z = -\frac{1}{2}\rangle
\end{aligned} \tag{5.1}$$

The Γ_8 systems comprise dipoles, quadrupoles, and octupoles, all of which are irreducible representations of the O_h group of the cubic lattice. Both dipolar (magnetic) and quadrupolar order (and likely even octupolar order) may arise via the RKKY interaction between the local multipolar moments[137]. At zero external field, neutron scattering experiments [139] show that the quadrupolar moments first order into an antiferroquadrupolar (AFQ) phase at $T_{\rm Q} \sim 0.4\,{\rm K}$, and with further decreasing temperature, the dipolar (magnetic) moments develop antiferromagnetic (AFM) order at $T_{\rm N} \sim 0.25\,{\rm K}$.

Once the external field is applied, the antiferromagnetic transition temperature is firstly suppressed and then goes to zero at some critical field B_N. Unlike AFM order,

AFQ order is sensitive to field orientations. Along [0 0 1] direction, the AFQ phase can be suppressed at a relatively small magnetic field [11]. The temperature-magnetic field phase diagram versus the applied magnetic field along this direction is shown in Fig. 5.2. We see that the AFM phase (phase III) is suppressed at $B_{\mathrm{N}} \sim 0.8\,\mathrm{T}$, whereas the AFQ phase (phase II) is suppressed at a slightly larger field $B_{\mathrm{Q}} \sim 2\,\mathrm{T}$. Both transitions have been found to be continuous from experiments [139, 11, 12], and thus there are two QCPs. The strange-metal behaviors associated with each QCP were also observed as shown in Fig. 5.3. More astonishing, across both B_{N} and B_{Q}, the measurements of magnetotransport revealed jumps of the Hall coefficient and magetoresistance in the zero-temperature, which implicates sudden reconstruction of Fermi surface for both QCPs. These results are summarized in the phase diagram Fig. 5.4[140, 13].

Since the concurrence of the Fermi surface reconstruction and the phase transition is a key signature of a Kondo destruction QCP, by combining all experimental data, we conclude that tuning the external field in the $Ce_3Pd_{20}Si_6$ can induce sequential Kondo destruction QCPs. Such consecutive Kondo destruction should be related to the multipolar nature of the local levels in $Ce_3Pd_{20}Si_6$. With the multipolar degree of freedom, in principle the Kondo entanglement between the local levels and the conduction electrons could break just partially at different stages. In the following, we are going to provide a firm theoretical ground for the notion of such sequential Kondo destruction in a multipolar heavy fermion system.

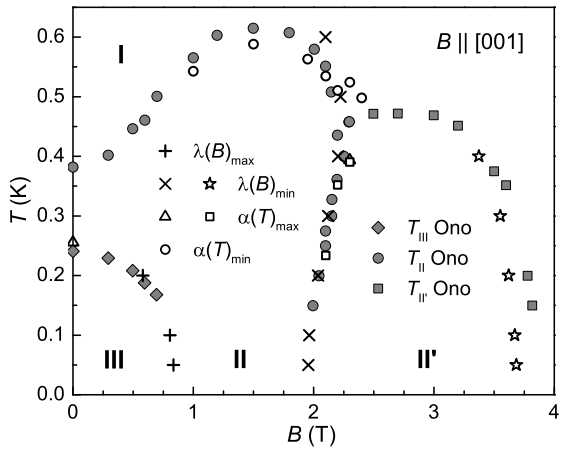

Figure 5.2 : Ordered phases in a temperature-magnetic field phase diagram for fields applied along [0 0 1], as identified from specific heat data by Ono et al. [11], and magnetostriction and thermal expansion data in Ref. [12]. The paramagnetic phase is denoted as phase I, the AFQ phase as phase II, and the AFM phase as phase III. The microscopic origin of phase II' remains to be identified.

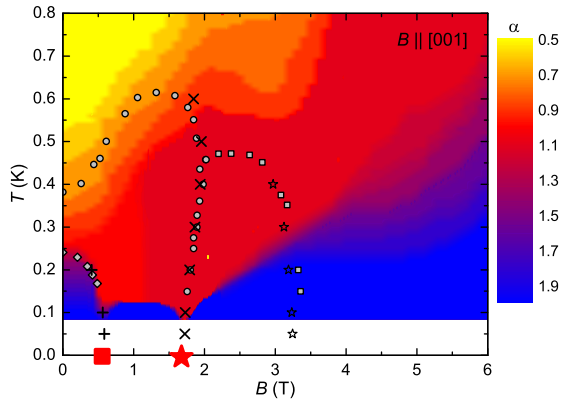

Figure 5.3 : Contour plot of the resistivity exponent a of $\rho = \rho_0 + A' \cdot T^a$ in the temperature-magnetic field phase diagram. The transition points at B_{N} and B_{Q} are marked by red square and red stars on the horizontal axis. From Ref. [13].

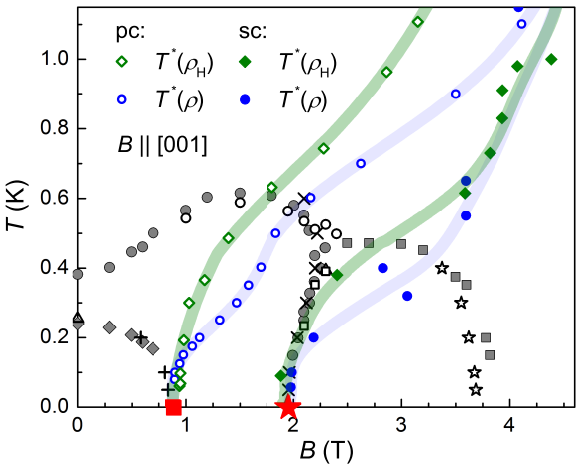

Figure 5.4 : Experimental temperature-magnetic field phase diagram, with T^* scales across which the Kondo entanglement in the spin and orbital channel breaks up at two consecutive QCPs, marked by the red square (at $B_{\rm N}$) and the red star (at $B_{\rm Q}$), respectively. From Ref. [13].

5.2 Model

To understand how multiple stages of Kondo destruction can arise without fine-tuning the parameters, we consider a multipolar Kondo lattice model that contains a lattice of local levels with a four-fold degeneracy which can be expressed in term of spin $\vec{\sigma}$ and orbital $\vec{\tau}$ operators:

$$H_{KL} = H_c + H_f + H_K. \tag{5.2}$$

The first part $H_c = \sum_{\boldsymbol{k}\sigma\tau} \epsilon_{\boldsymbol{k}\sigma\tau} c^\dagger_{\boldsymbol{k}\sigma\tau} c_{\boldsymbol{k}\sigma\tau}$ defines the kinetic energy of the conduction electrons, and the second part H_f describes the RKKY interaction among the Γ_8 local levels. For the purpose of convenience and demonstration, we choose H_f as the Ising type:

$$H_f = \sum_{ij} \left[I^\sigma_{ij} \sigma^z_i \sigma^z_j + I^\tau_{ij} \tau^z_i \tau^z_j + I^m_{ij} \left(\sigma^z_i \otimes \tau^z_i\right) \left(\sigma^z_j \otimes \tau^z_j\right) \right] \tag{5.3}$$

where, $\vec{\sigma}$, $\vec{\tau}$, and $\vec{\sigma} \otimes \vec{\tau}$ express the spin and orbital operators and their tensor product, respectively, and $I^\sigma_{ij}, I^\tau_{ij}, I^m_{ij}$ are the corresponding coupling constant. The Hamiltonian is essentially the Ising anisotropic version of the Kugel-Khomskii model.

The final part H_K is the Kondo coupling between the local levels and their conduction-electron counterparts:

$$H_K = \sum_i J_\sigma \vec{\sigma}_i \cdot \vec{\sigma}_{i,c} + \sum_i J_\tau \vec{\tau}_i \cdot \vec{\tau}_{i,c} + \sum_i 4 J_M \left(\vec{\sigma}_i \otimes \vec{\tau}_i\right) \cdot \left(\vec{\sigma}_{i,c} \otimes \vec{\tau}_{i,c}\right) \tag{5.4}$$

where the Kondo coupling J_κ with $\kappa = \sigma, \tau, M$, respectively, describe the interaction of the local levels $\vec{\sigma}$, $\vec{\tau}$, and $\vec{\sigma} \otimes \vec{\tau}$ with the conduction-electron counterparts.

The different components of the conduction electrons are defined as

$$\begin{aligned}\vec{\sigma}_{i,c} &= \frac{1}{2}\sum_{\sigma\sigma',\tau} c^{\dagger}_{i\sigma\tau}\vec{s}_{\sigma\sigma'}c_{i\sigma'\tau} \\ \vec{\tau}_{i,c} &= \frac{1}{2}\sum_{\sigma,\tau\tau'} c^{\dagger}_{i\sigma\tau}\vec{t}_{\tau\tau'}c_{i\sigma\tau'} \\ \vec{\sigma}_{i,c}\otimes\vec{\tau}_{i,c} &= \frac{1}{4}\sum_{\sigma\sigma'\tau\tau'} c^{\dagger}_{i\sigma\tau}\vec{s}_{\sigma\sigma'}\otimes\vec{t}_{\tau\tau'}c_{i\sigma'\tau'}\end{aligned} \tag{5.5}$$

where $\vec{s}_{\sigma\sigma'}$ and $\vec{t}_{\tau\tau'}$ are Pauli matrices in the spin and orbital subspaces, respectively, and $c^{\dagger}_{i\sigma\tau}$ creates a conduction electron at site i and with spin component σ and orbital component τ.

The Kondo Hamiltonian H_K (5.4) in general case respects the SU(2)$\otimes$SU(2) symmetry but breaks the SU(4) symmetry, which is restored only when $J_\sigma = J_\tau = J_M$. Without incorporating the RKKY interaction (5.3), it has been known that the RG flow trajectories of the Kondo Hamiltonian (5.4) flow toward the SU(4) strong Kondo coupling fixed point regardless of the initial parameters[141, 142]. In other words, there is no other phase and phase transition. In the following, we are going to demonstrate that with the RKKY interaction (5.3), the thing becomes dramatically different, and the sequential Kondo destruction phase transition is possible.

To do so, we use the scheme of extended dynamical mean field theory [143, 144], to map the multipolar Kondo lattice model $H_{\rm KL}$ into a spin-orbital coupled Bose-Fermi Kondo model(BFK) describing an single impurity model coupling with self-consistently determined fermionic and bosonic baths as illustrated in Fig. 5.5:

$$H_{BFK} = H_0 + H_K + H_{BK} \quad . \tag{5.6}$$

Here, $H_0 = H_{c0} + H_{B0}$ is the non-interacting part for the conduction electron and the bosonic baths, and is given by $H_{c0} = \sum_{\kappa=\sigma,\tau}\sum_q \epsilon_{\kappa,q}c^{\dagger}_{\kappa,q}c_{\kappa,q}$ and $H_{B0} = \sum_{\kappa=\sigma,\tau}\sum_q W_{\kappa,q}\phi^{\dagger}_{\kappa,q}\phi_{\kappa,q}$, respectively. H_K describes the local level at a single site

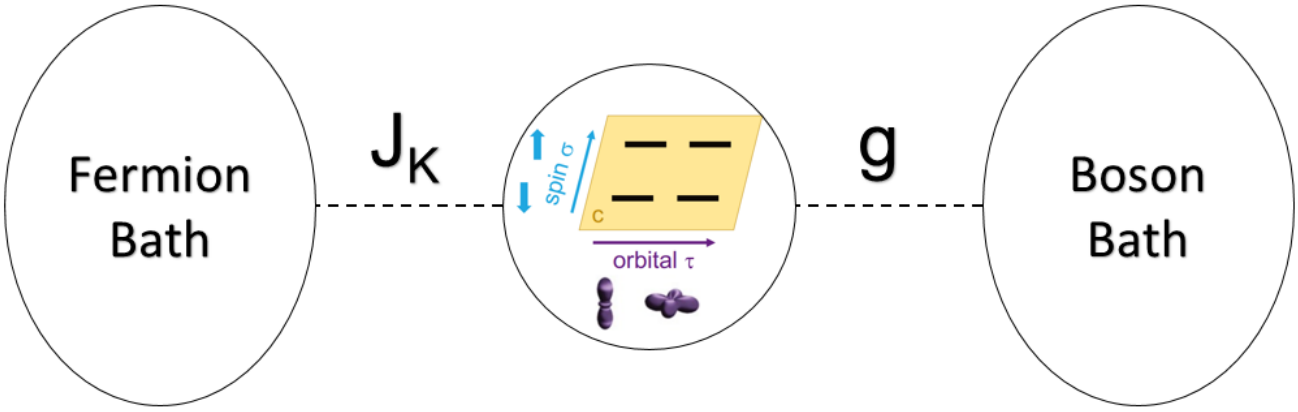

Figure 5.5 : schematic diagram of the spin-orbital coupled Bose-Fermi Kondo model (5.6).

0 being Kondo-coupled to the conduction electrons. In addition, H_{BK} describes the Bose-Kondo coupling between the local impurity and the bosonic baths, with coupling constants $g_{\kappa z}$. It is given by

$$H_{\rm BK} = g_{\sigma z}\sigma_z\phi_{\sigma z} + g_{\tau z}\tau_z\phi_{\tau z} \tag{5.7}$$

with $\phi_\kappa = \sum_q \left(\phi^\dagger_{\kappa,q} + \phi_{\kappa,-q}\right)$ for $\kappa = \sigma, \tau$. The sign of g_κ is immaterial and, for definiteness, each will be chosen to be positive. The coupling to bosonic baths reflects the magnetic fluctuation on site 0 induced by the inter-site RKKY interactions.

For the model (5.6) at $J_\sigma = J_\tau = J_M$, the phase diagram of the correspondent multipolar Bose-Fermi Anderson model, where the $H_{\rm K}$ is replaced by the hybridization of a localized two-orbital spin-1/2 f electron to theconduction electrons, has been studied through a numerical Quantum Monte Carlo(QMC) method[13]. The phase diagram is shown in Fig. 5.6, from which one can see that the sequential breakdown of Kondo entanglement is indeed generally possible.

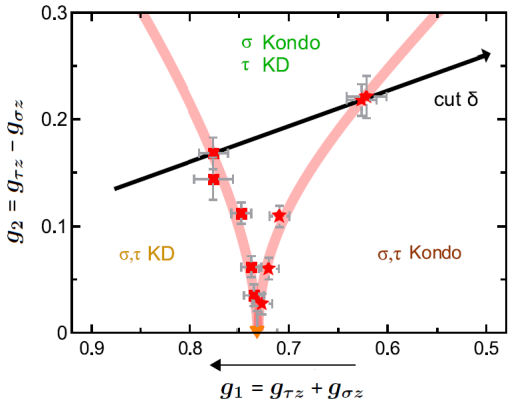

Figure 5.6 : Phase diagram (at $T = 0$) of the multipolar Bose Fermi Kondo model in the g_1–g_2 plane by a QMC study[13]. Here Kondo denotes Kondo-screened, and KD refer to Kondo-destroyed. Red squares and stars mark the spin and orbital Kondo destruction QCPs, respectively. The thick black arrow represents a generic trajectory in the parameter space. The orange triangle represents the special case $g_2 = 0$, where $g_{\tau z} = g_{\sigma z}$ and the two transitions occur simultaneously. Adapted from Ref. [13]

5.3 RG analysis and the generic phase diagram

Now the concept of the sequential Kondo destruction transition in a multipolar Kondo lattice model has been proven possible through a numerical QMC calculation. However, even the numerical results have their own value, any good combination of the analytical demonstrations is always necessary and can extend the understanding of the problem to a deeper level. Especially, the QMC calculation only scanned the whole phase diagram at the parameter case where the Kondo Hamiltonian H_K is SU(4) symmetric, and instead of solving the Bose-Fermi Kondo model, it solved a correspondent Bose-Fermi Anderson model. In this regard, in this section, we are going to perform an RG calculation of the spin-orbital coupled Bose-Fermi Kondo model (5.6):

$$H_{BFK} = H_0 + H_K + H_{BK} \tag{5.8}$$

Note that since the BFK model is a local impurity model, there is no site dependence. For the latter convenience, now we change the spin indices into Greek letters like α, and orbital indices into English letters such as i. One should not mix up with the site indices in the previous multipolar Kondo lattice model H_{KL} (5.2). Our next step is to use the pseudo-fermion representation for the spin and orbital operators of the local impurity:

$$\begin{aligned} \vec{\sigma} &= \frac{1}{2}\sum_{i,\alpha\beta} f^{\dagger}_{i\alpha}\vec{\sigma}_{\alpha\beta}f_{i\beta} \\ \vec{\tau} &= \frac{1}{2}\sum_{ij,\alpha} f^{\dagger}_{i\alpha}\vec{\tau}_{ij}f_{j\alpha} \\ \vec{\sigma}\otimes\vec{\tau} &= \frac{1}{4}\sum_{ij,\alpha\beta} f^{\dagger}_{i\alpha}\vec{\sigma}_{\alpha\beta}\otimes\vec{\tau}_{ij}f_{j\beta} \end{aligned} \tag{5.9}$$

and the constraint term $\sum_{i\alpha}\lambda f^{\dagger}_{i\alpha}f_{i\alpha}$ is also imposed into the action. As a result, the non-interacting part H_0 is:

$$H_0 = \sum_{i\alpha}\lambda f^{\dagger}_{i\alpha}f_{i\alpha} + \sum_{p,i\alpha}\epsilon_p c^{\dagger}_{p,i\alpha}c_{p,i\alpha} + \sum_q W_q\left(\vec{\phi}^{\dagger}_{\sigma,q}\cdot\vec{\phi}_{\sigma,q} + \vec{\phi}^{\dagger}_{\tau,q}\cdot\vec{\phi}_{\tau,q}\right) \tag{5.10}$$

In order to perform a controllable RG calculation, we also need to introduce a control parameter ϵ which is defined through the bosonic spectral function:

$$\sum_p\left[\delta\left(\omega-\omega_p\right)+\delta\left(\omega+\omega_p\right)\right] = \left(\frac{K_0^2}{\pi}\right)|\omega|^{\gamma}\operatorname{sgn}\omega \tag{5.11}$$

with

$$0 < \gamma \equiv 1-\epsilon < 1 \tag{5.12}$$

for $|\omega| < \Lambda$.

On the other hand, the coupling between the local impurity and the bosonic baths again is given by:

$$H_{BK} = g_{\sigma z}\sigma_z\phi_{\sigma z} + g_{\tau z}\tau_z\phi_{\tau z} \tag{5.13}$$

and the Kondo coupling at the SU(2)⊗SU(2) symmetric case is:

$$H_K = \sum_i J_\sigma \vec{\sigma}_i \cdot \vec{\sigma}_{i,c} + \sum_i J_\tau \vec{\tau}_i \cdot \vec{\tau}_{i,c} + \sum_i 4J_M \left(\vec{\sigma}_i \otimes \vec{\tau}_i\right) \cdot \left(\vec{\sigma}_{i,c} \otimes \vec{\tau}_{i,c}\right) \tag{5.14}$$

The spin and orbital Ising-type couplings in H_{BK} (5.13) actually cause some difficulties for the RG calculation. Firstly, unlike the Bose-Fermi Kondo model with an SU(2) spin rotational symmetry, in which the RG calculation can be done in a standard way[75], for the Ising case some extra effort is required[75]. One way to proceed is to use a so-called bosonization approach to map the BFK model (5.8) into a Colomb-gas type model, from which a controlled RG calculation is possible[75, 145].

Moreover, because the Ising couplings of H_{BK} (5.13) break not only the SU(4) symmetry but also the smaller SU(2)×SU(2) symmetry, in order to perform the RG calculation of the Kondo couplings in H_K which respect the SU(2)×SU(2) symmetry, one actually needs to reduce the symmetry of H_K, and thus inevitably need to introduce more Kondo couplings. It turns out that one needs to consider five types of Kondo couplings. Together with the spin and orbital Ising couplings $g_{\sigma z}$ and $g_{\tau z}$ of H_{BK} (5.13), the total number of coupling constants is seven.

We leave the full RG calculation and the detailed analysis in appendix C. Instead, here we summarize the results directly, and then illustrate how these results come about. The phase diagram based on the RG analysis is summarized in Fig 5.7, where the spin and orbital Kondo-destroyed(KD) phase can transit to the spin or orbital Kondo-screened(KS) phase, or to the SU(4) KS phase.

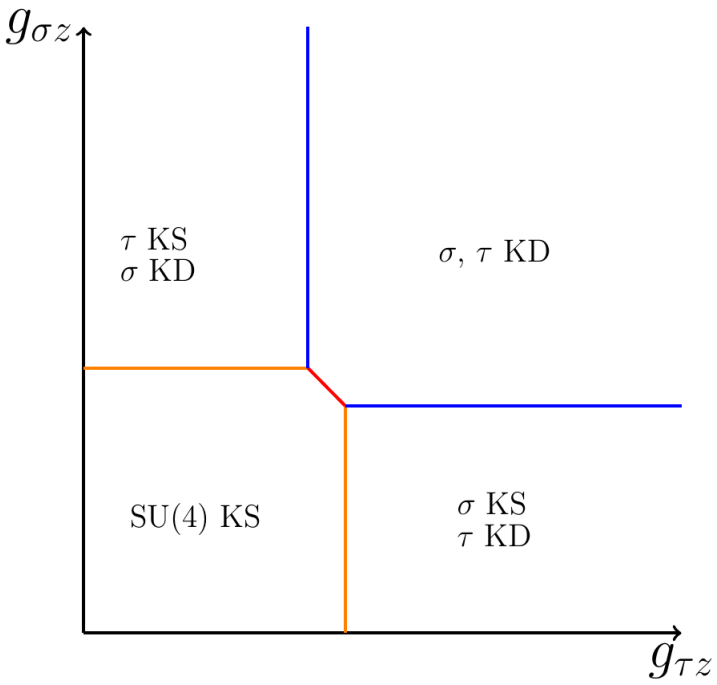

Figure 5.7 : The generic phase diagram based on the RG analysis, where KD and KS refer to Kondo-destroyed and Kondo-screened phases, respectively.

5.3.1 Transition to the SU(4) Kondo-screened phase

Now we briefly illustrate the transition from the spin and orbital KD phase to the SU(4) KS phase. We scan the RG flow structure by taking $g_{\sigma z} = g_{\tau z} = g$, which corresponds to the trajectory denoted as the dashed arrow in Fig. 5.8*.

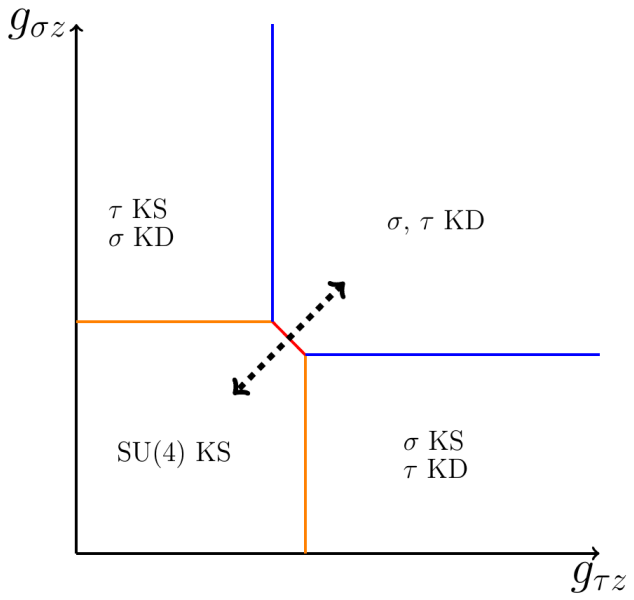

Figure 5.8 : Phase diagram trajectory of $g_{\sigma z} = g_{\tau z} = g$ is denoted by the dashed arrow.

As we have mentioned, generally the total number of coupling constants is seven. However, under the trajectory $g_{\sigma z} = g_{\tau z} = g$, some of the coupling constants are irrelevant, or can be combined due to the symmetry constraint, and thus the numbers of relevant RG equations (the β functions) can be substantially reduced. We leave

*One can verify from the RG equations (the β functions) that any small deviation from this trajectory actually is irrelevant in the RG sense.

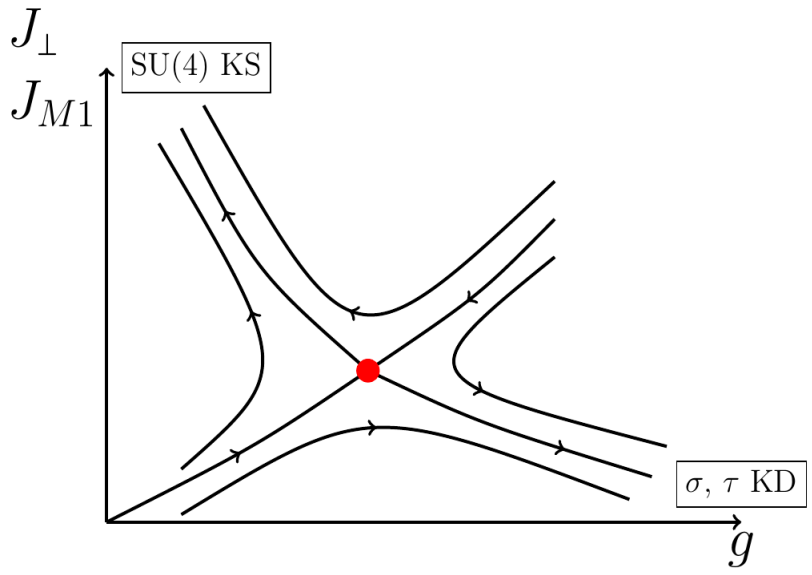

Figure 5.9 : RG flow diagram of the reduced β functions (5.15).

the details in appendix C.2.2, and only show the final reduced β functions:

$$\begin{aligned} \frac{dy_1}{dl} &= (1-2M)\, y_1 + 2y^2 \\ \frac{dy}{dl} &= (1-M)\, y + 2y_1 y \\ \frac{dM}{dl} &= \left(\epsilon - 4y_1^2 - 4y^2\right) M \end{aligned} \tag{5.15}$$

where $y = J_{\sigma\perp} = J_{\tau\perp}$ flips either spin or orbital indices, $M \propto g_{\sigma z}^2 = g_{\tau z}^2 = g^2$, and $y = J_{M1}$ is the part of the Kondo coupling J_M that flips both the spin and orbital indices. Note that we can set $J_{\sigma\perp} = J_{\tau\perp}$ since we choose to scan phase diagram in a path that preserves the symmetry $\sigma \leftrightarrow \tau$.

By these reduced β functions (5.15), one identifies a critical point $(y_1^*, y^*, M^*) = \left(\frac{\sqrt{\epsilon}}{2}, 0, \frac{1}{2}\right)$ separating the spin and orbital KD phase $(y_1 \to 0, y \to 0, M \to \infty)$ from the SU(4) KS phase $(y_1 \to \infty, y \to \infty, M \to 0)$. The RG flow structure of the reduced β functions (5.15) is plotted in Fig. 5.9. Consequently, we establish the transition between the spin and orbital KD phase and the SU(4) KS phase in the phase diagram

Fig. 5.8.

5.3.2 Transition to spin or orbital Kondo-screened phase

Our next step is to illustrate the transition between the spin and orbital KD phase and the σ or τ KS phase. We scan the RG flow structure by either taking $g_{\sigma z} \to \infty$ and varying the $g_{\tau z}$, or taking $g_{\tau z} \to \infty$ and varying $g_{\sigma z}$. The corresponding trajectories in phase diagram are denoted as the dashed arrow lines in Fig. 5.10[†].

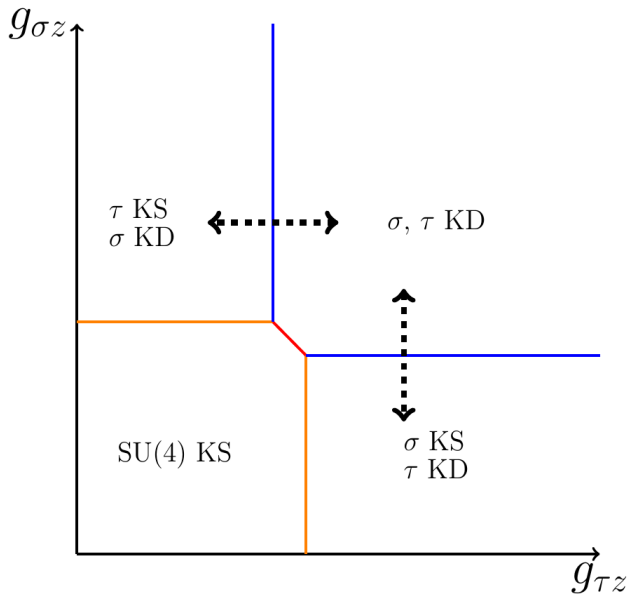

Figure 5.10 : Phase diagram trajectory of varying $g_{\tau z}(g_{\sigma z})$, and taking $g_{\sigma z}$ $(g_{\tau z}) \to \infty$, is denoted as either of the two dashed arrows.

Without loss of generality, here we choose to take $g_{\sigma z} \to \infty$. In this case, the final

[†]Again, from the β functions, one can check that any small deviation from these trajectories actually is also irrelevant in the RG sense.

reduced β functions are:

$$\begin{aligned} \frac{dy_2}{dl} &= (1 - M^\sigma)\, y_2 \\ \frac{dM^\sigma}{dl} &= \left(\epsilon - 4y_2^2\right) M^\sigma \end{aligned} \tag{5.16}$$

where $y_2 = J_{\sigma\perp}$ flips only the orbital indices, and $M^\sigma \propto g_{\sigma z}^2$. Again, we leave the derivation details in appendix C.2.3.

The RG flow of the reduced β functions (5.16) is plotted in Fig. 5.11. One can find a critical point $(y_2^*, M^{\sigma *}) = \left(\frac{\sqrt{\epsilon}}{2}, 1\right)$ separating the spin KS phase ($y_2 \to \infty, M^\sigma \to 0$) from the spin and orbital KD phase ($y_2 \to 0, M^\sigma \to \infty$). Therefore, based on this RG structure, we establish the transition between the spin and orbital KD phase and the spin KS phase. For the other trajectory, the analysis is precisely parallel, and the transition between the spin and orbital KD phase and the orbital KS phase can likewise be established.

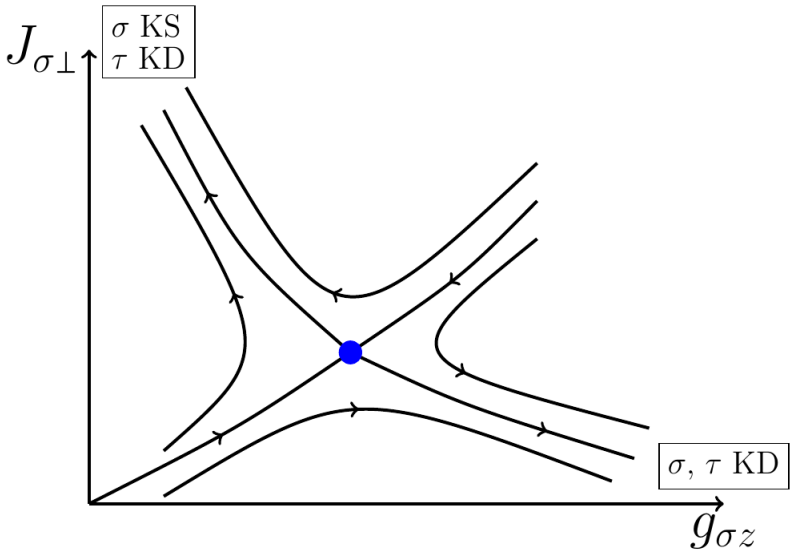

Figure 5.11 : RG flow diagram of the reduced β functions (5.16) on the $J_{\sigma\perp} - g_{\sigma z}$ plane.

5.4 Conclusion: Phase diagram and the sequential Kondo destruction

Up to now, we have shown that a spin and orbital KD phase can transit into different types of strong Kondo coupling fixed points corresponding to the spin, orbital, and SU(4) KS phases without fine-tuning the parameters. Consequently, there must be a phase transition between the spin or orbital KS phase and the SU(4) KS phase, as indicated in Fig. 5.12. The whole phase diagram in Fig. 5.7, then, is established.

For this phase diagram, the sequential Kondo destruction is robust, in the sense that there is no need to fine-tune the parameters in order to reach the quantum phase transitions that involve two-stages of Kondo destruction. These results provide a firm theoretical basis for the earlier numerical QMC results in a related Kondo model, and to the understanding of the quantum criticality in spin-orbital-coupled heavy fermion systems. Furthur comparison of the phase diagram based on our RG analysis, with those from the earlier numerical QMC result[13] and from the experimental measurements in the heavy fermion metal $Ce_3Pd_{20}Si_6$[13] is summarized in Fig. 5.13.

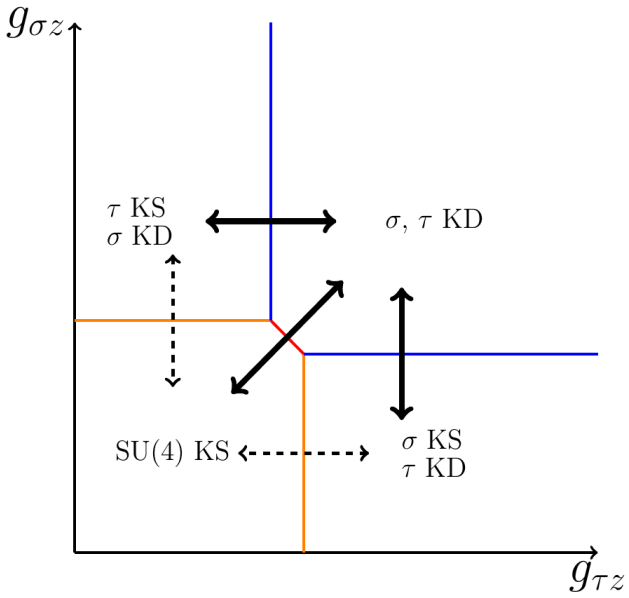

Figure 5.12 : The generic phase diagram based on our RG analysis. Solid arrows denote the phase transitions that we have established from our analysis. Since the spin and orbital KD phase can transit to the three distinct KS phases, there must be phase transitions between these KS phases, which are denoted by the dashed arrows.

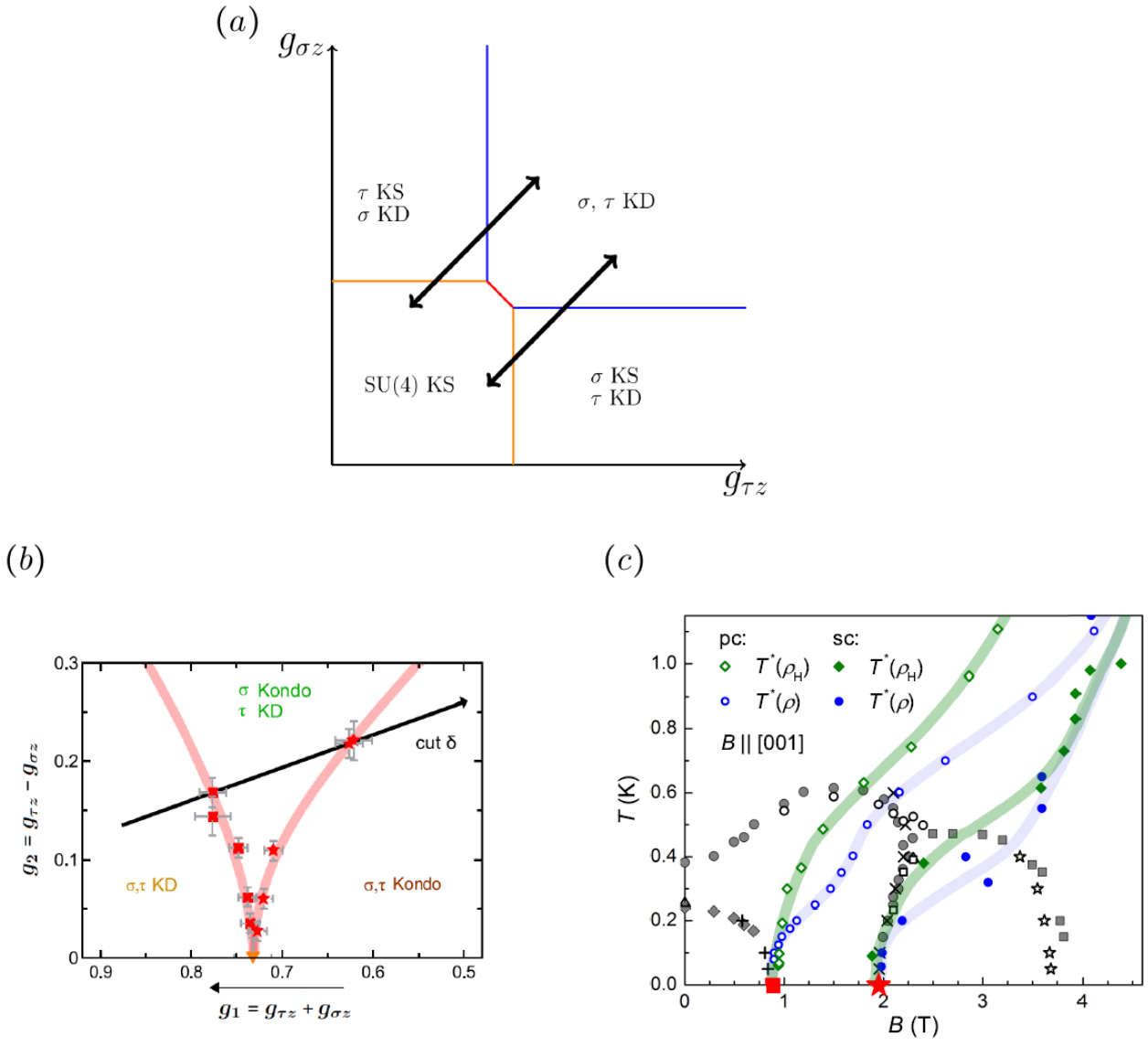

Figure 5.13 : Comparison of (a) phase diagram based on our RG analysis with (b) earlier numerical QMC result in Fig 5.6, and (c) the experimental phase diagram of $Ce_3Pd_{20}Si_6$ in Fig. 5.4. The solid arrows in (a) correspond to trajectories for the quantum phase transitions of the sequential Kondo destruction.

Chapter 6

Quantum critical nematic fluctuations and spin excitation anisotropy in iron pnictides

6.1 Introduction

As described earlier, quantum criticality also operates in other classes of strongly correlated electron systems. Iron-based superconductors have presented many intriguing and often puzzling properties [78, 79, 146, 147, 29, 148]. Among these is the onset of the tetragonal-to-orthorhombic structural phase transition at a temperature just above or at the antiferromagnetic (AF) phase transition [87]. When they are split, the region between the two transitions is called a nematic phase, where the C_4 tetragonal symmetry is broken while the $O(3)$ spin rotational symmetry is preserved. It has been well established that the nematic transition is driven by electron correlations, with B_{1g} anisotropies in electronic, orbital and magnetic properties [149, 150, 151]. Several channels are entwined in the nematic correlations, including spin [80, 85, 86, 152], electronic [153, 154] and orbital[155, 156] degrees of freedom.

One way to make progress is to consider the quantum critical regime, where the criticality singularities can be isolated from regular contributions. This facilitates the study of the relationship between the responses in the nematic and other channels. Our strategy in this paper is to assume that the magnetic fluctuations drive nematic correlations, establish a precise relationship between the singular responses in the magnetic and nematic sectors, and uses this relationship to assess the underlying

assumption and determine the critical properties. The parent ground state of the iron-pnictide superconductors is an AF state with the ordering wave vector $\vec{Q}_1 = (\pi, 0)$ or $\vec{Q}_2 = (0, \pi)$. Their spatial patterns are shown in Fig. 6.1(a) and 6.1(b). The AF state breaks not only the usual $O(3)$ spin rotational symmetry, but also a Z_2 symmetry between the $\vec{Q}_1$ and $\vec{Q}_2$ magnetic state. In iron pnictides, the bad-metal behavior [81, 8] motivated a theoretical proposal for the electronic excitations into coherent and incoherent parts. The tuning of the coherent electron weight was proposed to give rise to concurrent quantum criticality in both the $(\pi, 0)$ AF and Ising-nematic channels* [80]. The existence of quantum criticality has been most extensively evidenced by experiments in $BaFe_2As_2$ with P-for-As doping to the regime of optimal superconductivity [89, 159, 92, 90, 160].

A defining characteristic of quantum criticality is the inherent mixing of statics and dynamics. Singular magnetic responses in the quantum critical regime have been observed through dynamical measurements at both the optimally P-for-As- and Ni-for-Fe-doped $BaFe_2As_2$ [161, 14]. Singular nematic responses in the quantum critical regime have also been observed over a variety of optimally doped iron pnictides [91], albeit in DC measurements. The comparison already demonstrates the concurrent nature of the quantum criticality in the magnetic and nematic channels †. However,

*In the theoretical analysis, the magnetic and nematic quantum phase transitions are concurrent and very weakly first-order, with a jump of both order parameters that are nonzero but very small. The first order nature is driven by a relevant coupling; its weakness is dictated by the marginal nature of this coupling [80, 10], and has been confirmed in experiments [157]. The weakness of the first order transition dictates that there is an extended dynamical range over which criticality operates [158]

†While this is certainly true over an extended range of temperatures, we caution that quantum criticality may not extend all the way to zero temperature, and this was already indicated in the

to elucidate the relationship between the singular nematic and magnetic responses, it would be desirable to determine the dynamical nematic susceptibility in the quantum critical regime. In general, the low-energy dynamical nematic susceptibility in the quantum critical regime is not readily accessible experimentally.

In this work, we elucidate the relation between the singular dynamical magnetic and nematic responses by exploiting the relationship between the dynamical nematic susceptibility and spin excitation anisotropy. The latter, defined as the difference of the dynamical spin susceptibilities at $\vec{Q}_1 = (\pi, 0)$ and $\vec{Q}_2 = (0, \pi)$, under a uniaxial strain that breaks the C_4 symmetry in B_{1g} channel, has been measured by inelastic neutron scattering experiments in the optimally doped iron pnictides [14, 151, 163]. We analyze the singular part of the dynamical responses in both the O(3) AF and Z_2 Ising-nematic sectors. Within an effective Ginzburg-Landau theory involving both the AF and nematic degrees of freedom, we establish a general identity [Eq. (6.6)] among the spin excitation anisotropy, the dynamical magnetic susceptibility, and the nematic susceptibility. Based on a scaling analysis, we further show how this identity can be used to explore the properties of a quantum critical point (QCP), where both the magnetic and nematic channels are concurrently critical. Through the scaling procedure, we extract the dynamical nematic susceptibility from the spin excitation anisotropy, and also determine the dynamic exponent z and the scaling dimension of the nematic order parameter d_Δ. The procedure is illustrated in the context of the inelastic neutron scattering results for the optimally Ni-doped $BaFe_2Si_2$ under an external stress [14], which are summarized in Figs. 6.2(a) and 6.2(b).

P-doped $BaFe_2As_2$ [90, 160]. In addition, further studies are needed to determine whether he zero-temperature phase transitions are concurrent in all the doped iron pnictides [162].

6.2 Effective model

We start from an effective field theory for the magnetism of iron pnictides [80, 9]

$$\begin{aligned} S_0 &= S_2 + S_4 \\ S_2 &= \sum_{q=\vec{q},i\omega_n} \left\{ G_0^{-1}(q) \left(|\vec{m}_A(q)|^2 + |\vec{m}_B(q)|^2 \right) \right. \\ S_4 &= \int_0^\beta d\tau \int d^2x \left[u_1 \left(\vec{m}_A^2 + \vec{m}_B^2 \right)^2 - u_I \left(\vec{m}_A \cdot \vec{m}_B \right)^2 \right] \end{aligned} \tag{6.1}$$

where $\vec{m}_A$ and $\vec{m}_B$ are the Neel order parameter fields on the sublattices A and B, respectively, and $G_0^{-1}(\vec{q}, i\omega_n) = r + \omega_n^2 + c\vec{q}^2 + \gamma|\omega_n|$ with the mass term r and Landau damping term $\gamma|\omega_n|$ resulting from the coherent electronic excitations [80]. For convenience, we neglect the interaction $-u_2 \left(\vec{m}_A^2 - \vec{m}_B^2 \right)^2$ and the spatial anisotropy term $v \left(q_x^2 - q_y^2 \right) \vec{m}_A(q) \cdot \vec{m}_B(-q)$, which do not affect our scaling analysis.

We consider the problem in the presence of an external uniaxial stress, and focus on the effect of the induced strain in the B_{1g} channel, which couples linearly to the quantity $\vec{m}_A \cdot \vec{m}_B$. Absorbing this coupling into a Hubbard-Stratonovich transformation, it leads to a coupling $S_{\lambda,\Delta} = \lambda \int_0^\beta d\tau \int d^2x \Delta$ after integrating the strain degree of freedom, where λ is the strength of the external stress. Leaving details to the Supplementary Material (SM) (where additional terms that do not affect our scaling analysis are also described), we arrive at the following effective action:

$$\begin{aligned} S &= \tilde{S}_2 + S_3 + \ldots + S_{\lambda,\Delta} \\ \tilde{S}_2 &= \sum_{q=\vec{q},i\omega_n} \left\{ \chi_0^{-1}(q) \left(|\vec{m}_A(q)|^2 + |\vec{m}_B(q)|^2 \right) \right. \\ &\left. + \Delta(q) \chi_\Delta^{-1}(q) \Delta(-q) \right\} \\ S_3 &= \int_0^\beta d\tau \int d^2x 2\Delta \vec{m}_A \cdot \vec{m}_B \\ S_{\lambda,\Delta} &= \lambda \int_0^\beta d\tau \int d^2x \Delta \end{aligned} \tag{6.2}$$

where we have absorbed the mass term into the field conjugate to $\vec{m}_A^2 + \vec{m}_B^2$ (see SM) so that now $\chi_0^{-1}(\vec{q}, i\omega_n) = G_0^{-1}(\vec{q}, i\omega_n) - r = \omega_n^2 + c\vec{q}^2 + \gamma|\omega|$, and $\chi_\Delta^{-1}(\vec{q}, i\omega_n)$ is the *bare* magnetic and nematic propagator, respectively. The ellipsis denotes the terms that are not essential to our scaling analysis (see SM).

The spin excitation anisotropy $\chi_d(\omega)$ and the dynamical magnetic susceptibility $\chi_s(\omega)$ are defined as the difference and summation of the dynamical spin susceptibility $\chi(\vec{q}, \omega)$ between the two ordering wave vector $\vec{Q}_1 = (\pi, 0)$ and $\vec{Q}_2 = (0, \pi)$, respectively:

$$\chi_s(\omega) \equiv \chi\left(\vec{Q}_1, \omega\right) + \chi\left(\vec{Q}_2, \omega\right) \tag{6.3}$$

$$\chi_d(\omega) \equiv \chi\left(\vec{Q}_1, \omega\right) - \chi\left(\vec{Q}_2, \omega\right) \tag{6.4}$$

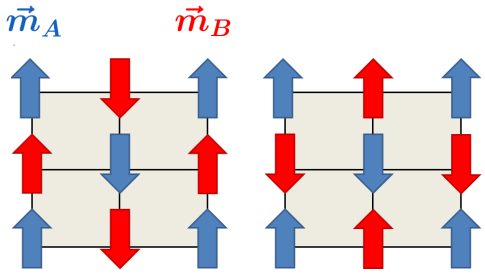

(a) $\vec{Q}_1 = (\pi, 0)$ (b) $\vec{Q}_2 = (0, \pi)$

Figure 6.1 : (a) The spin configurations of the ground state of the parent iron-based superconductors with ordering wave vector $\vec{Q}_1 = (\pi, 0)$ or (b) $\vec{Q}_2 = (0, \pi)$. The blue and red arrows denote the spins forming the staggered magnetizations on the sublattices A and B, respectively.

6.3 Connecting the spin excitation anisotropy to nematic susceptibility

On symmetry grounds, the spin excitation anisotropy $\chi_d(\omega)$ should be related to the Ising-nematic fluctuations, since it measures the degree of the asymmetry of the magnetic fluctuations between the two wave vectors $\vec{Q}_1$ and $\vec{Q}_2$. However, the precise

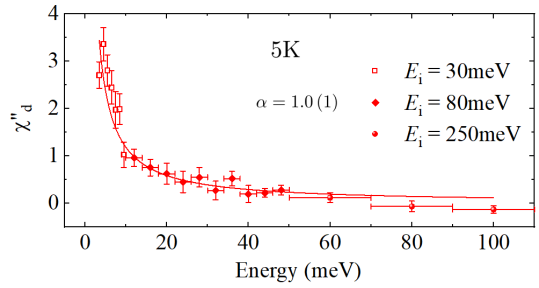

(a)

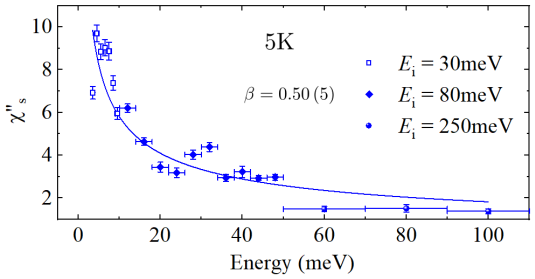

(b)

Figure 6.2 : The energy dependences of (a) the imaginary part of the spin excitation anisotropy $\chi''_d = \chi''\left(\vec{Q}_1\right) - \chi''\left(\vec{Q}_2\right)$ vs. energy and (b) the dynamical magnetic susceptibility $\chi''_s = \chi''\left(\vec{Q}_1\right) + \chi''\left(\vec{Q}_2\right)$ in $BaFe_{2-x}Ni_xAs_2$ measured by inelastic neutron scattering experiments at $T = 5K < T_S$[14] near the optimal doping $x = x_c \approx 0.1$; the former(latter) is fit in the power law form $E^{-\alpha}(E^{-\beta})$ with the exponent $\alpha \cong 1.0$ ($\beta \cong 0.5$).

relation has not been considered before. A detailed analysis, given in SM, shows that:

$$\chi_s(\omega) \equiv \chi\left(\vec{Q}_1, \omega\right) + \chi\left(\vec{Q}_2, \omega\right) = \overline{\chi}_m(0, \omega) + O\left(\lambda^2\right) \tag{6.5}$$

and

$$\begin{aligned} \chi_d(\omega) &\equiv \chi\left(\vec{Q}_1, \omega\right) - \chi\left(\vec{Q}_2, \omega\right) \\ &= \lambda \overline{V}(0, \omega)\, \overline{\chi}_m^2(0, \omega)\, \overline{\chi}_\Delta(0, 0) + O\left(\lambda^2\right) \end{aligned} \tag{6.6}$$

where $\overline{\chi}_m(q, \omega) \equiv \overline{\chi}_{m_A}(q, \omega) = \overline{\chi}_{m_B}(q, \omega)$ is the magnetic propagator, $\overline{\chi}_\Delta(q, \omega)$ is the nematic propagator, and $\overline{V}$ is the irreducible vertex function involving two external magnetic order parameter fields $\vec{m}_A$ and $\vec{m}_B$ and one nematic order parameter field Δ. For both of the Eq.(6.5) and Eq.(6.6), we use the symmetry $\vec{m}_A \leftrightarrow \vec{m}_B$ respected by the action (6.2), as discuss in the SM.

The identity, Eq. (6.6), will play a central role in the following analysis. The diagrammatic representation of this identity is shown in Fig. 6.3.

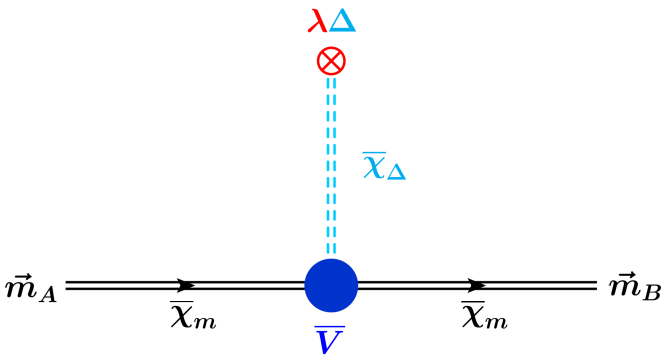

Figure 6.3 : The diagrammatic representation of the identity Eq. (6.6). The double black line and double cyan dashed line denote the renormalized magnetic propagator $\overline{\chi}_m$ and nematic propagator $\overline{\chi}_\Delta$, respectively. The blue circle is the vertex function $\overline{V}$, and the red cross small circle is the external C_4 symmetry breaking potential.

6.4 Scaling analysis

We now apply the identity, Eq. (6.6), to extract the nematic susceptibility from the spin excitation anisotropy. Our focus is on the singular parts of these quantities in the quantum critical regime.

Due to the scale invariance in the quantum critical regime, the irreducible two-point correlation function $\overline{\chi}_m(0,\omega)$ and the irreducible vertex function $\overline{V}(0,\omega)$ should obey a power law form with specific exponents Therefore, we expect the spin excitation anisotropy $\chi_d(\omega)$ to also obey the power law form with a specific exponent.

To derive these exponents, we carry out a scaling analysis of the irreducible vertex functions, using the generating functional $\Gamma(m,\Delta)$ [164, 165]:

$$\Gamma(m,\Delta)=\sum_{n_m,n_\Delta}\frac{1}{n_m!n_\Delta!}\int_{\{q\},\{p\}}\int_{\{\omega\},\{\nu\}}\times\left(\prod_{i=1}^{n_m}m_i\prod_{j=1}^{n_\Delta}\Delta_j\right)\Gamma^{n_m,n_\Delta}(\{q\},\{p\},\{\omega\},\{\nu\}) \tag{6.7}$$

where we define $\int_{\{q\},\{p\}}\equiv\int\prod_{i=1}^{n_m}d^Dq_i\prod_{j=1}^{n_\Delta}d^Dp_j\delta\left(\sum_i^{n_m}q_i+\sum_j^{n_\Delta}p_j\right)$ and $\int_{\{\omega\},\{\nu\}}\equiv\int\prod_{i=1}^{n_m}d\omega_i\prod_{j=1}^{n_\Delta}d\nu_j\delta\left(\sum_i^{n_m}\omega_i+\sum_j^{n_\Delta}\nu_j\right)$, with D being the spatial dimensionality. In addition, we have introduced Γ^{n_m,n_Δ} to represent an irreducible vertex function with n_m and n_Δ external magnetic and nematic order parameter fields, respectively.

In the quantum critical regime, under the rescaling $q\to e^{-l}q$, $\omega\to e^{-zl}\omega$, the magnetic and nematic order parameter fields transform according to $m\to e^{-d_ml}m$, $\Delta\to e^{-d_\Delta l}\Delta$, where d_m and d_Δ are their respective scaling dimensions. Since $\Gamma(m,\Delta)$ is a dimensionless quantity, the irreducible vertex function Γ^{n_m,n_Δ} must satisfy [165, 166, 126]:

$$\begin{gathered}\Gamma^{n_m,n_\Delta}(q,\omega)=\\ e^{-d_\Gamma l}\Gamma^{n_m,n_\Delta}\left(qe^{-l},\omega e^{-zl}\right)\end{gathered} \tag{6.8}$$

where $d_\Gamma=n_m(d_m+D+z)+n_\Delta(d_\Delta+D+z)-(D+z)$, and z is the dynamic

exponent[‡].

From the action, Eq. 6.2, it is straightforward to specify the scaling dimension [§] of the magnetic order parameter $\vec{m}$:

$$d_m = -\frac{D+z+2-\eta}{2}. \tag{6.9}$$

Because η, the anomalous dimension, is typically small, we will carry out our analysis assuming $\eta \cong 0$; what happens when $\eta \neq 0$ is shown in the SM. It then follows from Eq. (6.8) that:

$$\begin{aligned} &\Gamma^{n_m,n_\Delta}(q,\omega) = \\ &e^{\left[n_m - n_\Delta(d_\Delta+D+z)-(D+z)\left(\frac{n_m}{2}-1\right)\right]l}\Gamma^{n_m,n_\Delta}\left(qe^{-l},\omega e^{-zl}\right) \end{aligned} \tag{6.10}$$

The magnetic propagator is determined by a two-point irreducible vertex function:

$$\begin{aligned} &\overline{\chi}_m^{-1}(q,\omega) \equiv \Gamma^{n_m=2,n_\Delta=0}(q,\omega) = e^{2(l)}\overline{\chi}_m^{-1}\left(qe^{-l},\omega e^{-zl}\right) \\ &= q^2\overline{\chi}_m^{-1}\left(1,\omega q^{-z}\right) \end{aligned} \tag{6.11}$$

where in the last step we choose l such that $qe^{-l} = 1$. This, in turn, implies:

$$\overline{\chi}_m(0,\omega) = \chi_s(\omega) \sim \omega^{-\frac{2}{z}} \tag{6.12}$$

The function $\overline{V}$ appearing in Eq. (6.6) (and Fig. 6.3) is a three-point irreducible vertex function. The scaling procedure leads to:

$$\begin{aligned} &\overline{V}(q,\omega) \equiv \Gamma^{n_m=2,n_\Delta=1}(q,\omega) \\ &= e^{[2-d_\Delta-(D+z)]l}\overline{V}\left(qe^{-l},\omega e^{-zl}\right) \\ &= q^{(2-d_\Delta-(D+z))}\overline{V}\left(1,\omega q^{-z}\right) \end{aligned} \tag{6.13}$$

[‡]Note that in Eqs. (Here, the scaling analysis is carried out in the quantum critical regime.

[§]Note that in Eqs. (6.8) and (6.9), we choose to count the dimension from the momentum space action.

In turn, this gives rise to the following frequency dependence:

$$\overline{V}\left(0,\omega\right) \sim \omega^{\frac{2-d_{\Delta}-(D+z)}{z}} \tag{6.14}$$

Collecting all these, we can now determine from Eq. (6.6) the scaling form for the spin excitation anisotropy:

$$\chi_{d}\left(\omega\right) \sim \omega^{\frac{-2-d_{\Delta}-(D+z)}{z}} \tag{6.15}$$

Conversely, by measuring the singular parts in the energy dependence of the spin excitation anisotropy $\chi_{d}\left(\omega\right)$ and dynamical magnetic susceptibility $\chi_{s}\left(\omega\right)$ in the quantum critical regime, we can determine the dynamical exponent z and the scaling dimension of the nematic order parameter d_{Δ} through the following relations:

$$\begin{aligned} \frac{-2}{z} &= \frac{\partial \ln \chi_{s}\left(\omega\right)}{\partial \ln \omega} \\ \frac{-d_{\Delta}-(D+z)-2}{z} &= \frac{\partial \ln \chi_{d}\left(\omega\right)}{\partial \ln \omega} \end{aligned} \tag{6.16}$$

The above determine d_{Δ} and z for a given spatial dimensionality D. In turn, we can determine the singular *dynamical* properties of the nematic degree of freedom, which we now turn to.

6.4.1 Dynamical nematic susceptibility

We now turn to the analysis of the dynamical nematic susceptibility, $\overline{\chi}_{\Delta}\left(0,\omega\right)$, a task that seems impossible given that the identity Eq. (6.6) involves only the static nematic susceptibility $\overline{\chi}_{\Delta}\left(0,0\right)$. The key point is that the irreducible vertex function $\overline{V}\left(0,\omega\right)$ couples the nematic and magnetic order parameter fields, and captures the critical singularity in the *dynamical* nematic correlations.

To make this point clear, we note that, according to the scaling analysis, the critical part of the dynamical nematic susceptibility $\overline{\chi}_{\Delta}\left(q,\omega\right)$ obeys the following

form:

$$\begin{aligned}\overline{\chi}_{\Delta}^{-1}(q,\omega) &\equiv \Gamma^{n_m=0,n_\Delta=2}(\vec{q},\omega)\\ &= e^{-[2d_\Delta+(D+z)]l}\overline{\chi}_{\Delta}^{-1}\left(qe^{-l},\omega e^{-zl}\right)\\ &= q^{-(2d_\Delta+(D+z))}\overline{\chi}_{\Delta}^{-1}\left(1,\omega q^{-z}\right)\end{aligned} \tag{6.17}$$

This, in turn, implies the following result for the dynamical nematic susceptibility $\overline{\chi}_{\Delta}(0,\omega)$:

$$\overline{\chi}_{\Delta}(0,\omega) \sim \omega^{\frac{(2d_\Delta+(D+z))}{z}} \tag{6.18}$$

6.4.2 The case of quantum criticality in $BaFe_2As_2$ with optimal Ni-doping

In the Ni-doped $BaFe_{2-x}Ni_xAs_2$, the singular energy dependences of the spin excitation anisotropy and magnetic susceptibility were observed near the optimal doping $x = x_c \approx 0.1$ by inelastic neutron scattering experiments [14] as shown in the Figs. 6.2(a) and 6.2(b) (where $T = 5K < T_S$ only affects the results at the lowest measured frequencies). The experimental data suggest that the spin excitation anisotropy $\chi_d(\omega)$ and dynamical magnetic susceptibility $\chi_s(\omega)$ are best-fitted in power laws with different exponents α and β, respectively:

$$\begin{aligned}\chi_d(\omega) &\sim \omega^{-\alpha}\\ \chi_s(\omega) &= \overline{\chi}_m(0,\omega) \sim \omega^{-\beta}\end{aligned} \tag{6.19}$$

with $\alpha \cong 1.0$ and $\beta \cong 0.50$.

While there can be different physical reasons that could alter the values of the exponents α and β, it is intriguing that

$$\alpha \cong 2\beta\,. \tag{6.20}$$

We demonstrate that the identity Eq. (6.6) we established earlier serves as a natural way to explore the physics behind the relation (6.20).

By the identity Eq. (6.6), we see that the relation (6.20) implies:

$$\overline{V}\left(0,\omega\right) \sim \frac{\chi_d\left(\omega\right)}{\overline{\chi}_m^2\left(0,\omega\right)} \sim \omega^0 \,. \tag{6.21}$$

Following the scaling analysis of the irreducible vertex function, Eq. (6.14), we conclude that these power law forms are associated with an underlying QCP at which the scaling dimension of the nematic order parameter d_Δ is:

$$d_\Delta = 2 - D - z \tag{6.22}$$

In other words, the relation (6.20) implies a specific link between the the scaling dimension of the nematic order parameter d_Δ and dynamic exponent z.

This relation contains non-trivial information about the nematic degree of freedom. To see this further, consider a general form of the nematic propagator suitable for the quantum critical regime:

$$\overline{\chi}_\Delta^{-1}\left(q,\omega\right) = b_1 q^n + b_2 \frac{|\omega|}{q^a} \tag{6.23}$$

For this propagator, we must have:

$$z = n + a \tag{6.24}$$

and

$$d_\Delta = -\frac{D+z+n}{2} = -\frac{D+2n+a}{2} \tag{6.25}$$

On the other hand, according to Eqs. (6.22) and (6.24):

$$d_\Delta = 2 - D - z = 2 - D - n - a \tag{6.26}$$

Compare Eqs. (6.25) and (6.26), we can derive:

$$a = 4 - D = 2 \tag{6.27}$$

when the spatial dimensionality $D = 2$.

The above result follows from $\alpha \cong 2\beta$ (Eq. (6.20)). Further using $\alpha \cong 1.0$ (and $\beta \cong 0.50$), we find that $n = 2$. Thus, the quantum-critical nematic susceptibility is found to be:

$$\overline{\chi}_{\Delta}^{-1}(q,\omega) = b_1 q^2 + b_2 \frac{|\omega|}{q^2} \tag{6.28}$$

To reiterate, the relation (6.20) suggests the presence of a non-trivial critical dynamical term $|\omega|/q^2$ in the nematic propagator. The origin of such dynamical term in the nematic sector and its relation with the microscopic physics of the iron pnictides will be investigated in a separate work.

6.5 Discussion and Conclusion

To summarize, we have shown how the singular component of the spin excitation anisotropy connects with its counterparts in both the nematic and dynamical magnetic susceptibilities. The derived identity has allowed us to extract the critical properties from the experiments in an optimally doped iron pnictides under a uniaxial strain, including several critical exponents and a singular nematic susceptibility as a function of both frequency and wavevector. Our results demonstrate the success of the spin-driven nematicity for understanding the measured responses in the magnetic and nematic channels. Our approach allows us to determine the dynamical nematic susceptibility, which is difficult to directly measure experimentally. The singular fluctuations in both the nematic and magnetic channels appear in the regime of optimized superconductivity within the iron-pnictide phase diagram. Thus, both are expected to influence the development of the superconductivity.

Chapter 7

Summary

In this thesis, we have studied the quantum criticality in heavy fermion systems and iron pnictides in terms of several theoretical approaches ranging from numerical to analytical methods. We have used the QNLσM to represent the local moments in a Kondo lattice model, and developed a numerical way to non-perturbatively solve the low energy effective Dirac Hamiltonian in a skyrmion background. This has allowed us to study the correlation of various competing order parameters influenced by the skyrmion defects of antiferromagnetism. For the Kondo lattice model on a honeycomb lattice, we have identified both the valence bond solid and Kondo singlet as the leading competing orders to the antiferromagnetism, and their relative stability is tunable by varying the Kondo coupling. These results provide a new unified framework for elucidating the proposed global phase diagram of heavy fermion systems.

In a similar spirit, and motivated by a recent experiment on the geometrically frustrated heavy fermion metal CePdAl, we have performed an RG analysis to explore the role of the Kondo coupling to the QCP of the QNLσM. We have gone beyond the traditional Hert-Millis paradigm by treating both the bosonic and fermionic degrees of freedom on an equal footing. We have also used a large-N method to study the influence of the Kondo coupling to the Fermi surface around the QCP. Our results have shown that the antiferromagnetism to paramagnetism transition driven by the magnetic frustration is stable against the weak Kondo coupling, and the Fermi surface remains small.

Heavy fermion systems provide the setting to explore a very rich variety of quantum phases and quantum criticality. We have taken advantage of this highly desirable feature, and extended the Kondo destruction physics into multipolar heavy fermion systems. Motivated by the experiment in $CePd_{20}Si_6$, we have studied a spin-orbital coupled Bose-Fermi Kondo model, which captures the essential physics of the underlying multipolar Kondo lattice model. By using the bosonization technique, we have mapped this Bose-Fermi Kondo model to a Coulomb gas model, by which we can derive the β functions. We have established a generic phase diagram of this spin-orbital coupled Bose-Fermi Kondo model based on a detailed RG analysis. From this generic phase diagram, we have found that the notion of sequential Kondo destruction is robust, which gives us a firm theoretical basis for the earlier numerical QMC results in a related Kondo model, and for the understanding of quantum criticality in the multipolar heavy fermion systems.

Finally, the general relevance of quantum criticality to a variety of strongly correlated systems is accompanied by the distinctive ingredient that arises in particular classes of such systems. We illustrate this point by considering the interplay between the nematic and antiferromagnetic quantum criticality in the iron pnictides. To do so, we have established an identity through field theoretical methodology that connects the spin excitation anisotropy to the dynamical spin susceptibility and the static nematic susceptibility. Based on this identity and a general scaling analysis, we have demonstrated how to extract the scaling dimension of the nematic order and the dynamical exponent. In turn, this procedure allows us to determine the dynamical nematic susceptibility, which is hard to measure directly. We have illustrated the whole procedure in the optimally Ni-doped $BaFe_2As_2$, and found that the singular energy dependences of the spin excitation anisotropy and the dynamical magnetic

susceptibility observed in the optimally Ni-doped $BaFe_2As_2$ imply the existence of a non-trivial dynamical term $|\omega|/q^2$ in the dynamical nemacit susceptibility. We expect that this understanding of the dynamical nematic susceptibility in the regime of optimal superconductivity will be important to the elucidation of the mechanism for the iron-based high temperature superconductivity.

Appendix A

Appendix of Chapter 3

A.1 Coupling between fermions and nonlinear sigma model

Since we are working with a bipartite honeycomb lattice, an intraunit cell antiferromagnetic phase (Néel order) describes the ground state of a nearest neighbor Heisenberg model. The nonlinear sigma model description for this phase is usually derived by employing a large spin approximation. However, for describing the competing spin singlet orders such as spin Peierls and Kondo singlet it is more advantageous to work with a fermionic description. This is similar to the methods of Affleck and Haldane [114] for one dimensional spin-1/2 chain. The antiferromagnetic phase for honeycomb lattice can only be obtained from a Hubbard model for sufficiently strong onsite repulsion, as the density of states for two dimensional Dirac fermion vanishes at zero energy. The repulsive Hubbard interaction, $H_{int} = U \sum_i \; n_{i,\uparrow} n_{i,\downarrow}$, where $n_{i,s}$ is the density operator for spin projection $s = \uparrow / \downarrow$, can be decoupled in the magnetic channel by performing the following Hubbard-Stratonovich transformation

$$\int \; dc_i^\dagger dc_i \; \exp\left[- \int_0^{\frac{\hbar}{k_B T}} \frac{d\tau}{\hbar} H_{int} \right]$$

$$= \int \; dc_i^\dagger dc_i d\mathbf{M}_i \; \exp\left[- \int_0^{\frac{\hbar}{k_B T}} \frac{d\tau}{\hbar} \left\{ \sum_i \left[\frac{3\mathbf{M}_i^2}{2U} + \mathbf{M}_i \cdot c_{i,s}^\dagger \boldsymbol{\eta}_{s,s'} c_{i,s'} \right] + \frac{U}{2} \sum_{i,s} \; n_{i,s} \right\} \right].$$

Notice that the Hubbard interaction has been decoupled in the magnetic channel in terms of the vectors $\mathbf{M}_i$ ($i = A, B$ are assigned to two sublattices), where $\mathbf{M}_i = (U/3)\langle c_{i,s}^\dagger \boldsymbol{\eta}_{ss'} c_{i,s'} \rangle$. In the process of mean-field decoupling the chemical potential

has to be shifted by the amount $U/2$, to maintain the condition of half-filling. The antiferromagnetic phase corresponds to the choice $\mathbf{M}_A = -\mathbf{M}_B$. Due to the vanishing density of states the antiferromagnetic phase arises for $U > U_c$. Within the continuum limit this leads to the following effective action

$$S = \int d^2x d\tau \left[\bar{\psi}\gamma_\mu \partial_\mu + g\bar{\psi}\mathbf{M}\cdot\boldsymbol{\eta}\psi + \frac{\mathbf{M}^2}{2} \right], \tag{A.1}$$

with $g \propto U$. At $U = U_c$ (equivalently $g = g_c$), we have an itinerant version of paramagnetic semimetal to antiferromagnet quantum phase transition, where the fermion fields and both longitudinal and transverse parts of the order parameter constitute gapless or critical excitations. For $U > U_c$, the amplitude of the order parameter $|\mathbf{M}| \sim |U - U_c|^\beta$ is finite, and away from the itinerant critical regime i.e., at the length scales larger than the correlation length $\xi \sim |U - U_c|^{-\nu}$ we can effectively freeze the amplitude fluctuations of the magnetic order parameter. Since we can denote $\mathbf{M} = |\mathbf{M}|\ \mathbf{n}$, where $\mathbf{n}$ is the unit vector or nonlinear sigma model field, after freezing $\mathbf{M}|$ Eq. (A.1) can be reduced to

$$S = \int d^2x d\tau \left[\bar{\psi}\gamma_\mu \partial_\mu + g_\psi \bar{\psi}\mathbf{n}\cdot\boldsymbol{\eta}\psi \right].$$

This allows us to work with a nonlinear sigma model coupled to Dirac fermions, as used in the main text. The longitudinal part of the nonlinear sigma model field gives rise to a charge gap for the Dirac fermions, and after integrating out the Dirac fermions by following [106, 96, 95] one can obtain a nonlinear sigma model. The ordered phase of the nonlinear sigma model indeed corresponds to the ordered phase obtained within the large spin approximation of nearest neighbor Heisenberg model. An advantage for the effective theory is that the bare stiffness for nonlinear sigma model does not guarantee a global long range order, and it remains possible that the emergent gapped/insulating phase supports a nonmagnetic competing order, where

the Berry phase for the sigma model does not vanish and follows from the evaluation of fermion determinant [96, 95].

A.2 Topological charge of skyrmion and induced charge

The induced charge for each valley is defined as the difference of charge in each valley between system with and without skyrmion (vacuum):

$$\begin{aligned} Q_{\pm} &= \int_{-\infty}^{0} dE\rho_{S,\pm}(E) - \int_{-\infty}^{0} dE\rho_{0,\pm}(E) \\ &= -\frac{1}{2}\int_{-\infty}^{\infty} dE\rho_{S,\pm}(E)\,\mathrm{sign(E)} = -\frac{1}{2}\eta_{\pm} \end{aligned} \tag{A.2}$$

where $\rho_{S,\pm}(E)$ and $\rho_{0,\pm}(E)$ is the density of state at energy E with and without skyrmion for $\pm$ valley, respectively, $\eta_{\pm} = \int_{-\infty}^{\infty} dE\rho_{S,\pm}(E)\,\mathrm{sign(E)} = \int_{0}^{\infty} \mathrm{dE}\,(\rho_{\mathrm{S},\pm}(\mathrm{E}) - \rho_{\mathrm{S},\pm}(-\mathrm{E}))$ is called the spectral asymmetry, and we have used the fact that system without skyrmion field has charge conjugate symmetry.

Since Hamiltonian of Eq. (3.9) does not break valley symmetry, it can be decoupled into each valley space as $H_{\pm}$, the density of states in each valley is well-defined as:

$$\rho_{\pm}(E) \equiv \mathrm{Tr}\,\delta\left(H_{\pm} - E\right) = \frac{1}{\pi}\,\mathrm{Im\,Tr}\left(\frac{1}{H_{\pm} - E - i\epsilon}\right) \tag{A.3}$$

The spectral asymmetry then is:

$$\begin{aligned} \eta_{\pm} &= \int_{0}^{\infty} dE\,(\rho_{S,\pm}(E) - \rho_{S,\pm}(-E)) \\ &= \frac{1}{\pi}\int_{0}^{\infty} dE\left(\mathrm{Im\,Tr}\,\frac{1}{H_{\pm} - E - i\epsilon} - \mathrm{Im\,Tr}\,\frac{1}{H_{\pm} + E - i\epsilon}\right) \\ &= \frac{1}{\pi}\int_{0}^{\infty} dE\,\mathrm{Im\,Tr}\left(\frac{1}{H_{\pm} - E - i\epsilon} + \frac{1}{H_{\pm} + E + i\epsilon}\right) \end{aligned} \tag{A.4}$$

where we use the identity $\frac{1}{x \pm i\eta} = P\left(\frac{1}{x}\right) \mp i\pi\delta(x)$. By changing the variable $z = E + i\epsilon$, we have

$$\begin{aligned} \eta_{\pm} &= \frac{1}{\pi}\,\mathrm{Im}\int_{i\epsilon}^{\infty+i\epsilon} dz\,\mathrm{Tr}\left(\frac{1}{H_{\pm} - z} + \frac{1}{H_{\pm} + z}\right) \\ &= \frac{2}{\pi}\,\mathrm{Im}\int_{i\epsilon}^{\infty+i\epsilon} dz\,\mathrm{Tr}\left(H_{\pm}\frac{1}{H_{\pm}^2 - z^2}\right) \end{aligned} \tag{A.5}$$

In our case, $H_\pm = \pm\left(v_\chi\left(\sigma_1 k_1 + \sigma_2 k_2\right) + g_\chi \boldsymbol{n}\cdot\boldsymbol{\eta}\sigma_3\right) = \pm\left(H_0 + I\right)$, where $H_0 = v_\chi\left(\sigma_1 k_1 + \sigma_2 k_2\right)$ and $I = g_\chi \boldsymbol{n}\cdot\boldsymbol{\eta}\sigma_3$, thus $H_\pm^2 = H_0^2 + V = -v_\chi^2\nabla^2 + g_\chi^2 + i g_\chi v_\chi \sigma_3 \sigma^i \partial_i \boldsymbol{n}\cdot\boldsymbol{\eta}$, where $H_0^2 = -v_\chi^2\nabla^2 + g_\chi^2$ and $V = i g_\chi v_\chi \sigma_3 \sigma^i \partial_i \boldsymbol{n}\cdot\boldsymbol{\eta}$

We assume that background field varies very slowly compared with coupling constant, that is $|\nabla \boldsymbol{n}| \ll g_\chi$, and then expand $\eta_\pm$ in order of $|\nabla \boldsymbol{n}|/g_\chi$:

$$\begin{aligned}
&\mathrm{Tr}\left(H_\pm \frac{1}{H_\pm^2 - z^2}\right) = \mathrm{Tr}\left(H_\pm \frac{1}{H_0^2 + V^2 - z^2}\right) \\
&= \mathrm{Tr}\left(H_\pm G_0\left(z\right)\left(1 + G_0\left(z\right)V\right)^{-1}\right) \\
&= \mathrm{Tr}\left(H_\pm G_0\left(z\right)\sum_{n=0}^{\infty}\left(-G_0\left(z\right)V\right)^n\right)
\end{aligned} \tag{A.6}$$

where $G_0\left(z\right) = \frac{1}{H_0^2 - z^2}$.

By identity $G_0\left(z\right)V = VG_0\left(z\right) + G_0\left(z\right)\left[V, H_0\right]G_0\left(z\right)$, we are now able to separate the trace into pure momentum and real space part, and then do the trace separately. The non-vanishing leading order of (A5) will be $\pm\,\mathrm{Tr}\left(IV^2\right)\mathrm{Tr}\left(G_0^3\left(z\right)\right)$. Since

$$\begin{aligned}
&\mathrm{Tr}\left(IV^2\right) = -g_\chi^3 v_\chi^2\,\mathrm{Tr}\left(\sigma_3^3 \boldsymbol{n}\cdot\boldsymbol{\eta}\sigma^i\partial_i\boldsymbol{n}\cdot\boldsymbol{\eta}\sigma^j\partial_j\boldsymbol{n}\cdot\boldsymbol{\eta}\right) \\
&= -g_\chi^3 v_\chi^2\,\mathrm{Tr}\left(\sigma_3\sigma^i\sigma^j\eta^a\eta^b\eta^c n_a\partial_i n_b\partial_j n_c\right) \\
&= -4g_\chi^3 v_\chi^2\int d^2x\epsilon^{ij}\epsilon^{abc}n_a\partial_i n_b\partial_j n_c \\
&\mathrm{Tr}\left(G_0^3\left(z\right)\right) = \mathrm{Tr}\left(\frac{1}{H_0^2 - z^2}\right)^3 = \mathrm{Tr}\left(\frac{1}{-v_\chi^2\nabla^2 + g_\chi^2 - z^2}\right)^3 \\
&= \int\frac{dk}{\left(2\pi\right)^2}\frac{2\pi k}{\left(v_\chi^2 k^2 + g_\chi^2 - z^2\right)^3} = \frac{1}{8\pi v_\chi^2\left(g_\chi^2 - z^2\right)^2}
\end{aligned} \tag{A.7}$$

Consequently, the leading order of $\eta_\pm$ will be

$$\begin{aligned}
&\frac{\mp 8 g_\chi^3 v_\chi^2}{\pi}\,\mathrm{Im}\int_{i\epsilon}^{\infty+i\epsilon}\frac{dz}{8\pi v_\chi^2\left(g_\chi^2 - z^2\right)^2}\int d^2x\epsilon^{ij}\epsilon^{abc}n_a\partial_i n_b\partial_j n_c \\
&= \frac{\mp\,\mathrm{sign}\left(g_\chi\right)}{4\pi}\int d^2x\epsilon^{ij}\epsilon^{abc}n_a\partial_i n_b\partial_j n_c
\end{aligned} \tag{A.8}$$

Therefore,

$$\begin{aligned} Q_{\pm} &= -\frac{1}{2}\eta_{\pm} = \frac{\pm \operatorname{sign}(g_{\chi})}{8\pi} \int d^2x \epsilon^{ij} \epsilon^{abc} n_a \partial_i n_b \partial_j n_c \\ &= \pm \operatorname{sign}(g_{\chi})\, Q_{top} \end{aligned} \tag{A.9}$$

Appendix B

Appendix of Chapter 4

B.1 Renormalization group calculation for X-Y component of Kondo coupling

In this appendix, we aim to derive the Beta function of the Kondo coupling λ_K (4.23) from the XY Kondo vertex $\lambda_\perp = \sqrt{g}\lambda_K$. To calculate the one-loop correction to the XY Kondo vertex $\lambda_\perp$, we need to include a higher order vertex which results from expanding $1/\sigma$ in the Eq. (4.5) and is not included in Fig. (4.1). Fig. (B.1) is the Feynman rule of such vertex.

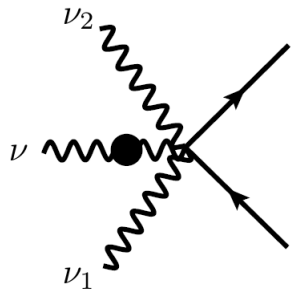

$$g^{\frac{3}{2}}\lambda_K\left(\frac{1}{2}\pi_+^2\dot{\pi}_- - \frac{1}{2}\pi_-^2\dot{\pi}_- - \pi_+\pi_-\dot{\pi}_+\right)s_c^x$$
$$+\, g^{\frac{3}{2}}\lambda_K\left(-\frac{1}{2}\pi_-^2\dot{\pi}_+ + \frac{1}{2}\pi_+^2\dot{\pi}_+ + \pi_-\pi_+\dot{\pi}_-\right)s_c^y$$

Figure B.1 : Feynman rule for a high-order XY component of the Kondo coupling.

The one-loop diagram to the XY Kondo vertex $\lambda_\perp$ is shown in Fig. (B.2). Such diagram is vanishing after performing the components summation. Therefore, at one-loop level we have:

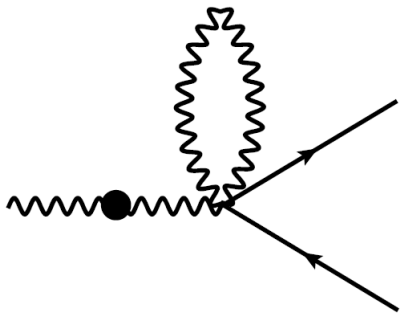

Figure B.2 : One-loop correction diagram for XY Kondo vertex.

$$(\lambda_\perp)' = \lambda_\perp \xi_\pi^{-1} \xi_\psi^{-2} b^{(D+4)} \tag{B.1}$$

Together with Eq. (4.17) and Eq. (4.20), the Beta function of $\lambda_\perp$ can be derived:

$$\beta(\lambda_\perp) = -\frac{1}{2}\epsilon\lambda_\perp - \frac{1}{2}g\lambda_\perp \tag{B.2}$$

By using $\lambda_\perp = \sqrt{g}\lambda_K$, one can verify from Eq. (B.2) that

$$\beta(\lambda_K) = -g\lambda_K \tag{B.3}$$

which is consistent with Eq. (4.23). As we have pointed out, the $O(3)$ symmetry of the action (4.3) guarantees such consistency.

Appendix C

Appendix of Chapter 5

C.1 Derivation of the Coulomb gas action and RG equations

As we mentioned in the Chapter 5, because of the Ising-type couplings in H_{BK} (5.13), the whole Bose-Fermi Kondo model (5.8) breaks not only the SU(4) symmetry but also the SU(2)×SU(2) symmetry. Therefore, to perform the RG calculation, one need to reduce the symmetry in the Kondo part H_K and introduce much more Kondo couplings. To our purpose, the model with the minimal number of parameters that we need to consider is:

$$
\begin{aligned}
&H_{BFK} = H_0 + H_K + H_{KB} \\
&H_0 = \sum_{i\alpha} \lambda f^\dagger_{i\alpha} f_{i\alpha} + \sum_{p,i\alpha} \epsilon_p c^\dagger_{p,i\alpha} c_{p,i\alpha} + \sum_q W_q \left(\vec{\phi}^\dagger_{\sigma,q} \cdot \vec{\phi}_{\sigma,q} + \vec{\phi}^\dagger_{\tau,q} \cdot \vec{\phi}_{\tau,q} \right) \\
&H_K = J_{\sigma z} \sigma^z \sigma^z_c + J_{\sigma\perp} \left(\sigma^x \sigma^x_c + \sigma^y \sigma^y_c \right) + J_{\tau z} \tau^z \tau^z_c + J_{\tau\perp} \left(\tau^x \tau^x_c + \tau^y \tau^y_c \right) \\
&+ 4J_{M1} \left[(\sigma_x \otimes \tau_x) (\sigma_x \otimes \tau_x)_c + (\sigma_x \otimes \tau_y) (\sigma_x \otimes \tau_y)_c + (\sigma_y \otimes \tau_x) (\sigma_y \otimes \tau_x)_c + (\sigma_y \otimes \tau_y) (\sigma_y \otimes \tau_y)_c \right] \\
&+ 4J_{M2} \left[(\sigma_z \otimes \tau_x) (\sigma_z \otimes \tau_x)_c + (\sigma_z \otimes \tau_y) (\sigma_z \otimes \tau_y)_c \right] \\
&+ 4J_{M3} \left[(\sigma_x \otimes \tau_z) (\sigma_x \otimes \tau_z)_c + (\sigma_y \otimes \tau_z) (\sigma_y \otimes \tau_z)_c \right] \\
&+ 4J_{M4} \left[(\sigma_z \otimes \tau_z) (\sigma_z \otimes \tau_z)_c \right] \\
&H_{BK} = g_{\sigma z} \sigma_z \phi_{\sigma z} + g_{\tau z} \tau_z \phi_{\tau z}
\end{aligned}
\tag{C.1}
$$

where $\vec{\phi}_{\sigma/\tau} = \sum_q \left(\vec{\phi}_{\sigma/\tau,q} + \vec{\phi}^\dagger_{\sigma/\tau,-q} \right)$, and $J_{\sigma\perp} = J_{M3}$ and $J_{\tau\perp} = J_{M2}$.

For the Ising-type bosonic coupling, to perform a controllable RG calculation, one need to map the Bose-Fermi Kondo model into a Coulomb gas type model[75, 145]. The first step to decompose the above Hamiltonian H_{BFK} into the part that is diagonal in the space of the local impurity states $|\sigma\rangle \otimes |\tau\rangle$, and the other part that is not:

$$H_{BFK} = H_0 + H_f \tag{C.2}$$

where H_0 is diagonal in the space of the local impurity states $|\sigma\rangle \otimes |\tau\rangle$. We use the notation $|m\rangle = |i\alpha\rangle$ to denote a local impurity state with the orbital $i = 1, 2$ and the spin $\alpha = \uparrow, \downarrow$. Therefore,

$$H_0 = \sum_m H_m |m\rangle\langle m| \tag{C.3}$$

Then we rewrite H_m in term of the projection operators $X_{mm} = |m\rangle\langle m| = |i\alpha\rangle\langle i\alpha|$, so that:

$$\begin{aligned} H_m = E_m &+ \sum_n V_m^n c_n^\dagger c_n + \sum_{k,n} E_k c_{k,n}^\dagger c_{k,n} + \sum_q W_q \left(\vec{\phi}_{\sigma,q}^\dagger \cdot \vec{\phi}_{\sigma,q} + \vec{\phi}_{\tau,q}^\dagger \cdot \vec{\phi}_{\tau,q} \right) \\ &+ \sum_q F_{\sigma,q}^m \left(\phi_{\sigma z,q} + \phi_{\sigma z,-q}^\dagger \right) + \sum_q F_{\tau,q}^m \left(\phi_{\tau z,q} + \phi_{\tau z,-q}^\dagger \right) \end{aligned} \tag{C.4}$$

where

$$\begin{aligned} V_{i\alpha}^{i\alpha} &= \frac{1}{4} \left(J_{\sigma z} + J_{\tau z} + J_{M4} \right) \\ V_{i\alpha}^{i\bar{\alpha}} &= \frac{1}{4} \left(J_{\tau z} - J_{\sigma z} - J_{M4} \right) \\ V_{i\alpha}^{\bar{i}\alpha} &= \frac{1}{4} \left(J_{\sigma z} - J_{\tau z} - J_{M4} \right) \\ V_{i\alpha}^{\bar{i}\bar{\alpha}} &= -\frac{1}{4} \left(J_{\sigma z} + J_{\tau z} - J_{M4} \right) \end{aligned} \tag{C.5}$$

and

$$\begin{aligned} F_{\sigma,q}^{i\uparrow} &= g_{\sigma z} \\ F_{\sigma,q}^{i\downarrow} &= -g_{\sigma z} \\ F_{\tau,q}^{1\alpha} &= g_{\tau z} \\ F_{\tau,q}^{2\alpha} &= -g_{\tau z} \end{aligned} \tag{C.6}$$

One the other hand, the flipping part is defined as:

$$H_f = \sum_{m \neq n} Q\left(m,n\right) \tag{C.7}$$

where

$$Q\left(m,m\right) = |m\rangle\langle m|H_f|n\rangle\langle n| \tag{C.8}$$

describing the process of flipping from the local impurity state $|n\rangle$ to $|m\rangle$. Specifically,

$$\begin{aligned} Q\left(i\alpha,\bar{i}\overline{\alpha}\right) &= J_{M1} f_{i\alpha}^{\dagger} f_{\bar{i}\overline{\alpha}} c_{\bar{i}\overline{\alpha}}^{\dagger} c_{i\alpha} \\ Q\left(i\alpha,i\overline{\alpha}\right) &= \frac{1}{2}\left(J_{\sigma\perp} - J_{M3}\right) f_{i\alpha}^{\dagger} f_{i\overline{\alpha}} c_{\bar{i}\overline{\alpha}}^{\dagger} c_{\bar{i}\alpha} + \frac{1}{2}\left(J_{\sigma\perp} + J_{M3}\right) f_{i\alpha}^{\dagger} f_{i\overline{\alpha}} c_{i\overline{\alpha}}^{\dagger} c_{i\alpha} = J_{\sigma\perp} f_{i\alpha}^{\dagger} f_{i\overline{\alpha}} c_{i\overline{\alpha}}^{\dagger} c_{i\alpha} \\ Q\left(i\alpha,\bar{i}\alpha\right) &= \frac{1}{2}\left(J_{\tau\perp} - J_{M2}\right) f_{i\alpha}^{\dagger} f_{\bar{i}\alpha} c_{\bar{i}\overline{\alpha}}^{\dagger} c_{i\overline{\alpha}} + \frac{1}{2}\left(J_{\tau\perp} + J_{M2}\right) f_{i\alpha}^{\dagger} f_{\bar{i}\alpha} c_{\bar{i}\alpha}^{\dagger} c_{i\alpha} = J_{\tau\perp} f_{i\alpha}^{\dagger} f_{\bar{i}\alpha} c_{\bar{i}\alpha}^{\dagger} c_{i\alpha} \end{aligned} \tag{C.9}$$

since $J_{\sigma\perp} = J_{M3}$ and $J_{\tau\perp} = J_{M2}$.

Since H_0 is diagonal in the local impurity states, after tracing out these local states, the partition function can be expanded in H_f, and the results is:

$$Z = \sum_{n=0}^{\infty} \int_0^{\beta} d\tau_n ... \int_0^{\tau_{i+1}} d\tau_i ... \int_0^{\tau_2} d\tau_1 \sum_m A\left(m;\tau_n,...,\tau_1\right) \tag{C.10}$$

Here the transition amplitude is defined as:

$$\begin{aligned} A\left(m;\tau_n,...\tau_1\right) &= (-1)^n \sum_{m_2,...,m_n} \int DcD\phi \exp\left[-H_m\left(\beta-\tau_n\right)\right] Q'\left(m,m_n\right) \times ... \\ &\times \exp\left[-H_{m_{i+1}}\left(\tau_{i+1}-\tau_i\right)\right] Q'\left(m_{i+1},m_i\right) \exp\left[-H_{m_i}\left(\tau_i-\tau_{i-1}\right)\right] \times ... \\ &\times \exp\left[-H_{m_2}\left(\tau_2-\tau_1\right)\right] Q'\left(m_2,m\right) \exp\left[-H_m\tau_1\right] \end{aligned} \tag{C.11}$$

where

$$Q'\left(m_{i+1}, m_i\right) = \langle m_{i+1}|H_f|m_i\rangle \tag{C.12}$$

, which can be separated as:

$$\langle m|H_f|n\rangle = y'_{m,n} O'\left(m, n\right) \tag{C.13}$$

with

$$\begin{aligned}
y'_{i\alpha,i\alpha} &= \frac{1}{4}\left(J_{\sigma z} + J_{\tau z} + J_{M4}\right) \\
y'_{i\alpha,\bar{i}\bar{\alpha}} &= J_{M1} \\
y'_{i\alpha,i\bar{\alpha}} &= \frac{1}{2}\left(J_{\sigma\perp} + J_{M3}\right) = J_{\sigma\perp} \\
y_{i\alpha,\bar{i}\alpha} &= \frac{1}{2}\left(J_{\tau\perp} + J_{M2}\right) = J_{\tau\perp} \\
O'_{i\alpha,i\alpha} &= c^{\dagger}_{i\alpha} c_{i\alpha} \\
O'_{i\alpha,\bar{i}\bar{\alpha}} &= c^{\dagger}_{\bar{i}\bar{\alpha}} c_{i\alpha} \\
O'_{i\alpha,i\bar{\alpha}} &= c^{\dagger}_{i\bar{\alpha}} c_{i\alpha} \\
O'_{i\alpha,i\bar{\alpha}} &= c^{\dagger}_{\bar{i}\alpha} c_{i\alpha}
\end{aligned} \tag{C.14}$$

Now we can trace out the conduction electron by using the bosonization technique. For our local impurity problem, we only need to consider the S-wave component:

$$c_{i\alpha}\left(x\right) = \frac{1}{\sqrt{2\pi a}} e^{-i\theta_{i\alpha}(x)} \tag{C.15}$$

The projected Hamiltonian thus transforms into:

$$H_m = H_c + H_{\phi_\sigma} + H_{\phi_\tau} + E'_m + \sum_n \frac{\delta^n_m}{\pi\rho_0}\left(\frac{d\theta_n\left(x\right)}{dx}\right) + \sum_q F^m_{\sigma,q}\left(\phi_{\sigma z,q} + \phi^{\dagger}_{\sigma z,-q}\right) + \sum_q F^m_{\tau,q}\left(\phi_{\tau z,q} + \phi^{\dagger}_{\tau z,-q}\right) \tag{C.16}$$

where $E'_m = E_m + \Delta E_m$, ρ_0 is the bare conduction electron density of state, and $\delta^{j\beta}_{i\alpha}$

is the phase shift from the scattering potential:

$$\begin{aligned}
\delta_{i\alpha}^{i\alpha} &= \tan^{-1}\left(\pi\rho_0 V_{i\alpha}^{i\alpha}\right) = \tan^{-1}\left[\frac{\pi\rho_0}{4}\left(J_{\sigma z}+J_{\tau z}+J_{M4}\right)\right] \\
\delta_{i\alpha}^{i\overline{\alpha}} &= \tan^{-1}\left(\pi\rho_0 V_{i\alpha}^{i\overline{\alpha}}\right) = \tan^{-1}\left[\frac{\pi\rho_0}{4}\left(J_{\tau z}-J_{\sigma z}-J_{M4}\right)\right] \\
\delta_{i\alpha}^{\bar{i}\alpha} &= \tan^{-1}\left(\pi\rho_0 V_{i\alpha}^{\bar{i}\alpha}\right) = \tan^{-1}\left[\frac{\pi\rho_0}{4}\left(J_{\sigma z}-J_{\tau z}-J_{M4}\right)\right] \\
\delta_{i\alpha}^{\bar{i}\overline{\alpha}} &= \tan^{-1}\left(\pi\rho_0 V_{i\alpha}^{\bar{i}\overline{\alpha}}\right) = \tan^{-1}\left[-\frac{\pi\rho_0}{4}\left(J_{\sigma z}+J_{\tau z}-J_{M4}\right)\right]
\end{aligned} \tag{C.17}$$

The history dependent potential is treated then through introducing a canonical transformation at each imaginary time:

$$U_\delta = \exp\left(i\frac{\delta}{\pi}\theta\right) \tag{C.18}$$

The potential after the canonical transformation is time-independent because of the property:

$$U_\delta^\dagger H_c U_\delta = H_c + \frac{\delta}{\pi\rho_0}\frac{d\theta}{dx} \tag{C.19}$$

We also introduce a similar canonical transformation to the bosonic degree of freedom,

$$\begin{aligned}
U_{W_{\sigma,m}} &= \exp\left(\sum_q \frac{F_{\sigma,q}^\alpha}{W_q}\left(\phi_{\sigma z,q}-\phi_{\sigma z,-q}^\dagger\right)\right) \\
U_{W_{\tau,m}} &= \exp\left(\sum_q \frac{F_{\tau,q}^\alpha}{W_q}\left(\phi_{\tau z,q}-\phi_{\tau z,-q}^\dagger\right)\right)
\end{aligned} \tag{C.20}$$

with the property:

$$\begin{aligned}
U_{W_{\sigma,m}}^\dagger H_{\phi_\sigma} U_{W_{\sigma,m}} &= H_{\phi_\sigma} + \sum_q F_{\sigma,q}^m\left(\phi_{\sigma z,q}+\phi_{\sigma z,-q}^\dagger\right) \\
U_{W_{\tau,m}}^\dagger H_{\phi_\tau} U_{W_{\tau,m}} &= H_{\phi_\tau} + \sum_q F_{\tau,q}^m\left(\phi_{\tau z,q}+\phi_{\tau z,-q}^\dagger\right)
\end{aligned} \tag{C.21}$$

The transition amplitude now reduce to:

$$\begin{aligned}
&A\left(m;\tau_n,...,\tau_1\right)=Z_c\sum_{m_{n+1}=\alpha_1=m,m_2,...m_{n-1}}y'_{m_{n+1},\alpha_n}...y'_{m_{i+1},m_i}...y'_{m_2,m_1}\\
&\times\exp\left[-E'_m\left(\tau_1-\tau_n\right)-\sum_{i=2}^{n-1}E'_{m_{i+1}}\left(\tau_{i+1}-\tau_i\right)\right]\\
&\times\left\langle O\left(m_{n+1},m_n\right)\left(\tau_n\right)...O\left(m_{i+1},m_i\right)\left(\tau_i\right)...O\left(m_2,m_1\right)\left(\tau_1\right)\right\rangle\\
&\times\left\langle B_\sigma\left(m_{n+1},m_n\right)\left(\tau_n\right)...B_\tau\left(m_{i+1},m_i\right)\left(\tau_i\right)...B_\sigma\left(m_2,m_1\right)\left(\tau_1\right)\right\rangle\\
&\times\left\langle B_\tau\left(m_{n+1},m_n\right)\left(\tau_n\right)...B_\tau\left(m_{i+1},m_i\right)\left(\tau_i\right)...B_\tau\left(m_2,m_1\right)\left(\tau_1\right)\right\rangle
\end{aligned}\tag{C.22}$$

Here, for the bosonic part

$$\begin{aligned}
B_\sigma\left(m_{i+1},M_i\right)\left(\tau_i\right)&=U_{W_{\sigma,m_{i+1}}}U^\dagger_{W_{\sigma,m_i}}\left(\tau_i\right)\\
B_\tau\left(m_{i+1},m_i\right)\left(\tau_i\right)&=U_{W_{\tau,m_{i+1}}}U^\dagger_{W_{\tau,m_i}}\left(\tau_i\right)
\end{aligned}\tag{C.23}$$

, the correlation function can be reduced into

$$\begin{aligned}
&\left\langle B_\sigma\left(m_{n+1},m_n\right)\left(\tau_n\right)...B_\sigma\left(m_2,m_1\right)\left(\tau_1\right)\right\rangle=U_{W_{\sigma,m_{i+1}}}U^\dagger_{W_{\sigma,m_i}}\left(\tau_i\right)\\
&=\left\langle\prod_i\exp\left(-\sum_q\frac{F^{m_{i+1}m_i}_{\sigma,q}}{W_q}\left(\phi_{\sigma z,q}-\phi^\dagger_{\sigma z,-q}\right)\left(\tau_i\right)\right)\right\rangle\\
&=\left\langle\exp\left(\sum_{ij}C_\sigma\left(\tau_i-\tau_j\right)\right)\exp\left(\Delta_E\right)\right\rangle
\end{aligned}\tag{C.24}$$

and similarly

$$\begin{aligned}
&\left\langle B_\tau\left(m_{n+1},m_n\right)\left(\tau_n\right)...B_\tau\left(m_2,m_1\right)\left(\tau_1\right)\right\rangle\\
&=U_{W_{\tau,m_{i+1}}}U^\dagger_{W_{\tau,m_i}}\left(\tau_i\right)=\left\langle\prod_i\exp\left(-\sum_q\frac{F^{m_{i+1}m_i}_{\tau,q}}{W_q}\left(\phi_{\tau z,q}-\phi^\dagger_{\tau z,-q}\right)\left(\tau_i\right)\right)\right\rangle\\
&=\left\langle\exp\left(\sum_{ij}C_\tau\left(\tau_i-\tau_j\right)\right)\exp\left(\Delta_E\right)\right\rangle
\end{aligned}\tag{C.25}$$

where

$$\begin{aligned}
F^{m_{i+1}m_i}_{\sigma,q}&=F^{m_{i+1}}_{\sigma z,q}-F^{m_i}_{\sigma z,q}\\
C_\sigma\left(\tau_i-\tau_j\right)&=\sum_q\frac{F^{m_{i+1}mi}_{\sigma,q}F^{m_{j+1}m_j}_{\sigma,q}}{W_q^2}\exp\left(-W_q\left(\tau_j-\tau_i\right)\right)
\end{aligned}\tag{C.26}$$

$$
\begin{aligned}
&F_{\tau,q}^{m_{i+1}m_i} = F_{\tau z,q}^{m_{i+1}} - F_{\tau z,q}^{m_i} \\
&C_\tau\left(\tau_i - \tau_j\right) = \sum_q \frac{F_{\tau,q}^{m_{i+1}mi} F_{\tau,q}^{m_{j+1}m_j}}{W_q^2} \exp\left(-W_q\left(\tau_j - \tau_i\right)\right)
\end{aligned}
\tag{C.27}
$$

with

$$
\sum_q \exp\left(-W_q\tau\right) = \frac{K_\gamma}{\tau^{1+\gamma}} \tag{C.28}
$$

On the other hand, for the conduction electron part

$$
O\left(m_{i+1}, m_i\right)\left(\tau_i\right) = \exp\left(H_c\tau_i\right) O\left(m_{i+1}, m_i\right) \exp\left(-H_c\tau_i\right) \tag{C.29}
$$

Here,

$$
O\left(m_{i+1}, m_i\right) = \left(\prod_n U_{\delta_{m_{i+1}}^n}\right) O'\left(m, m_i\right) \left(\prod_n U_{\delta_{n_i}^n}^\dagger\right) \tag{C.30}
$$

and for different channels, they are:

$$
\begin{aligned}
&O\left(i\alpha, i\alpha\right) = \prod_{j\beta} U_{i\alpha}^{j\beta} c_{i\alpha}^\dagger c_{i\alpha} \prod_{j\beta} U_{i\alpha}^{\dagger j\beta} = 1 \\
&O\left(i\alpha, \bar{i}\bar{\alpha}\right) = \prod_{j\beta} U_{i\alpha}^{j\beta} c_{\bar{i}\bar{\alpha}}^\dagger c_{i\alpha} \prod_{j\beta} U_{\bar{i}\bar{\alpha}}^{\dagger j\beta} \\
&= \exp\left[\left(\frac{\delta_{i\alpha}^{i\alpha}}{\pi} - \frac{\delta_{\bar{i}\bar{\alpha}}^{i\alpha}}{\pi} - 1\right)\theta_{i\alpha} + \left(\frac{\delta_{i\alpha}^{i\bar{\alpha}}}{\pi} - \frac{\delta_{\bar{i}\bar{\alpha}}^{i\bar{\alpha}}}{\pi}\right)\theta_{i\bar{\alpha}} + \left(\frac{\delta_{i\alpha}^{\bar{i}\alpha}}{\pi} - \frac{\delta_{\bar{i}\bar{\alpha}}^{\bar{i}\alpha}}{\pi}\right)\theta_{\bar{i}\alpha} + \left(\frac{\delta_{i\alpha}^{\bar{i}\bar{\alpha}}}{\pi} - \frac{\delta_{\bar{i}\bar{\alpha}}^{\bar{i}\bar{\alpha}}}{\pi} + 1\right)\theta_{\bar{i}\bar{\alpha}}\right] \\
&O\left(i\alpha, i\bar{\alpha}\right) = \prod_{j\beta} U_{i\alpha}^{j\beta} c_{i\bar{\alpha}}^\dagger c_{i\alpha} \prod_{j\beta} U_{i\bar{\alpha}}^{\dagger j\beta} \\
&= \exp\left[\left(\frac{\delta_{i\alpha}^{i\alpha}}{\pi} - \frac{\delta_{i\bar{\alpha}}^{i\alpha}}{\pi} - 1\right)\theta_{i\alpha} + \left(\frac{\delta_{i\alpha}^{i\bar{\alpha}}}{\pi} - \frac{\delta_{i\bar{\alpha}}^{i\bar{\alpha}}}{\pi} + 1\right)\theta_{i\bar{\alpha}} + \left(\frac{\delta_{i\alpha}^{\bar{i}\alpha}}{\pi} - \frac{\delta_{i\bar{\alpha}}^{\bar{i}\alpha}}{\pi}\right)\theta_{\bar{i}\alpha} + \left(\frac{\delta_{i\alpha}^{\bar{i}\bar{\alpha}}}{\pi} - \frac{\delta_{i\bar{\alpha}}^{\bar{i}\bar{\alpha}}}{\pi}\right)\theta_{\bar{i}\bar{\alpha}}\right] \\
&O\left(i\alpha, \bar{i}\alpha\right) = \prod_{j\beta} U_{i\alpha}^{j\beta} c_{\bar{i}\alpha}^\dagger c_{i\alpha} \prod_{j\beta} U_{\bar{i}\alpha}^{\dagger j\beta} \\
&= \exp\left[\left(\frac{\delta_{i\alpha}^{i\alpha}}{\pi} - \frac{\delta_{\bar{i}\alpha}^{i\alpha}}{\pi} - 1\right)\theta_{i\alpha} + \left(\frac{\delta_{i\alpha}^{i\bar{\alpha}}}{\pi} - \frac{\delta_{\bar{i}\alpha}^{i\bar{\alpha}}}{\pi}\right)\theta_{i\bar{\alpha}} + \left(\frac{\delta_{i\alpha}^{\bar{i}\alpha}}{\pi} - \frac{\delta_{\bar{i}\alpha}^{\bar{i}\alpha}}{\pi} + 1\right)\theta_{\bar{i}\alpha} + \left(\frac{\delta_{i\alpha}^{\bar{i}\bar{\alpha}}}{\pi} - \frac{\delta_{\bar{i}\alpha}^{\bar{i}\bar{\alpha}}}{\pi}\right)\theta_{\bar{i}\bar{\alpha}}\right]
\end{aligned}
\tag{C.31}
$$

We can rewrite these term as:

$$
O\left(m, n\right) = \exp\left[i\sum_r e_{mn}^r \theta_r\right] \tag{C.32}
$$

After all of these, the partition function is mapped into:

$$\frac{Z}{Z_0}=\sum_{n=0}^{\infty}\sum_{m_{n+1}=m_1=m,m_2,...m_{n-1}}\int_{\xi_0}^{\beta-\xi_0}\frac{d\tau_n}{\xi_0}...\int_{\xi_0}^{\tau_{i+1}-\xi_0}\frac{d\tau_i}{\xi_0}...\int_{\xi_0}^{\tau_2-\xi_0}\frac{d\tau_1}{\xi_0}\exp\left[-S\left(\tau_1,...,\tau_n\right)\right] \tag{C.33}$$

with a Coulomb gas type action:

$$\begin{aligned}
S\left(\tau_1,...,\tau_n\right)=&-\sum_i \ln y_{m_i,m_{i+1}}+\sum_i h_{m_{i+1}}\frac{\tau_{i+1}-\tau_i}{\xi_0}\\
&+\sum_{i<j}\left[K_{m_i,m_j}+K_{m_{i+1},m_{j+1}}-K_{m_i,m_{j+1}}-K_{m_{i+1},m_j}\right]\ln\frac{\tau_j-\tau_i}{\xi_0}\\
&+\sum_{i<j}\left[M^{\sigma}_{m_i,m_j}+M^{\sigma}_{m_{i+1},m_{j+1}}-M^{\sigma}_{m_i,m_{j+1}}-M^{\sigma}_{m_{i+1},m_j}\right]\left[\left(\frac{\tau_j-\tau_i}{\xi_0}\right)^{1-\gamma}-1\right]\\
&+\sum_{i<j}\left[M^{\tau}_{m_i,m_j}+M^{\tau}_{m_{i+1},m_{j+1}}-M^{\tau}_{m_i,m_{j+1}}-M^{\tau}_{m_{i+1},m_j}\right]\left[\left(\frac{\tau_j-\tau_i}{\xi_0}\right)^{1-\gamma}-1\right]
\end{aligned} \tag{C.34}$$

where $h_m\propto E'_m$ and

$$\begin{aligned}
y_{m,n}O'\left(m,n\right)&=\langle m|H_f|n\rangle\\
K_{m,n}&=\frac{1}{2}\sum_r\left(e^r_{mn}\right)^2\\
M^{\sigma}_{m,n}&=\frac{1}{2}\sum_q\left(F^{mn}_{\sigma,q}\right)^2\\
M^{\tau}_{m,n}&=\frac{1}{2}\sum_q\left(F^{mn}_{\tau,q}\right)^2
\end{aligned} \tag{C.35}$$

By following these definitions, for the Bose-Fermi Kondo model (C.1), the non-

vanishing fugacity $y_{m,n}$ and stiffness $K_{m,n}$, $M^{\sigma}_{m,n}$ and $M^{\tau}_{m,n}$ are:

$$\begin{aligned}
y'_{i\alpha,\bar{i}\overline{\alpha}} &\equiv y_1 = J_{M1} \\
y'_{i\alpha,i\overline{\alpha}} &\equiv y_2 = J_{\sigma\perp} \\
y_{i\alpha,\bar{i}\alpha} &\equiv y_3 = J_{\tau\perp} \\
K_{i\alpha,\bar{i}\overline{\alpha}} &\equiv K_1 = f_1\left(J_{\sigma z}, J_{\tau z}, J_{M4}\right) \\
K_{i\alpha,i\overline{\alpha}} &\equiv K_2 = f_2\left(J_{\sigma z}, J_{\tau z}, J_{M4}\right) \\
K_{i\alpha,\bar{i}\alpha} &\equiv K_3 = f_3\left(J_{\sigma z}, J_{\tau z}, J_{M4}\right) \\
M^{\sigma}_{i\alpha,\bar{i}\overline{\alpha}} = M^{\sigma}_{i\alpha,i\overline{\alpha}} &\equiv M^{\sigma} = \Gamma\left(\gamma\right) g^2_{\sigma z} \\
M^{\tau}_{i\alpha,\bar{i}\overline{\alpha}} = M^{\tau}_{i\alpha,\bar{i}\alpha} &\equiv M^{\tau} = \Gamma\left(\gamma\right) g^2_{\tau z}
\end{aligned} \tag{C.36}$$

where the explicit expression of $K_{1,2,3}$ is complicated and unnecessary. They come from Eq. (C.31), where the phase shifts are known in Eq. (C.17). The only few things that matter are that they depend only on indices-preserving coupling $J_{\sigma z,\tau z,M4}$, and the range of their bare value is $f_{1,2,3}\left(J_{\sigma z}, J_{\tau z}, J_{M4}\right) \in (0,3)$.

For the Coulomb gas action (C.34), the associated RG equations can be derived through a conventional manner[145, 167, 168, 169], and it turns out:

$$\begin{aligned}
\frac{dy_1}{dl} &= \left(1 - K_1 - M^{\sigma} - M^{\tau}\right) y_1 + 2 y_2 y_3 \\
\frac{dy_2}{dl} &= \left(1 - K_2 - M^{\sigma}\right) y_2 + 2 y_1 y_3 \\
\frac{dy_3}{dl} &= \left(1 - K_3 - M^{\tau}\right) y_3 + 2 y_1 y_2 \\
\frac{dK_1}{dl} &= -2y_1^2\left(2K_1\right) - 2y_2^2\left(K_1 + K_2 - K_3\right) - 2y_3^2\left(K_1 + K_3 - K_2\right) \\
\frac{dK_2}{dl} &= -2y_1^2\left(K_2 + K_1 - K_3\right) - 2y_2^2\left(2K_2\right) - 2y_3^2\left(K_2 + K_3 - K_1\right) \\
\frac{dK_3}{dl} &= -2y_1^2\left(K_3 + K_1 - K_2\right) - 2y_2^2\left(K_3 + K_2 - K_1\right) - 2y_3^2\left(2K_3\right) \\
\frac{dM^{\sigma}}{dl} &= \left(\epsilon - 4y_1^2 - 4y_2^2\right) M^{\sigma} \\
\frac{dM^{\tau}}{dl} &= \left(\epsilon - 4y_1^2 - 4y_3^2\right) M^{\tau}
\end{aligned} \tag{C.37}$$

where $\epsilon = 1 - \gamma$.

C.2 RG analysis and the generic phase diagram

In this section, we give a detailed RG analysis of the β functions (C.37). We also illustrate the generic phase diagram Fig. (5.7) based on our RG analysis.

C.2.1 RG analysis

By identifying the zeros of the β functions (C.37), one can find the fixed points:

$$(\mathbf{F1}):\ y_1 = \frac{\sqrt{\epsilon}}{2},\ y_2 = 0,\ y_3 = 0,\ K_2 = K_3 = k,\ K_1 = 0,\ M^\sigma + M^\tau = 1$$

$$(\mathbf{F2}):\ y_1 = 0,\ y_2 = \frac{\sqrt{\epsilon}}{2},\ y_3 = 0,\ K_1 = K_3 = k,\ K_2 = 0,\ M^\sigma = 1,\ M^\tau = 0$$

$$(\mathbf{F3}):\ y_1 = 0,\ y_2 = 0,\ y_3 = \frac{\sqrt{\epsilon}}{2},\ K_1 = K_2 = k,\ K_3 = 0,\ M^\sigma = 0,\ M^\tau = 1$$

$$(\mathbf{F4}):\ y_1 = y_2 = y_3 = 0,\ K_1 = k_1,\ K_2 = k_2,\ K_3 = k_3,\ M^\sigma = M^\tau = 0$$

The RG flow trajectory around these fixed points can be analysed through the eigenvalues and eigenvectors of the matrix:

$$W = \begin{pmatrix}
\frac{\partial\beta_{y_1}}{\partial y_1} & \frac{\partial\beta_{y_1}}{\partial y_2} & \frac{\partial\beta_{y_1}}{\partial y_3} & \frac{\partial\beta_{y_1}}{\partial K_1} & \frac{\partial\beta_{y_1}}{\partial K_2} & \frac{\partial\beta_{y_1}}{\partial K_3} & \frac{\partial\beta_{y_1}}{\partial M^\sigma} & \frac{\partial\beta_{y_1}}{\partial M^\tau} \\
\frac{\partial\beta_{y_2}}{\partial y_1} & \frac{\partial\beta_{y_2}}{\partial y_2} & \frac{\partial\beta_{y_2}}{\partial y_3} & \frac{\partial\beta_{y_2}}{\partial K_1} & \frac{\partial\beta_{y_2}}{\partial K_2} & \frac{\partial\beta_{y_2}}{\partial K_3} & \frac{\partial\beta_{y_2}}{\partial M^\sigma} & \frac{\partial\beta_{y_2}}{\partial M^\tau} \\
\frac{\partial\beta_{y_3}}{\partial y_1} & \frac{\partial\beta_{y_3}}{\partial y_2} & \frac{\partial\beta_{y_3}}{\partial y_3} & \frac{\partial\beta_{y_3}}{\partial K_1} & \frac{\partial\beta_{y_3}}{\partial K_2} & \frac{\partial\beta_{y_3}}{\partial K_3} & \frac{\partial\beta_{y_3}}{\partial M^\sigma} & \frac{\partial\beta_{y_3}}{\partial M^\tau} \\
\frac{\partial\beta_{K_1}}{\partial y_1} & \frac{\partial\beta_{K_1}}{\partial y_2} & \frac{\partial\beta_{K_1}}{\partial y_3} & \frac{\partial\beta_{K_1}}{\partial K_1} & \frac{\partial\beta_{K_1}}{\partial K_2} & \frac{\partial\beta_{K_1}}{\partial K_3} & \frac{\partial\beta_{K_1}}{\partial M^\sigma} & \frac{\partial\beta_{K_1}}{\partial M^\tau} \\
\frac{\partial\beta_{K_2}}{\partial y_1} & \frac{\partial\beta_{K_2}}{\partial y_2} & \frac{\partial\beta_{K_2}}{\partial y_3} & \frac{\partial\beta_{K_2}}{\partial K_1} & \frac{\partial\beta_{K_2}}{\partial K_2} & \frac{\partial\beta_{K_2}}{\partial K_3} & \frac{\partial\beta_{K_2}}{\partial M^\sigma} & \frac{\partial\beta_{K_2}}{\partial M^\tau} \\
\frac{\partial\beta_{K_3}}{\partial y_1} & \frac{\partial\beta_{K_3}}{\partial y_2} & \frac{\partial\beta_{K_3}}{\partial y_3} & \frac{\partial\beta_{K_3}}{\partial K_1} & \frac{\partial\beta_{K_3}}{\partial K_2} & \frac{\partial\beta_{K_3}}{\partial K_3} & \frac{\partial\beta_{K_3}}{\partial M^\sigma} & \frac{\partial\beta_{K_3}}{\partial M^\tau} \\
\frac{\partial\beta_{M^\sigma}}{\partial y_1} & \frac{\partial\beta_{M^\sigma}}{\partial y_2} & \frac{\partial\beta_{M^\sigma}}{\partial y_3} & \frac{\partial\beta_{M^\sigma}}{\partial K_1} & \frac{\partial\beta_{M^\sigma}}{\partial K_2} & \frac{\partial\beta_{M^\sigma}}{\partial K_3} & \frac{\partial\beta_{M^\sigma}}{\partial M^\sigma} & \frac{\partial\beta_{M^\sigma}}{\partial M^\tau} \\
\frac{\partial\beta_{M^\tau}}{\partial y_1} & \frac{\partial\beta_{M^\tau}}{\partial y_2} & \frac{\partial\beta_{M^\tau}}{\partial y} & \frac{\partial\beta_{M^\tau}}{\partial K_1} & \frac{\partial\beta_{M_3^\tau}}{\partial K_2} & \frac{\partial\beta_{M^\tau}}{\partial K_3} & \frac{\partial\beta_{M^\tau}}{\partial M^\sigma} & \frac{\partial\beta_{M^\tau}}{\partial M^\tau}
\end{pmatrix} \tag{C.38}$$

and then one can conclude that except the fixed point **F1**, which is a generic critical

point, other are just unstable fixed points. The RG trajectory around the critical point **F1** flow toward either a strong coupling SU(4) Kondo-screened(KS) fixed point:

$$(\mathbf{S1}):\ y_1, y_2, y_3 \to \infty,\ K_1 = K_2 = K_3 = 0,\ M^\sigma = M^\tau = 0$$

or a spin and orbital Kondo-destroyed(KD) phase:

$$(\mathbf{G}):\ y_1 = y_2 = y_3 = 0,\ K_1 = k_1,\ K_2 = k_2,\ K_3 = k_3,\ M^\sigma \to \infty,\ M^\tau \to \infty$$

However, **F1** is not the only critical point that controls all the critical phenomena of the phase diagram. For instance, one can also find that except flowing to the fixed point **F1**, fixed point **F2** also flows toward the direction $M_3^\tau \to \infty$, and thus approach to:

$$(\mathbf{F5}):\ y_1 = 0,\ y_2 = \frac{\sqrt{\epsilon}}{2},\ y_3 = 0,\ K_1 = K_3 = k,\ K_2 = 0,\ M_2^\sigma = 1,\ M_3^\tau \to \infty$$

For the **F5**, except the β function dM^τ/dl, other β functions remain zero. As a result, **F5** corresponds to a fixed point at the large M^τ regime. By study the nearby RG trajectory through the matrix W in Eq. (C.38), one can conclude that fixed point **F5** is actually a generic critical point, and flows toward either the spin and orbital KD phase **G**, or an orbital KS phase:

$$(\mathbf{S2}):\ y_2 \to \infty,\ y_1 = y_3 = 0,\ K_2 = 0,\ K_1 = K_3 = k_\tau,\ M^\sigma = 0,\ M^\tau \to \infty$$

Similarly, there is another fixed point

$$(\mathbf{F6}):\ y_1 = 0,\ y_2 = 0,\ y_3 = \frac{\sqrt{\epsilon}}{2},\ K_1 = K_2 = k,\ K_3 = 0,\ M^\sigma = 0,\ M^\tau \to \infty$$

which flows to either the spin and orbital KD phase **G**, or a spin KS strong coupling fixed point:

$$(\mathbf{S3}):\ y_3 \to \infty,\ y_1 = y_2 = 0,\ K_3 = 0,\ K_1 = K_2 = k_\tau,\ M^\sigma \to \infty,\ M^\tau = 0$$

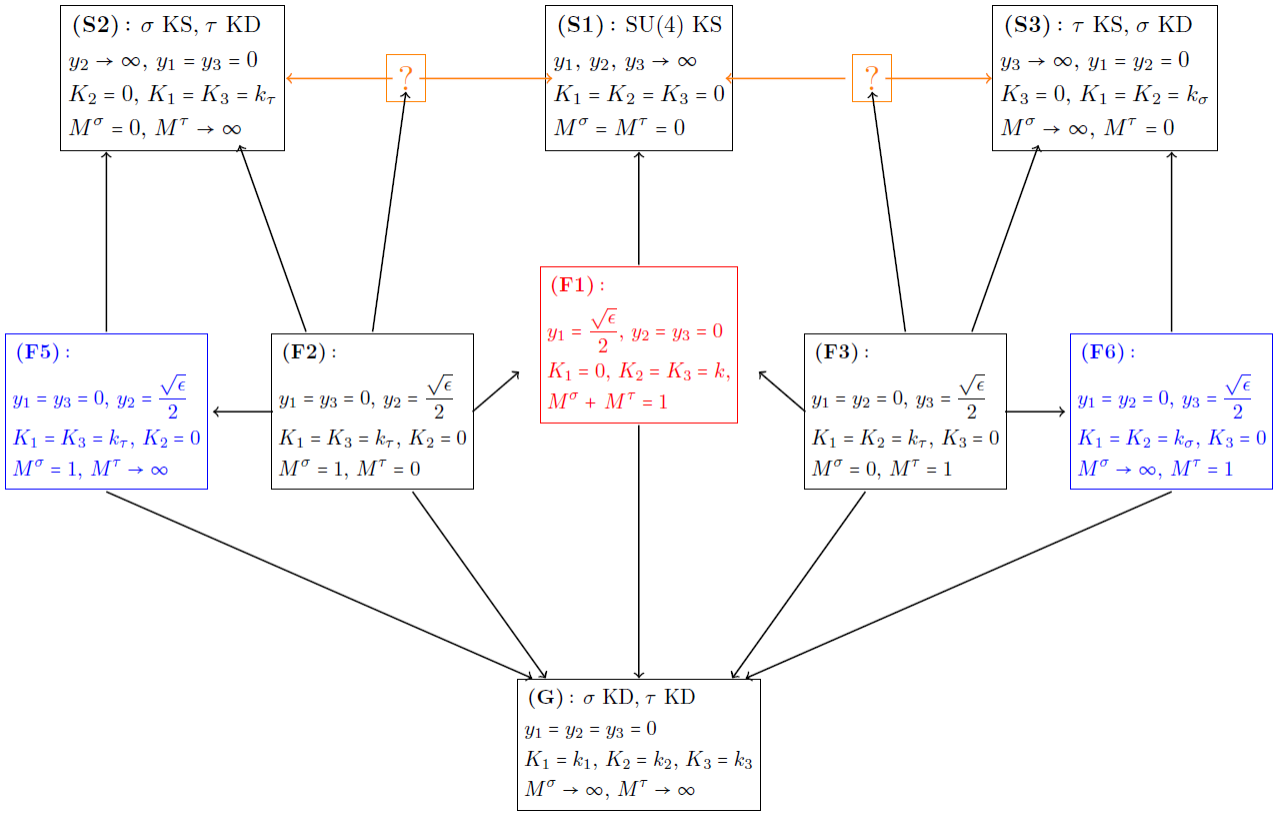

Figure C.1 : The schematic fixed points structure and their relative RG flow of BFK model (5.8) based on the β functions (C.37). Here KS and KD is the abbreviation for the Kondo-screened and the Kondo-destroyed, respectively. The three boxes on the top are the different kinds of strong Kondo coupling fixed points, which should be all stable according to the β functions (C.37). The middle five are the different fixed points in the order of ϵ, where **F1**, **F5** and **F6** are the generic critical points corresponding to different kinds of phase transitions. The bottom box is a completely Kondo-destroyed phase. Since the critical points can flow toward the different types of strong Kondo coupling fixed points **S1**, **S2**, and **S1**, there should be some critical points(denoted as orange boxes here) separating these strong Kondo coupling fixed points.

The stability of the strong coupling fixed points $S1$, $S2$, and $S3$ can be explored through the matrix W (C.38), which indicates that they are stable against other small perturbations. Hence, there should be other strong coupling critical points separating them. The whole RG flow structure is summarized in Fig. C.1, where the orange boxes denote the strong coupling critical points separating stable strong Kondo coupling fixed points. We also neglect the fixed **F4** since it is the most unstable fixed point and thus does not affect the RG structure at all.

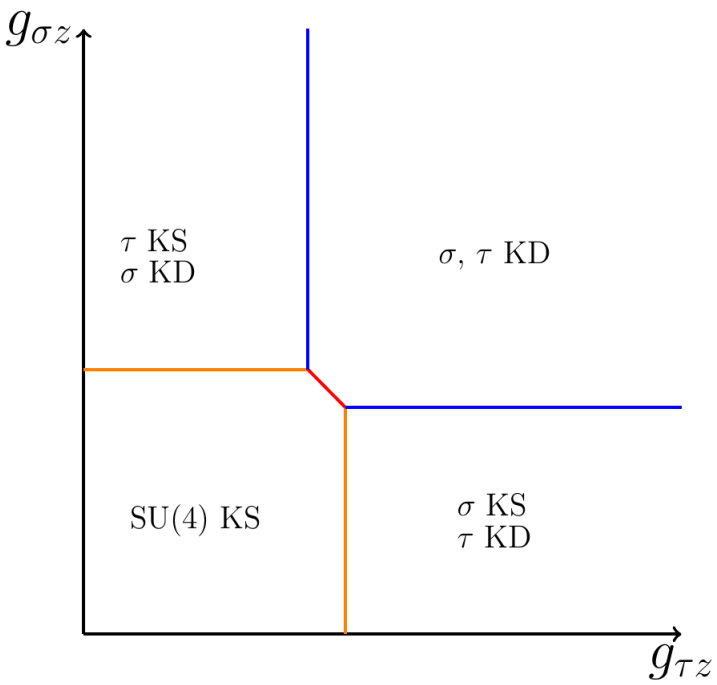

Figure C.2 : The generic phase diagram with arbitrary Kondo couplings based on the RG flow structure Fig. C.1. The critical properties across each blue lines, the red line, and orange lines are controlled by a specific critical points in the blue, red, and orange boxes in Fig. C.1, respectively.

From to the RG flow structure Fig.C.1, one can see that the spin and orbital KD phase **G** can transit to different kinds of strong Kondo coupling fixed points **S1**, **S2**, and **S3**. There are three distinct types of trajectory path, and the associated critical

phenomena are controlled by different generic critical points **F1**, **F5**, and **F6**. Based on these results, the generic phase diagram is shown in Fig. C.2*.

In the following, we are going to elaborate these results in a more transparent and visible way.

C.2.2 Transition to the SU(4) Kondo-screened phase

To illustrate the transition between the spin and orbital KD phase to the SU(4) KS phase, we choose to scan the RG flow structure by taking $g_{\sigma z} = g_{\tau z} = g$, which corresponds to the trajectory denoted as dashed arrow in Fig. 5.8.

Since along this direction, the β functions (C.37) are invariant under $\sigma \leftrightarrow \tau$, one can set $y_2 = y_3 = y$ and $K_2 = K_3 = K$. The β functions (C.37) thus can be reduced to:

$$\begin{aligned}
\frac{dy_1}{dl} &= (1 - K_1 - 2M)\, y_1 + 2y^2 \\
\frac{dy}{dl} &= (1 - K - M)\, y + 2y_1 y \\
\frac{dK_1}{dl} &= -2y_1^2\,(2K_1) - 4y^2\,(K_1) \\
\frac{dK}{dl} &= -2y_1^2\,(K_1) - 4y^2\,(2K) + 2y^2\,(K_1) \\
\frac{dM}{dl} &= \left(\epsilon - 4y_1^2 - 4y^2\right) M
\end{aligned} \tag{C.39}$$

One can see that the coupling constant K_1 flows to 0 no matter the initial values,

*Here the term "generic" means that we choose arbitrary $J_{\sigma z}$, $J_{\tau z}$,$J_{\sigma\perp}$,$J_{\tau\perp}$, J_{M_1}, J_{M_4}, and then keep them fixed while varying $g_{\sigma z}$ and $g_{\tau z}$.

and thus the β functions can be further reduced into:

$$\begin{aligned}
\frac{dy_1}{dl} &= (1-2M)\, y_1 + 2y^2 \\
\frac{dy}{dl} &= (1-K-M)\, y + 2y_1 y \\
\frac{dK}{dl} &= -2y_1^2\,(K_1) - 4y^2\,(2K) \\
\frac{dM}{dl} &= \left(\epsilon - 4y_1^2 - 4y^2\right) M
\end{aligned} \tag{C.40}$$

and again, $K \to 0$ no matter the initial values, so in the end we derive the reduced β functions Eq. (5.15):

$$\begin{aligned}
\frac{dy_1}{dl} &= (1-2M)\, y_1 + 2y^2 \\
\frac{dy}{dl} &= (1-M)\, y + 2y_1 y \\
\frac{dM}{dl} &= \left(\epsilon - 4y_1^2 - 4y^2\right) M
\end{aligned} \tag{C.41}$$

By these reduced β functions (C.41), one identify a critical point $(y_1^*, y^*, M^*) = \left(\frac{\sqrt{\epsilon}}{2}, 0, \frac{1}{2}\right)$. This critical point actually corresponds to the critical point **F1** in Fig. C.1, and separates the spin and orbital KD phase from the SU(4) KS phase.

C.2.3 Transition to spin or orbital Kondo-screened phase

Here we aim to illustrate the transition between the spin and orbital KD phase and the spin or orbital KS phase. We scan the RG flow by taking the $g_{\sigma z} \to \infty$ and vary the $g_{\tau z}$, which corresponds to the dashed arrow lines in Fig. 5.10. Under this condition, according to the β functions (C.37), y_1 and y_3 must both flow to 0, and

both are irrelevant. The β functions can thus be reduced into:

$$\begin{aligned}
\frac{dy_2}{dl} &= (1 - K_2 - M^\sigma)\, y_2 \\
\frac{dK_1}{dl} &= -2y_2^2\,(K_1 + K_2 - K_3) \\
\frac{dK_2}{dl} &= -2y_2^2\,(2K_2) \\
\frac{dK_3}{dl} &= -2y_2^2\,(K_3 + K_2 - K_1) \\
\frac{dM^\sigma}{dl} &= \left(\epsilon - 4y_2^2\right) M^\sigma
\end{aligned} \tag{C.42}$$

by which one can see that $K_2 \to 0$, and again the β functions can be further reduced into:

$$\begin{aligned}
\frac{dy_2}{dl} &= (1 - M^\sigma)\, y_2 \\
\frac{dK_1}{dl} &= -2y_2^2\,(K_1 - K_3) \\
\frac{dK_3}{dl} &= -2y_2^2\,(K_3 - K_1) \\
\frac{dM^\sigma}{dl} &= \left(\epsilon - 4y_2^2\right) M^\sigma
\end{aligned} \tag{C.43}$$

From the reduced β functions (C.43), one can immediately conclude that the K_1 and K_3 flow to the fixed point $K_1 = K_3 = k_\tau$, where k_τ is a constant. As a result, the final reduced β functions are indeed Eq. (5.16).

By these reduced β functions (C.43), One can find a critical point $(y_2^*, M^{\sigma *}) = \left(\frac{\sqrt{\epsilon}}{2}, 1\right)$, which corresponds to the fixed point **F5** in Fig. C.1 and separates the spin and orbital KD phase from the spin KS phase.

Appendix D

Appendix of Chapter 6

D.1 Ginzburg-Lanbdau theory

We start from the Ginzburg-Landau description for the magnetism in iron pnictides, Eq. (1) of the main text. After performing the Hubbard-Stranovich transformation to the quartic term S_4 in the action of Eq. (1), the resulting action is:

$$\begin{aligned} S_0 &= S_{2,\vec{m},\Delta,\eta} + S_{3,\vec{m},\Delta,\eta} \\ S_{2,\vec{m},\Delta,\eta} &= \sum_{q=\vec{q},i\omega_n} \Big\{ \chi_0^{-1}(q) \left(|\vec{m}_A(q)|^2 + |\vec{m}_B(q)|^2 \right) \\ &+ \Delta(q) \chi_\Delta^{-1}(q) \Delta(-q) + \frac{-1}{4u_1} \Big(i\eta(q) - r \Big) \Big(i\eta(-q) - r \Big) \Big\} \\ S_{3,\vec{m},\Delta,\eta} &= \int_0^\beta d\tau \int d^2x \left[2\Delta \vec{m}_A \cdot \vec{m}_B + 2i\eta \left(\vec{m}_A^2 + \vec{m}_B^2 \right) \right] \end{aligned} \tag{D.1}$$

The field Δ is the Ising-nematic order parameter field because it is the conjugate to the bilinear $\vec{m}_A \cdot \vec{m}_B$, which changes sign under the transformation $\vec{m}_A \to \pm \vec{m}_A, \vec{m}_B \to \mp \vec{m}_B$. The field η is the conjugate of $\vec{m}_A^2 + \vec{m}_B^2$. The nematic propagator χ_Δ will have the form

$$\chi_\Delta^{-1}(\vec{q}, i\omega_n) = \frac{1}{u_I} - \Pi_\Delta(\vec{q}, i\omega_n) \ . \tag{D.2}$$

The constant term $\frac{1}{u_I}$ comes from the Hubbard-Stratonovich transformation of the quartic term in Eq. (1), while $\Pi(\vec{q}, i\omega)$ will come from integrating out high energy $\vec{m}_A$ and $\vec{m}_B$ fields as well as background coherent-fermion fields.

D.2 nematicity and the Spin excitation anisotropy

The spin excitation anisotropy $\chi_d(\omega)$ and the dynamical magnetic susceptibility $\chi_s(\omega)$ is defined as:

$$\chi_s(\omega) \equiv \chi\left(\vec{Q}_1, \omega\right) + \chi\left(\vec{Q}_2, \omega\right) \tag{D.3}$$

$$\chi_d(\omega) \equiv \chi\left(\vec{Q}_1, \omega\right) - \chi\left(\vec{Q}_2, \omega\right) \tag{D.4}$$

where $\vec{Q}_1 = (\pi, 0)$ and $\vec{Q}_2 = (0, \pi)$ are ordering wave vectors, and the dynamical spin susceptibility $\chi(\vec{q}, \omega)$ is:

$$\begin{aligned} &\chi(\vec{q}, \omega) = \\ &\int d^2r' \int d^2r \int d\tau e^{-i\vec{q}\cdot(\vec{r}'-\vec{r})-i\omega\tau} \langle T_\tau \vec{S}(\vec{r}, \tau) \cdot \vec{S}^*(\vec{r}', 0)\rangle_S \end{aligned} \tag{D.5}$$

and $\vec{S}(\vec{r}, \tau)$ is the local spin operator.

In order to measure spin excitation anisotropy $\chi_d(\omega)$, an small external uniaxial stress is necessary to detwin the sample. Therefore, the expectation $\langle T_\tau \vec{S}(\vec{r}, \tau) \cdot \vec{S}^*(\vec{r}', 0)\rangle_S$ in Eq.(D.5) is calculated under the action $S = S_0 + S_{\lambda,\Delta}$ in Eq. (2) of the main text.

Our next step is to express the dynamical magnetic susceptibility $\chi_s(\omega)$ and the spin excitation anisotropy $\chi_d(\omega)$ in term of the magnetic order parameter fields $\vec{m}_A$, $\vec{m}_B$, and the nematic order parameter field Δ. To do so, we just need to recognize that in iron pnictides, the local spin operator field $\vec{S}(\vec{r}, \tau)$ can be represented as $\vec{S}(\vec{r}, \tau) = \vec{m}_1(\vec{r}, \tau) e^{i\vec{Q}_1\cdot\vec{r}} + \vec{m}_2(\vec{r}, \tau) e^{i\vec{Q}_2\cdot\vec{r}}$, where $\vec{m}_1(\vec{r}, \tau) = (\vec{m}_A(\vec{r}, \tau) - \vec{m}_B(\vec{r}, \tau))/2$ and $\vec{m}_2(\vec{r}, \tau) = (\vec{m}_A(\vec{r}, \tau) + \vec{m}_B(\vec{r}, \tau))/2$, is the magnetic order parameter associated with ordering wave vector $\vec{Q}_1$ and $\vec{Q}_2$, respectively. We can then express the spin excitation anisotropy $\chi_d(\omega)$ and dynamical magnetic susceptibility $\chi_s(\omega)$ in terms of

the magnetic order parameter fields $\vec{m}_A$ and $\vec{m}_B$:

$$\begin{aligned}
&\chi_d(\omega) \equiv \chi\left(\vec{Q}_1, \omega\right) - \chi\left(\vec{Q}_2, \omega\right) \\
&= -\frac{1}{2}\int d\tau e^{-i\omega\tau}\langle T_\tau \vec{m}_A(\vec{q}=0,\tau)\cdot\vec{m}_B(\vec{q}'=0,\tau'=0)\rangle_S \\
&-\frac{1}{2}\int d\tau e^{-i\omega\tau}\langle T_\tau \vec{m}_B(\vec{q}=0,\tau)\cdot\vec{m}_A(\vec{q}'=0,\tau'=0)\rangle_S \\
&= -\int d\tau e^{-i\omega\tau}\langle T_\tau \vec{m}_A(\vec{q}=0,\tau)\cdot\vec{m}_B(\vec{q}'=0,\tau'=0)\rangle_S
\end{aligned} \tag{D.6}$$

and

$$\begin{aligned}
&\chi_s(\omega) \equiv \chi\left(\vec{Q}_1, \omega\right) + \chi\left(\vec{Q}_2, \omega\right) \\
&= \frac{1}{2}\int d\tau e^{-i\omega\tau}\langle T_\tau \vec{m}_A(\vec{q}=0,\tau)\cdot\vec{m}_A(\vec{q}'=0,\tau'=0)\rangle_S \\
&+\frac{1}{2}\int d\tau e^{-i\omega\tau}\langle T_\tau \vec{m}_B(\vec{q}=0,\tau)\cdot\vec{m}_B(\vec{q}'=0,\tau'=0)\rangle_S \\
&= \int d\tau e^{-i\omega\tau}\langle T_\tau \vec{m}_{A/B}(\vec{q}=0,\tau)\cdot\vec{m}_{A/B}(\vec{q}'=0,\tau'=0)\rangle_S
\end{aligned} \tag{D.7}$$

Here, the last equality for both Eq. (D.6) and Eq. (D.7) hold since the the model (2) of the main text respect the symmetry $\vec{m}_A \leftrightarrow \vec{m}_B$, and there is no condensation of the $\langle \vec{m}_A^2 - \vec{m}_B^2 \rangle$. We also neglected the terms such as $\langle \vec{m}_A\left(\vec{Q}_2 - \vec{Q}_1, \omega\right)\vec{m}_B\left(-\left(\vec{Q}_2 - \vec{Q}_1\right), -\omega\right)\rangle$. Because $|\vec{Q}_1 - \vec{Q}_2| \approx \Lambda$, where Λ is the momentum cut-off of the theory, such term can only be generated by very severe spatial fluctuations which had already been coarse-grained in the construction of the starting Ginzburg-Landau description (1) of the main text.

The expectation values in Eqs. (D.6) and (D.7) are calculated under the action $S = S_0 + S_{\lambda,\Delta}$. Now we treat the uniaxial strain $S_{\lambda,\Delta}$ as a perturbation and expand the action with respect to S_0:

$$\begin{aligned}
&\langle T_\tau \vec{m}_A(0,\tau)\cdot\vec{m}_A(0,0)\rangle_{S_0+S_{\lambda,\Delta}} = \langle T_\tau \vec{m}_A(0,\tau)\cdot\vec{m}_A(0,0)\rangle_{S_0} \\
&-\lambda\int d\tau' \langle T_\tau \vec{m}_A(0,\tau)\cdot\vec{m}_A(0,0)\,\Delta(0,\tau')\rangle_{S_0} + O\left(\lambda^2\right) \\
&= \langle T_\tau \vec{m}_A(0,\tau)\cdot\vec{m}_A(0,0)\rangle_{S_0} + O\left(\lambda^2\right) \\
&= \int d\omega' e^{i\omega'\tau}\overline{\chi}_{m_A}(0,\omega') + O\left(\lambda^2\right)
\end{aligned} \tag{D.8}$$

We have used $\langle T_\tau \vec{m}_A(0,\tau)\,\vec{m}_A(0,0)\,\Delta(0,\tau')\rangle_{S_0} = 0$, and the fact that $\overline{\chi}_{m_A}(\vec{q},\omega')$ is the magnetic propagator in the momentum space. Following Eq. (D.7) and Eq. (D.8), we have:

$$\chi_s(\omega) = \overline{\chi}_{m_{A/B}}(0,\omega) = \overline{\chi}_m(0,\omega) \tag{D.9}$$

where $\overline{\chi}_{m_A}(0,\omega) = \overline{\chi}_{m_B}(0,\omega)$ because of the symmetry $\vec{m}_A \leftrightarrow \vec{m}_B$ respected by the action (2) of the main text. We have defined $\overline{\chi}_m(0,\omega) \equiv \overline{\chi}_{m_A}(0,\omega) = \overline{\chi}_{m_B}(0,\omega)$.

We see that $\chi_s(\omega)$ is just the dynamical magnetic propagator $\overline{\chi}_m(0,\omega)$. Similarly, for the spin excitation anisotropy $\chi_d(\omega)$:

$$\begin{aligned}
&\langle T_\tau \vec{m}_A(0,\tau)\cdot\vec{m}_B(0,0)\rangle_{S_0+S_{\lambda,\Delta}} = \langle T_\tau \vec{m}_A(0,\tau)\cdot\vec{m}_B(0,0)\rangle_{S_0} \\
&-\lambda\int d\tau' \langle \vec{m}_A(0,\tau)\cdot\vec{m}_B(0,0)\,\Delta(0,\tau')\rangle_{S_0} + O\left(\lambda^2\right) \\
&= -\lambda\int d\tau' \langle T_\tau \vec{m}_A(0,\tau)\cdot\vec{m}_B(0,0)\,\Delta(0,\tau')\rangle_{S_0} + O\left(\lambda^2\right)
\end{aligned} \tag{D.10}$$

where $\langle T_\tau \vec{m}_A(0,\tau)\cdot\vec{m}_B(0,0)\rangle_{S_0} \propto \langle\Delta\rangle_{S_0}\delta_{\tau,0}$ vanishes when temperature $T > T_S$, the nematic phase transition temperature, or $T < T_S$ but near the critical point at which $\langle\Delta\rangle_{S_0} \to 0$. Since in this work, we focus on the quantum critical region, we can safely discard this term.

On the other hand, since any three-point correlation function can always be factorized as the product of suitable irreducible two-point correlation function and irre-

ducible vertex function[164, 165, 166], we have:

$$\begin{aligned}&\int d\tau' \langle T_\tau \vec{m}_A(0,\tau)\cdot\vec{m}_B(0,0)\,\Delta(0,\tau')\rangle_{S_0} = \\ &\int d\omega' e^{i\omega'\tau}\overline{V}(0,\omega')\,\overline{\chi}_{m_A}(0,\omega')\,\overline{\chi}_{\Delta}(0,0)\,\overline{\chi}_{m_B}(0,-\omega')\end{aligned} \tag{D.11}$$

As a result, we conclude:

$$\begin{aligned}&\chi_d(\omega) \equiv \chi\left(\vec{Q}_1,\omega\right) - \chi\left(\vec{Q}_2,\omega\right) \\ &= \lambda\overline{V}(0,\omega)\,\overline{\chi}_{m_A}(0,\omega)\,\overline{\chi}_{\Delta}(0,0)\,\overline{\chi}_{m_B}(0,-\omega) + O\left(\lambda^2\right) \\ &= \lambda\overline{V}(0,\omega)\,\overline{\chi}_{m}^2(0,\omega)\,\overline{\chi}_{\Delta}(0,0) + O\left(\lambda^2\right)\end{aligned} \tag{D.12}$$

where the $\overline{\chi}_\Delta$ is the nematic propagator, and $\overline{V}$ is the vertex function involving two external magnetic order parameter fields $\vec{m}_A$ and $\vec{m}_B$, and one nematic order parameter field Δ. Again, we use $\overline{\chi}_{m_A}(0,\omega) = \overline{\chi}_{m_B}(0,\omega) = \overline{\chi}_m(0,\omega)$. Because of the time reversal symmetry, we also have $\overline{\chi}_m(0,\omega) = \overline{\chi}_m(0,-\omega)$

Note that when we derive the identities (D.9) and (D.12), we only expand the uniaxial strain term $S_{\lambda,\Delta}$ perturbatively. Therefore, both the identities (D.9) and (D.12) are valid non-perturbatively as far as S_0 is concerned.

D.3 Scaling analysis of spin excitation anisotropy with non-zero anomalous dimension

In this section, we carry through the scaling analysis of the spin excitation anisotropy $\chi_d(\omega)$ and dynamical magnetic susceptibility $\chi_s(\omega)$ with a non-zero anomalous dimension η for the magnetic order parameter field $\vec{m}$. The scaling dimension of the magnetic order parameter field is:

$$d_m = -\frac{D+z+2-\eta}{2} \tag{D.13}$$

with $\eta \neq 0$.

Following a procedure similar to that presented in the main text, in the quantum critical regime the frequency dependence of the magnetic propagator is:

$$\overline{\chi}_m(0,\omega) = \chi_s(\omega) \sim \omega^{-\frac{2-\eta}{z}} \tag{D.14}$$

and the frequency dependence of the vertex function is:

$$\overline{V}(0,\omega) \sim \omega^{\frac{(2-\eta)-d_\Delta-(D+z)}{z}} \tag{D.15}$$

Consequently, by the identity Eq. (D.12), the spin excitation anisotropy is:

$$\chi_d(\omega) \sim \omega^{\frac{-(2-\eta)-d_\Delta-(D+z)}{z}} \tag{D.16}$$

Therefore, with the knowledge of the anomalous dimension η, again we can detect the dynamical exponent z and the scaling dimension of the nematic order parameter d_Δ by measuring the dynamical nematic susceptibility $\chi_s(\omega)$ and the spin excitation anisotropy $\chi_d(\omega)$ according to:

$$\begin{aligned} \frac{-(2-\eta)}{z} &= \frac{\partial \ln \chi_s(\omega)}{\partial \ln \omega} \\ \frac{-d_\Delta-(D+z)-(2-\eta)}{z} &= \frac{\partial \ln \chi_d(\omega)}{\partial \ln \omega} \end{aligned} \tag{D.17}$$

For the singular energy dependence of the spin excitation anisotropy and the dynamical magnetic susceptibility observed in the Ni-doped $BaFe_2As_2$ near optimal doping, if anomalous dimension $\eta \neq 0$, again the relation (20) in the main text implies that:

$$\overline{V}(0,\omega) \sim \frac{\chi_d(\omega)}{\overline{\chi}_m^2(0,\omega)} \sim \omega^0 \tag{D.18}$$

and thus following Eq. (D.15):

$$d_\Delta = 2 - \eta - D - z \tag{D.19}$$

Again, to see what this implies for the nematic degree of freedom, let's consider the nematic propagator to take a general form in the quantum critical regime:

$$\overline{\chi}_{\Delta}^{-1}(q,\omega) = b_1 q^n + b_2 \frac{|\omega|}{q^a} \tag{D.20}$$

by which we then know:

$$z = n + a \tag{D.21}$$

and

$$d_{\Delta} = -\frac{D+z+n}{2} = -\frac{D+2n+a}{2} \tag{D.22}$$

Compare it with Eq. (D.19), it is straightforward to show that:

$$a = 4 - D - 2\eta = 2 - 2\eta \tag{D.23}$$

Bibliography

[1] Q. Si, "Global magnetic phase diagram and local quantum criticality in heavy fermion metals," *Physica B: Condensed Matter*, vol. 378, pp. 23–27, 2006.

[2] Q. Si, "Quantum criticality and global phase diagram of magnetic heavy fermions," *Physica Status Solidi (B) Basic Research*, vol. 247, pp. 476–484, 2010.

[3] H. v. Löhneysen, A. Rosch, M. Vojta, and P. Wölfle, "Fermi-liquid instabilities at magnetic quantum phase transitions," *Rev. Mod. Phys.*, vol. 79, pp. 1015–1075, Aug 2007.

[4] P. Coleman, "Heavy fermions: Electrons at the edge of magnetism," *Handbook of Magnetism and Advanced Magnetic Materials*, 2007.

[5] P. Lee, T. Rice, J. Serene, L. Sham, and J. Wilkins, "Theories of heavy-electron systems," *Comments on Condensed Matter Physics*, vol. 12, no. 3, pp. 99–161, 1986.

[6] N. Tsujii, H. Kontani, and K. Yoshimura, "Universality in heavy fermion systems with general degeneracy," *Phys. Rev. Lett.*, vol. 94, p. 057201, Feb 2005.

[7] Q. Si, "Iron pnictide superconductors: Electrons on the verge," *Nature Physics*, vol. 5, p. 629–630, 2009.

[8] M. M. Qazilbash, J. J. Hamlin, R. E. Baumbach, L. Zhang, D. J. Singh, M. B. Maple, and D. N. Basov, "Electronic correlations in the iron pnictides," *Nature Physics*, vol. 5, p. 647–650, 2009.

[9] E. Abrahams and Q. Si, "Quantum criticality in the iron pnictides and chalcogenides," *Journal of Physics Condensed Matter*, vol. 23, p. 223201, 2011.

[10] J. Wu, Q. Si, and E. Abrahams, "Magnetic and ising quantum phase transitions in a model for isoelectronically tuned iron pnictides," *Phys. Rev. B*, vol. 93, p. 104515, Mar 2016.

[11] H. Ono, T. Nakano, N. Takeda, G. Ano, M. Akatsu, Y. Nemoto, T. Goto, A. Dönni, and H. Kitazawa, "Magnetic phase diagram of clathrate compound $ce_3pd_{20}si_6$ with quadrupolar ordering," *J. Phys.: Condens. Matter*, vol. 25, no. 12, p. 126003, 2013.

[12] V. Martelli, A. Cai, E. Nica, M. Taupin, A. Prokofiev, C.-C. Liu, H.-H. Lai, R. Yu, R. Küchler, A. Strydom, *et al.*, "Sequential localization and strange-metal behavior of a complex electron fluid," *arXiv preprint arXiv:1709.09376*, 2017.

[13] V. Martelli, A. Cai, E. M. Nica, M. Taupin, A. Prokofiev, C.-C. Liu, H.-H. Lai, R. Yu, K. Ingersent, R. Küchler, A. M. Strydom, D. Geiger, J. Haenel, J. Larrea, Q. Si, and S. Paschen, "Sequential localization of a complex electron fluid," *Proceedings of the National Academy of Sciences*, vol. 116, no. 36, pp. 17701–17706, 2019.

[14] Y. Song, X. Lu, D. L. Abernathy, D. W. Tam, J. L. Niedziela, W. Tian, H. Luo, Q. Si, and P. Dai, "Energy dependence of the spin excitation anisotropy in

uniaxial-strained $bafe_{1.9}ni_{0.1}as_2$," *Phys. Rev. B*, vol. 92, p. 180504, Nov 2015.

[15] K. G. Wilson, "The renormalization group and critical phenomena," *Rev. Mod. Phys.*, vol. 55, pp. 583–600, Jul 1983.

[16] J. Cardy, *Scaling and renormalization in statistical physics*. Cambridge University Press, 2015.

[17] N. Goldenfeld, *Lectures on phase transitions and the renormalization group*. CRC Press, 2018.

[18] S. L. Sondhi, S. M. Girvin, J. P. Carini, and D. Shahar, "Continuous quantum phase transitions," *Rev. Mod. Phys.*, vol. 69, pp. 315–333, Jan 1997.

[19] M. Vojta, "Quantum phase transitions," *Reports on Progress in Physics*, 2003.

[20] S. Sachdev, *Quantum Phase Transitions*. Cambridge University Press, 2011.

[21] S. Sachdev and B. Keimer, "Quantum criticality," *Physics Today*, vol. 64, p. 29, 2011.

[22] P. Coleman and A. J. Schofield, "Quantum criticality," *Nature*, vol. 433, p. 226–229, 2005.

[23] S. Kirchner, S. Paschen, Q. Chen, S. Wirth, D. Feng, J. D. Thompson, and Q. Si, "Colloquium: Heavy-electron quantum criticality and single-particle spectroscopy," *Rev. Mod. Phys.*, vol. 92, p. 011002, Mar 2020.

[24] G. Baym and C. Pethick, *Landau Fermi-Liquid Theory: Concepts and Applications*. Wiley-VCH, 2007.

[25] N. F. Mott, "Metal-insulator transition," *Rev. Mod. Phys.*, vol. 40, pp. 677–683, Oct 1968.

[26] M. R. Norman, D. Pines, and C. Kallin, "The pseudogap: friend or foe of high t_c ?," *Advances in Physics*, vol. 54, no. 8, pp. 715–733, 2005.

[27] R. A. Cooper, Y. Wang, B. Vignolle, O. J. Lipscombe, S. M. Hayden, Y. Tanabe, T. Adachi, Y. Koike, M. Nohara, H. Takagi, C. Proust, and N. E. Hussey, "Anomalous criticality in the electrical resistivity of la2–xsrxcuo4," *Science*, vol. 323, no. 5914, pp. 603–607, 2009.

[28] P. Gegenwart, Q. Si, and F. Steglich, "Quantum criticality in heavy fermion metals," *Nature Physics*, vol. 4, pp. 186–197, 2008.

[29] Q. Si, R. Yu, and E. Abrahams, "High-temperature superconductivity in iron pnictides and chalcogenides," *Nature Reviews Materials*, vol. 1, no. 4, p. 16017, 2016.

[30] P. Coleman and A. H. Nevidomskyy, "Frustration and the kondo effect in heavy fermion materials," *Journal of Low Temperature Physics*, vol. 161, p. 182–202, 2010.

[31] L. Fu, S. Sachdev, and C. Xu, "Geometric phases and competing orders in two dimensions," *Phys. Rev. B*, vol. 83, p. 165123, Apr 2011.

[32] P. Goswami and Q. Si, "Topological defects of néel order and kondo singlet formation for the kondo-heisenberg model on a honeycomb lattice," *Phys. Rev. B*, vol. 89, p. 045124, Jan 2014.

[33] C.-C. Liu, P. Goswami, and Q. Si, "Skyrmion defects and competing singlet orders in a half-filled antiferromagnetic kondo-heisenberg model on the honeycomb lattice," *Phys. Rev. B*, vol. 96, p. 125101, Sep 2017.

[34] H. Zhao, J. Zhang, M. Lyu, S. Bachus, Y. Tokiwa, P. Gegenwart, S. Zhang, J. Cheng, Y. feng Yang, G. Chen, Y. Isikawa, Q. Si, F. Steglich, and P. Sun, "Quantum-critical phase out of frustrated magnetism in a strongly correlated metal," *Nature Physics*, vol. 15, p. 1261–1266, 2019.

[35] C.-C. Liu, E. Abrahams, and Q. Si, "Quantum critical nematic fluctuations and spin excitation anisotropy in iron pnictides," *Arxiv:1910.14597*, 2019.

[36] L. P. Kadanoff, "Scaling laws for ising models near T_c," *Physics Physique Fizika*, vol. 2, pp. 263–272, Jun 1966.

[37] M. Kardar, *Statistical Physics of Fields*. Cambridge University Press, 2007.

[38] J. A. Hertz, "Quantum critical phenomena," *Phys. Rev. B*, vol. 14, pp. 1165–1184, Aug 1976.

[39] A. J. Millis, "Effect of a nonzero temperature on quantum critical points in itinerant fermion systems," *Phys. Rev. B*, vol. 48, pp. 7183–7196, Sep 1993.

[40] J. Hubbard, "Electron correlations in narrow energy bands," *Proceedings of the Royal Society of London. Series A, Mathematical and Physical Sciences*, vol. 276, no. 1365, pp. 238–257, 1963.

[41] D. Belitz, T. R. Kirkpatrick, and T. Vojta, "Nonanalytic behavior of the spin susceptibility in clean fermi systems," *Phys. Rev. B*, vol. 55, pp. 9452–9462, Apr 1997.

[42] A. Abanov and A. Chubukov, "Anomalous scaling at the quantum critical point in itinerant antiferromagnets," *Phys. Rev. Lett.*, vol. 93, p. 255702, Dec 2004.

[43] A. V. Chubukov, C. Pépin, and J. Rech, "Instability of the quantum-critical point of itinerant ferromagnets," *Phys. Rev. Lett.*, vol. 92, p. 147003, Apr 2004.

[44] P. W. Anderson, "Antiferromagnetism. theory of superexchange interaction," *Phys. Rev.*, vol. 79, pp. 350–356, Jul 1950.

[45] F. D. M. Haldane, "Nonlinear field theory of large-spin heisenberg antiferromagnets: Semiclassically quantized solitons of the one-dimensional easy-axis néel state," *Phys. Rev. Lett.*, vol. 50, pp. 1153–1156, Apr 1983.

[46] F. D. M. Haldane, "Continuum dynamics of the 1-d heisenberg antiferromagnet: Identification with the o(3) nonlinear sigma model," *Physics Letters A*, vol. 93, pp. 464–468, Feb 1983.

[47] E. Brézin and J. Zinn-Justin, "Renormalization of the nonlinear σ model in $2+\epsilon$ dimensions—application to the heisenberg ferromagnets," *Phys. Rev. Lett.*, vol. 36, pp. 691–694, Mar 1976.

[48] E. Brézin and J. Zinn-Justin, "Spontaneous breakdown of continuous symmetries near two dimensions," *Phys. Rev. B*, vol. 14, pp. 3110–3120, Oct 1976.

[49] D. R. Nelson and R. A. Pelcovits, "Momentum-shell recursion relations, anisotropic spins, and liquid crystals in $2+\epsilon$ dimensions," *Phys. Rev. B*, vol. 16, pp. 2191–2199, Sep 1977.

[50] S. Chakravarty, B. I. Halperin, and D. R. Nelson, "Two-dimensional quantum heisenberg antiferromagnet at low temperatures," *Phys. Rev. B*, vol. 39,

pp. 2344–2371, Feb 1989.

[51] A. M. Polyakov, "Interaction of goldstone particles in two dimensions. applications to ferromagnets and massive yang-mills fields," *Physics Letters B*, vol. 59, pp. 79–81, Oct 1975.

[52] F. D. M. Haldane, "O(3) nonlinear σ model and the topological distinction between integer- and half-integer-spin antiferromagnets in two dimensions," *Phys. Rev. Lett.*, vol. 61, pp. 1029–1032, Aug 1988.

[53] N. Read and S. Sachdev, "Valence-bond and spin-peierls ground states of low-dimensional quantum antiferromagnets," *Phys. Rev. Lett.*, vol. 62, pp. 1694–1697, Apr 1989.

[54] N. Read and S. Sachdev, "Spin-peierls, valence-bond solid, and néel ground states of low-dimensional quantum antiferromagnets," *Phys. Rev. B*, vol. 42, pp. 4568–4589, Sep 1990.

[55] T. Senthil, L. Balents, S. Sachdev, A. Vishwanath, and M. P. A. Fisher, "Quantum criticality beyond the landau-ginzburg-wilson paradigm," *Phys. Rev. B*, vol. 70, p. 144407, Oct 2004.

[56] T. Senthil, A. Vishwanath, L. Balents, S. Sachdev, and M. P. A. Fisher, "Deconfined quantum critical points," *Science*, vol. 303, no. 5663, pp. 1490–1494, 2004.

[57] M. A. Ruderman and C. Kittel, "Indirect exchange coupling of nuclear magnetic moments by conduction electrons," *Phys. Rev.*, vol. 96, pp. 99–102, Oct 1954.

[58] T. Kasuya, "A Theory of Metallic Ferro- and Antiferromagnetism on Zener's Model," *Progress of Theoretical Physics*, vol. 16, pp. 45–57, 07 1956.

[59] K. Yosida, "Magnetic properties of cu-mn alloys," *Phys. Rev.*, vol. 106, pp. 893–898, Jun 1957.

[60] A. A. Abrikosov, "Electron scattering on magnetic impurities in metals and anomalous resistivity effects," *Physics Physique Fizika*, vol. 2, pp. 5–20, Sep 1965.

[61] K. G. Wilson, "The renormalization group: Critical phenomena and the kondo problem," *Rev. Mod. Phys.*, vol. 47, pp. 773–840, Oct 1975.

[62] K. Kadowaki and S. B. Woods, "Universal relationship of the resistivity and specific heat in heavy-Fermion compounds," *Solid State Communications*, vol. 58, pp. 507–509, 1986.

[63] A. Schröder, G. Aeppli, R. Coldea, M. Adams, O. Stockert, H. V. Löhneysen, E. Bucher, R. Ramazashvili, and P. Coleman, "Onset of antiferromagnetism in heavy-fermion metals," *Nature*, vol. 407, p. 351–355, 2000.

[64] S. Friedemann, N. Oeschler, S. Wirth, C. Krellner, C. Geibel, F. Steglich, S. Paschen, S. Kirchner, and Q. Si, "Fermi-surface collapse and dynamical scaling near a quantum-critical point," *Proceedings of the National Academy of Sciences*, vol. 107, no. 33, pp. 14547–14551, 2010.

[65] Q. Si, S. Rabello, K. Ingersent, and J. L. Smith, "Locally critical quantum phase transitions in strongly correlated metals," *Nature*, vol. 413, p. 804–808, 2001.

[66] P. Coleman, C. Pépin, Q. Si, and R. Ramazashvili, "How do fermi liquids get heavy and die?," *Journal of Physics: Condensed Matter*, vol. 13, pp. R723–R738, aug 2001.

[67] L. Zhu, S. Kirchner, Q. Si, and A. Georges, "Quantum critical properties of the bose-fermi kondo model in a large-n limit," *Phys. Rev. Lett.*, vol. 93, p. 267201, Dec 2004.

[68] J. H. Pixley, S. Kirchner, K. Ingersent, and Q. Si, "Kondo destruction and valence fluctuations in an anderson model," *Phys. Rev. Lett.*, vol. 109, p. 086403, Aug 2012.

[69] Y. Komijani and P. Coleman, "Emergent critical charge fluctuations at the kondo breakdown of heavy fermions," *Phys. Rev. Lett.*, vol. 122, p. 217001, May 2019.

[70] A. Cai, Z. Yu, H. Hu, S. Kirchner, and Q. Si, "Dynamical scaling of charge and spin responses at a kondo destruction quantum critical point," *Phys. Rev. Lett.*, vol. 124, p. 027205, Jan 2020.

[71] L. Prochaska, X. Li, D. C. MacFarland, A. M. Andrews, M. Bonta, E. F. Bianco, S. Yazdi, W. Schrenk, H. Detz, A. Limbeck, Q. Si, E. Ringe, G. Strasser, J. Kono, and S. Paschen, "Singular charge fluctuations at a magnetic quantum critical point," *Science*, vol. 367, no. 6475, pp. 285–288, 2020.

[72] J.-X. Zhu, D. R. Grempel, and Q. Si, "Continuous quantum phase transition in a kondo lattice model," *Phys. Rev. Lett.*, vol. 91, p. 156404, Oct 2003.

[73] M. T. Glossop and K. Ingersent, "Numerical renormalization-group study of the bose-fermi kondo model," *Phys. Rev. Lett.*, vol. 95, p. 067202, Aug 2005.

[74] J. H. Pixley, S. Kirchner, K. Ingersent, and Q. Si, "Quantum criticality in the pseudogap bose-fermi anderson and kondo models: Interplay between fermion- and boson-induced kondo destruction," *Phys. Rev. B*, vol. 88, p. 245111, Dec 2013.

[75] L. Zhu and Q. Si, "Critical local-moment fluctuations in the bose-fermi kondo model," *Phys. Rev. B*, vol. 66, p. 024426, Jul 2002.

[76] G. Zaránd and E. Demler, "Quantum phase transitions in the bose-fermi kondo model," *Phys. Rev. B*, vol. 66, p. 024427, Jul 2002.

[77] Q. Si, S. Rabello, K. Ingersent, and J. L. Smith, "Local fluctuations in quantum critical metals," *Phys. Rev. B*, vol. 68, p. 115103, Sep 2003.

[78] Y. Kamihara, T. Watanabe, M. Hirano, and H. Hosono, "Iron-based layered superconductor La[$O_{1-x}F_x$]FeAs (x= 0.05-0.12) with T_c = 26 K," *Journal of the American Chemical Society*, vol. 130, pp. 3296–3297, 2008.

[79] D. C. Johnston, "The puzzle of high temperature superconductivity in layered iron pnictides and chalcogenides," *Advances in Physics*, vol. 59, no. 6, pp. 803–1061, 2010.

[80] J. Dai, Q. Si, J.-X. Zhu, and E. Abrahams, "Iron pnictides as a new setting for quantum criticality," *Proceedings of the National Academy of Sciences*, vol. 106, no. 11, pp. 4118–4121, 2009.

[81] Q. Si and E. Abrahams, "Strong correlations and magnetic frustration in the high T_c iron pnictides," *Phys. Rev. Lett.*, vol. 101, p. 076401, Aug 2008.

[82] F. Ma, Z.-Y. Lu, and T. Xiang, "Arsenic-bridged antiferromagnetic superexchange interactions in lafeaso," *Phys. Rev. B*, vol. 78, p. 224517, Dec 2008.

[83] T. Yildirim, "Origin of the 150-k anomaly in lafeaso: Competing antiferromagnetic interactions, frustration, and a structural phase transition," *Phys. Rev. Lett.*, vol. 101, p. 057010, Aug 2008.

[84] P. Chandra, P. Coleman, and A. I. Larkin, "Ising transition in frustrated heisenberg models," *Phys. Rev. Lett.*, vol. 64, pp. 88–91, Jan 1990.

[85] C. Fang, H. Yao, W.-F. Tsai, J. Hu, and S. A. Kivelson, "Theory of electron nematic order in lafeaso," *Phys. Rev. B*, vol. 77, p. 224509, Jun 2008.

[86] C. Xu, M. Müller, and S. Sachdev, "Ising and spin orders in the iron-based superconductors," *Phys. Rev. B*, vol. 78, p. 020501, Jul 2008.

[87] C. De La Cruz, Q. Huang, J. W. Lynn, J. Li, W. Ratcliff, J. L. Zarestky, H. A. Mook, G. F. Chen, J. L. Luo, N. L. Wang, and P. Dai, "Magnetic order close to superconductivity in the iron-based layered $\mathrm{lao}_{1-x}\mathrm{f}_x\mathrm{feas}$ systems," *Nature*, vol. 453, p. 899–902, 2008.

[88] J. Zhao, Q. Huang, C. De La Cruz, S. Li, J. W. Lynn, Y. Chen, M. A. Green, G. F. Chen, G. Li, Z. Li, J. L. Luo, N. L. Wang, and P. Dai, "Structural and magnetic phase diagram of CeFeAsO(1 x)F(x) and its relation to high-temperature superconductivity," *Nature Materials*, vol. 7, p. 953–959, 2008.

[89] S. Jiang, H. Xing, G. Xuan, C. Wang, Z. Ren, C. Feng, J. Dai, Z. Xu, and G. Cao, "Superconductivity up to 30 k in the vicinity of the quantum critical point in $\mathrm{bafe}_2(\mathrm{as}_{1-x}\mathrm{p}_x)_2$," *Journal of Physics Condensed Matter*, vol. 21, p. 38, 2009.

[90] J. G. Analytis, H. H. Kuo, R. D. Mcdonald, M. Wartenbe, P. M. Rourke, N. E. Hussey, and I. R. Fisher, "Transport near a quantum critical point in $BaFe_2$ ($As_{1-x}P_x$)$_2$," *Nature Physics*, vol. 10, p. 194–197, 2014.

[91] H.-H. Kuo, J.-H. Chu, J. C. Palmstrom, S. A. Kivelson, and I. R. Fisher, "Ubiquitous signatures of nematic quantum criticality in optimally doped fe-based superconductors," *Science*, vol. 352, no. 6288, pp. 958–962, 2016.

[92] Y. Nakai, T. Iye, S. Kitagawa, K. Ishida, H. Ikeda, S. Kasahara, H. Shishido, T. Shibauchi, Y. Matsuda, and T. Terashima, "Unconventional superconductivity and antiferromagnetic quantum critical behavior in the isovalent-doped $bafe_2(as_{1-x}\mathbf{p}_x)_2$," *Phys. Rev. Lett.*, vol. 105, p. 107003, Sep 2010.

[93] T. Senthil, M. Vojta, and S. Sachdev, "Weak magnetism and non-fermi liquids near heavy-fermion critical points," *Phys. Rev. B*, vol. 69, p. 035111, Jan 2004.

[94] M. Levin and T. Senthil, "Deconfined quantum criticality and néel order via dimer disorder," *Phys. Rev. B*, vol. 70, p. 220403, Dec 2004.

[95] A. Tanaka and X. Hu, "Many-body spin berry phases emerging from the π-flux state: Competition between antiferromagnetism and the valence-bond-solid state," *Phys. Rev. Lett.*, vol. 95, p. 036402, Jul 2005.

[96] T. Senthil and M. P. A. Fisher, "Competing orders, nonlinear sigma models, and topological terms in quantum magnets," *Phys. Rev. B*, vol. 74, p. 064405, Aug 2006.

[97] S. Saremi, P. A. Lee, and T. Senthil, "Unifying kondo coherence and antiferromagnetic ordering in the honeycomb lattice," *Phys. Rev. B*, vol. 83, p. 125120, Mar 2011.

[98] C.-K. Lu and I. F. Herbut, "Zero modes and charged skyrmions in graphene bilayer," *Phys. Rev. Lett.*, vol. 108, p. 266402, Jun 2012.

[99] P. Goswami and Q. Si, "Dynamic zero modes of dirac fermions and competing singlet phases of antiferromagnetic order," *Phys. Rev. B*, vol. 95, p. 224438, Jun 2017.

[100] J. H. Pixley, R. Yu, and Q. Si, "Quantum phases of the shastry-sutherland kondo lattice: Implications for the global phase diagram of heavy-fermion metals," *Phys. Rev. Lett.*, vol. 113, p. 176402, Oct 2014.

[101] M. S. Kim and M. C. Aronson, "Spin liquids and antiferromagnetic order in the shastry-sutherland-lattice compound yb_2pt_2Pb," *Phys. Rev. Lett.*, vol. 110, p. 017201, Jan 2013.

[102] V. Fritsch, N. Bagrets, G. Goll, W. Kittler, M. J. Wolf, K. Grube, C.-L. Huang, and H. v. Löhneysen, "Approaching quantum criticality in a partially geometrically frustrated heavy-fermion metal," *Phys. Rev. B*, vol. 89, p. 054416, Feb 2014.

[103] L. Jiao, Y. Chen, Y. Kohama, D. Graf, E. D. Bauer, J. Singleton, J.-X. Zhu, Z. Weng, G. Pang, T. Shang, J. Zhang, H.-O. Lee, T. Park, M. Jaime, J. D. Thompson, F. Steglich, Q. Si, and H. Q. Yuan, "Fermi surface reconstruction and multiple quantum phase transitions in the antiferromagnet cerhin5," *Proceedings of the National Academy of Sciences*, vol. 112, no. 3, pp. 673–678, 2015.

[104] Y. Tokiwa, C. Stingl, M.-S. Kim, T. Takabatake, and P. Gegenwart, "Characteristic signatures of quantum criticality driven by geometrical frustration,"

Science Advances, vol. 1, no. 3, 2015.

[105] J. Goldstone and F. Wilczek, "Fractional quantum numbers on solitons," *Phys. Rev. Lett.*, vol. 47, pp. 986–989, Oct 1981.

[106] A. G. Abanov and P. B. Wiegmann, "Theta-terms in nonlinear sigma-models," *Nuclear Physics B*, vol. 570, pp. 685–698, March 2000.

[107] G. V. Dunne and K. Rao, "Thermal fluctuations of induced fermion number," *Phys. Rev. D*, vol. 64, p. 025003, Jun 2001.

[108] S. Kahana and G. Ripka, "Baryon density of quarks coupled to a chiral field," *Nuclear Physics B*, vol. 429, pp. 462–476, 1984.

[109] T. Jaroszewicz, "Induced fermion current in the σ model in $(2 + 1)$ dimensions," *Nuclear Physics B*, vol. 146, pp. 337–340, 1984.

[110] A. M. Tsvelik, "Semiclassical solution of one dimensional model of kondo insulator," *Phys. Rev. Lett.*, vol. 72, pp. 1048–1051, Feb 1994.

[111] P. Goswami and Q. Si, "Effects of the berry phase and instantons in one-dimensional kondo-heisenberg model," *Phys. Rev. Lett.*, vol. 107, p. 126404, Sep 2011.

[112] R. MacKenzie, F. Wilczek, and A. Zee, "Possible form of vacuum deformation by heavy particles," *Phys. Rev. Lett.*, vol. 53, pp. 2203–2206, Dec 1984.

[113] I. J. R. Aitchison and C. M. Fraser, "Derivative expansions of fermion determinants: Anomaly-induced vertices, goldstone-wilczek currents, and skyrme terms," *Phys. Rev. D*, vol. 31, pp. 2605–2615, May 1985.

[114] I. Affleck and F. D. M. Haldane, "Critical theory of quantum spin chains," *Phys. Rev. B*, vol. 36, pp. 5291–5300, Oct 1987.

[115] Y. H. Chen and F. Wilczek, "Induced quantum numbers in some 2+1 dimensional models," *Int. J. Mod. Phys. B*, vol. 3, p. 117, 1989.

[116] M. Carena, S. Chaudhuri, and C. E. M. Wagner, "Induced fermion number in the o(3) nonlinear σ model," *Phys. Rev. D*, vol. 42, pp. 2120–2126, Sep 1990.

[117] E. Witten, "An su(2) anomaly," *Physics Letters B*, vol. 117, pp. 324–328, 1982.

[118] M. Shifman, *Advanced Topics in Quantum Field Theory*. Cambridge University Presss, 2012.

[119] C.-Y. Hou, C. Chamon, and C. Mudry, "Electron fractionalization in two-dimensional graphenelike structures," *Phys. Rev. Lett.*, vol. 98, p. 186809, May 2007.

[120] R. Jackiw and C. Rebbi, "Solitons with fermion number ½," *Phys. Rev. D*, vol. 13, pp. 3398–3409, Jun 1976.

[121] G. 't Hooft, "Computation of the quantum effects due to a four-dimensional pseudoparticle," *Phys. Rev. D*, vol. 14, pp. 3432–3450, Dec 1976.

[122] C. J. Callias, "Spectra of fermions in monopole fields—exactly soluble models," *Phys. Rev. D*, vol. 16, pp. 3068–3077, Nov 1977.

[123] R. Jackiw and C. Rebbi, "Spinor analysis of yang-mills theory," *Phys. Rev. D*, vol. 16, pp. 1052–1060, Aug 1977.

[124] R. Blankenbecler and D. Boyanovsky, "Fractional charge and spectral asymmetry in one dimension: A closer look," *Phys. Rev. D*, vol. 31, pp. 2089–2099, Apr 1985.

[125] S.-S. Lee, "Low-energy effective theory of fermi surface coupled with u(1) gauge field in $2+1$ dimensions," *Phys. Rev. B*, vol. 80, p. 165102, Oct 2009.

[126] M. A. Metlitski and S. Sachdev, "Quantum phase transitions of metals in two spatial dimensions. i. ising-nematic order," *Phys. Rev. B*, vol. 82, p. 075127, Aug 2010.

[127] M. A. Metlitski and S. Sachdev, "Quantum phase transitions of metals in two spatial dimensions. ii. spin density wave order," *Phys. Rev. B*, vol. 82, p. 075128, Aug 2010.

[128] S.-S. Lee, "Recent developments in non-fermi liquid theory," *Annual Review of Condensed Matter Physics*, vol. 9, no. 1, pp. 227–244, 2018.

[129] S. J. Yamamoto and Q. Si, "Fermi surface and antiferromagnetism in the kondo lattice: An asymptotically exact solution in $d > 1$ dimensions," *Phys. Rev. Lett.*, vol. 99, p. 016401, Jul 2007.

[130] T. T. Ong and B. A. Jones, "Analysis of the antiferromagnetic phase transitions of the 2d kondo lattice," *Phys. Rev. Lett.*, vol. 103, p. 066405, Aug 2009.

[131] A. Auerbach, *Interacting Electrons and Quantum Magnetism*. Springer, 1998.

[132] E. Manousakis and R. Salvador, "Two-dimensional spin-1/2 antiferromagnetic heisenberg model versus nonlinear σ model," *Phys. Rev. Lett.*, vol. 62, pp. 1310–1313, Mar 1989.

[133] E. Manousakis and R. Salvador, "Equivalence between the nonlinear σ model and the spin-(1/2 antiferromagnetic heisenberg model: Spin correlations in la_2cuo_4," *Phys. Rev. B*, vol. 40, pp. 2205–2216, Aug 1989.

[134] R. Shankar, "Renormalization-group approach to interacting fermions," *Rev. Mod. Phys.*, vol. 66, pp. 129–192, Jan 1994.

[135] P. M. Chaikin and T. C. Lubensky, *Principles of Condensed Matter Physics*. Cambridge University Press, 2012.

[136] T. Grover and T. Senthil, "Quantum phase transition from an antiferromagnet to a spin liquid in a metal," *Phys. Rev. B*, vol. 81, p. 205102, May 2010.

[137] R. Shiina, H. Shiba, and P. Thalmeier, "Magnetic-field effects on quadrupolar ordering in a γ_8-quartet system ceb_6," *J. Phys. Soc. Jpn.*, vol. 66, no. 6, p. 1741, 1997.

[138] K.-A. Lorenzer, *Quantum critical behaviour in cubic heavy-fermion compounds*. PhD thesis, Vienna University of Technology, 2012.

[139] P. Y. Portnichenko, S. Paschen, A. Prokofiev, M. Vojta, A. S. Cameron, J.-M. Mignot, A. Ivanov, and D. S. Inosov, "Incommensurate short-range multipolar order parameter of phase II in $Ce_3Pd_{20}Si_6$," *Phys. Rev. B*, vol. 94, p. 245132, Dec 2016.

[140] J. Custers, K. Lorenzer, M. Müller, A. Prokofiev, A. Sidorenko, H. Winkler, A. M. Strydom, Y. Shimura, T. Sakakibara, R. Yu, Q. Si, and S. Paschen, "Destruction of the Kondo effect in the cubic heavy-fermion compound $Ce_3Pd_{20}Si_6$," *Nature Mater.*, vol. 11, p. 189, 2012.

[141] Y. Kuramoto, "Perturbative renormalization of multi-channel Kondo-type models," *The European Physical Journal B - Condensed Matter and Complex Systems*, vol. 5, no. 3, pp. 457–464, 1998.

[142] C. Aron and G. Kotliar, "Analytic theory of hund's metals: A renormalization group perspective," *Phys. Rev. B*, vol. 91, p. 041110, Jan 2015.

[143] J. L. Smith and Q. Si, "Spatial correlations in dynamical mean-field theory," *Phys. Rev. B*, vol. 61, no. 8, p. 5184, 2000.

[144] R. Chitra and G. Kotliar, "Effective-action approach to strongly correlated fermion systems," *Phys. Rev. B*, vol. 63, no. 11, p. 115110, 2001.

[145] Q. Si and J. L. Smith, "Kosterlitz-thouless transition and short range spatial correlations in an extended hubbard model," *Phys. Rev. Lett.*, vol. 77, pp. 3391–3394, Oct 1996.

[146] F. Wang and D.-H. Lee, "The electron-pairing mechanism of iron-based superconductors," *Science*, vol. 332, no. 6026, pp. 200–204, 2011.

[147] P. Dai, "Antiferromagnetic order and spin dynamics in iron-based superconductors," *Rev. Mod. Phys.*, vol. 87, pp. 855–896, Aug 2015.

[148] P. J. Hirschfeld, "Using gap symmetry and structure to reveal the pairing mechanism in fe-based superconductors," *Comptes Rendus Physique*, vol. 17, p. 197, 2016.

[149] J.-H. Chu, J. G. Analytis, K. De Greve, P. L. McMahon, Z. Islam, Y. Yamamoto, and I. R. Fisher, "In-plane resistivity anisotropy in an underdoped iron arsenide superconductor," *Science*, vol. 329, no. 5993, pp. 824–826, 2010.

[150] M. Yi, D. Lu, J.-H. Chu, J. G. Analytis, A. P. Sorini, A. F. Kemper, B. Moritz, S.-K. Mo, R. G. Moore, M. Hashimoto, W.-S. Lee, Z. Hussain, T. P. Devereaux, I. R. Fisher, and Z.-X. Shen, "Symmetry-breaking orbital anisotropy observed for detwinned ba(fe1-xcox)2as2 above the spin density wave transition," *Proceedings of the National Academy of Sciences*, vol. 108, no. 17, pp. 6878–6883, 2011.

[151] X. Lu, J. T. Park, R. Zhang, H. Luo, A. H. Nevidomskyy, Q. Si, and P. Dai, "Nematic spin correlations in the tetragonal state of uniaxial-strained bafe2-xnixas2," *Science*, vol. 345, no. 6197, pp. 657–660, 2014.

[152] R. Willa, M. Fritz, and J. Schmalian, "Strain tuning and anisotropic spin correlations in iron-based systems," *Phys. Rev. B*, vol. 100, p. 085106, Aug 2019.

[153] V. Stanev and P. B. Littlewood, "Nematicity driven by hybridization in iron-based superconductors," *Phys. Rev. B*, vol. 87, p. 161122, Apr 2013.

[154] S.-P. Kou, T. Li, and Z.-Y. Weng, "Coexistence of itinerant electrons and local moments in iron-based superconductors," *EPL (Europhysics Letters)*, vol. 88, p. 17010, oct 2009.

[155] F. Krüger, S. Kumar, J. Zaanen, and J. van den Brink, "Spin-orbital frustrations and anomalous metallic state in iron-pnictide superconductors," *Phys. Rev. B*, vol. 79, p. 054504, Feb 2009.

[156] W. Lv, J. Wu, and P. Phillips, "Orbital ordering induces structural phase transition and the resistivity anomaly in iron pnictides," *Phys. Rev. B*, vol. 80, p. 224506, Dec 2009.

[157] D. Hu, X. Lu, W. Zhang, H. Luo, S. Li, P. Wang, G. Chen, F. Han, S. R. Banjara, A. Sapkota, A. Kreyssig, A. I. Goldman, Z. Yamani, C. Niedermayer, M. Skoulatos, R. Georgii, T. Keller, P. Wang, W. Yu, and P. Dai, "Structural and magnetic phase transitions near optimal superconductivity in $BaFe_2(As_{1-x}P_x)_2$," *Phys. Rev. Lett.*, vol. 114, p. 157002, Apr 2015.

[158] K. Binder, "Theory of first-order phase transitions," *Reports on Progress in Physics*, vol. 50, pp. 783–859, jul 1987.

[159] S. Kasahara, T. Shibauchi, K. Hashimoto, K. Ikada, S. Tonegawa, R. Okazaki, H. Shishido, H. Ikeda, H. Takeya, K. Hirata, T. Terashima, and Y. Matsuda, "Evolution from non-fermi- to fermi-liquid transport via isovalent doping in $bafe_2(As_{1-x}P_x)_2$ superconductors," *Phys. Rev. B*, vol. 81, p. 184519, May 2010.

[160] I. M. Hayes, R. D. McDonald, N. P. Breznay, T. Helm, P. J. W. Moll, M. Wartenbe, A. Shekhter, and J. G. Analytis, "Scaling between magnetic field and temperature in the high-temperature superconductor BaFe2(As1−xPx)2," *Nature Physics*, vol. 12, no. 10, pp. 916–919, 2016.

[161] D. Hu, H. Hu, W. Zhang, Y. Wei, S. Li, Y. Gu, X. Ma, D. L. Abernathy, S. Chi, W. J. Travis, Y. Li, Q. Si, and P. C. Dai, "ω/t scaling and magnetic quantum criticality in $bafe_2(as_{0.7}p_{0.3})_2$," *arXiv:1812.11902*.

[162] R. Zhou, Z. Li, J. Yang, D. L. Sun, C. T. Lin, and G.-q. Zheng, "Quantum criticality in electron-doped BaFe2−xNixAs2," *Nature Communications*, vol. 4, no. 1, p. 2265, 2013.

[163] H. Luo, M. Wang, C. Zhang, X. Lu, L.-P. Regnault, R. Zhang, S. Li, J. Hu, and P. Dai, "Spin excitation anisotropy as a probe of orbital ordering in the para-

magnetic tetragonal phase of superconducting $\mathrm{bafe}_{1.904}\mathrm{ni}_{0.096}\mathrm{as}_2$," *Phys. Rev. Lett.*, vol. 111, p. 107006, Sep 2013.

[164] M. Peskin and D. Schroeder, *An Introduction To Quantum Field Theory*. Perseus Books, 1995.

[165] J. Zinn-Justin, *Phase Transitions and Renormalization Group*. Oxford University Press, 2007.

[166] J. Zinn-Justin, *Critical Properties of ϕ^4-Theories*. World Scientific, Singapore, 2001.

[167] S. Chakravarty and J. E. Hirsch, "Approximate mapping of the two-impurity symmetric anderson model in the local-moment regime to a classical problem," *Phys. Rev. B*, vol. 25, pp. 3273–3282, Mar 1982.

[168] J. L. Cardy, "One-dimensional models with 1/r2interactions," *Journal of Physics A: Mathematical and General*, vol. 14, pp. 1407–1415, jun 1981.

[169] Q. Si and G. Kotliar, "Metallic non-fermi-liquid phases of an extended hubbard model in infinite dimensions," *Phys. Rev. B*, vol. 48, pp. 13881–13903, Nov 1993.